POLITECNICO DI TORINO

DEPARTMENT OF SPACE ENGINEERING
Master Degree in Aerospace Engineering

Exchange University: **TECHNISCHE UNIVERSITEIT DELFT**

Preliminary Mission Analysis and Sub-System Design for the 16U4SBSP CubeSat Mission

Supervisors
Prof. Angelo Cervone
Prof. Manuela Battipede

Candidate
Caterina Busso

Academic Year 2023 - 2024

A Mamma, Papà,
Diletta e Beatrice.

Abstract

The mission concept "16U4SBSP", funded by the European Space Agency through the Sysnova campaign "Innovative Missions Concepts enabled by Swarms of CubeSats", aims to demonstrate the feasibility of a swarm of 16U CubeSats for a scaled demonstration of Space-Based Solar Power (SBSP). This demonstration mission can provide wireless electric energy in kW-scale to space-to-ground or space-to-space applications. The main objective of the mission is to validate the SBSP concept and some of the involved technologies, in view of full-scale missions which could serve users in remote areas with low power requirements (<MW) or/and emergency operations in the blackout zones affected by natural or manmade hazards.

The focus of this master thesis is the study of the mission's formation flying orbital dynamics for the case of Heliotropic orbits and the study of the thermal analysis and thermal design of the CubeSats. The dynamical model used accounts for perturbations from Earth's gravitational field up to the fourth degree, solar radiation pressure, and atmospheric drag. The configuration of the swarm includes seven CubeSats in a circular formation, with one CubeSat positioned at the center and six CubeSats distributed in a hexagonal shape around it. Heliotropic orbits are defined as sun-frozen orbits that enable extended periods of energy beaming during nighttime. Initially, the long-term evolution of the orbit is characterized. The analysis then focuses on the evolution of the relative distance variation of each CubeSat with respect to the central one within the heliotropic formation. This determines the frequency of formation control required to maintain the relative positions of each CubeSat. The findings suggest that employing a formation in a Heliotropic orbit is a suitable option for the mission, but not as cost-effective as a Sun-Synchronous orbit. For the thermal analysis, it has been used a simplified single-node steady-state lumped mass thermal analysis in order to define a baseline understanding of the thermal loads and expected temperatures of the spacecraft. A trade-off is conducted about the choice of materials to be used as passive coatings. Additionally, crucial aspects of the CubeSat design have been studied, including an illumination study for optimal star tracker placement.

The work presented in the thesis contributed to prove the feasibility of the 16U4SBSP mission's objectives representing the first step towards GW-scale SBSP, that would supply clean energy from space through wireless power transmission.

Contents

Chapter 1

Introduction

The “16U4SBSP” mission concept is a fundamental technology demonstration step for the realization of kW-/MW-/GW-scale Space-Based Solar Power (SBSP) based on flight formation, a distrusted swarm of small satellites contrary to conventional concepts of monolithic giant SBSP satellites. In this mission, a swarm of 16U CubeSats collaboratively supply wireless power via Radio-Frequency waves to end-users in different locations on the ground, for instance to provide backup power for emergency situations, and also for space-to-space commercial use-cases.

The 16U4SBSP project, currently in phases 0 and A, is the outcome of a collaborative effort between Delft University of Technology, the University of Strathclyde, and Sirin Orbital Systems AG. This innovative project was presented at ESA ESTEC as part of the Open Space Innovation Platform (OSIP) campaign, under the theme "Innovative Mission Concepts Enabled by Swarms of CubeSats."

The scope of this thesis is to conduct a preliminary mission analysis study on the stability of formation flying in the Heliotropic Orbit. Beginning with the dynamical model of the orbit, the thesis explores the definition and characteristics of the heliotropic orbit and examines the formation flying aspect in detail. Furthermore, some aspects of the sub-system design are analyzed, including thermal analysis. This analysis is conducted in a preliminary phase, considering a single-node steady-state situation.

This chapter provides a comprehensive summary of the mission 16U4SBSP, detailing the key elements of the final mission analysis and the various sub-system design choices. It offers an overview of the critical aspects that were considered during the mission planning and highlights the rationale behind the design decisions made for each sub-system. At the end of this introduction, the final spacecraft configuration is presented.

1.1 Mission Analysis

The 16U4SBSP mission aims to demonstrate Space-Based Solar Power (SBSP) using a CubeSat (CS) swarm from Earth orbit. This demonstration employs seven 16U CSs to deliver 1 kW-scale wireless energy via Radio-Frequency (RF) beaming, adaptable for both space-to-ground and space-to-space applications. The primary goal is to validate SBSP provision using a satellite swarm and explore miniaturized technologies for future large-scale missions that could benefit remote or emergency areas. [24]

Firstly, the mission orbit is identified. A trade off is conducted between the Sun-synchronous orbits and the Heliotropic orbits, which is presented in chapter 3. The case of Sun-synchronous orbits (SSO) is selected. SSOs are a type of near-polar orbit that enables a satellite to pass over a given point on Earth's surface at the same local solar time. This characteristic is achieved through a precise inclination and altitude that causes the orbit's Right Ascension of the Ascending Node Ω to precess at the same rate Earth orbits around the Sun, effectively synchronizing with the solar cycle. [12]

For missions where power is primarily needed at night to complement ground-based solar arrays, a sun-synchronous orbit offers significant advantages. It maximizes illumination during operational periods and minimizes the energy storage requirements, as the satellites are strategically positioned to efficiently leverage sunlight.

The configuration of the swarm consists of seven CubeSats arranged in a circular formation, with one central chief CubeSat and six deputy CubeSats arranged hexagonally around it as detailed explained in chapter 3.2.

The mission Concept of Operations includes: formation deployment and acquisition phase, operative phase and end-of-life phase. The CubeSats are deployed into a sun-synchronous orbit with a release cadence from the dispenser. The launch and early orbit phase (LEOP) have a duration of one day for attitude acquisition, solar array deployment, and subsystems check. Then, maneuvers for orbit circularization and phase correction of each CubeSat are executed to ensure that the CubeSats are correctly distributed in the along-track direction. An observation campaign is conducted before the acquisition phase, which consists of the establishing of the formation with 1000 m radius. Two following two days are reserved for verifying formation control, assessing orbit/attitude perturbations, antenna pointing, and time synchronization. [24]

After the first phase, the operative phase starts. The formation is adjusted to decrease the radius to 100 m and is maintained for the first half of the mission's duration (3 months). For the second half (3 months), the radius is further reduced to 10 meters. Finally, the end-of-life phase occurs. For an initial altitude of 500 km, the mission is projected to re-enter the Earth's atmosphere within 1,5 years naturally. Therefore, no maneuver is required. [24]

1.2 Payload

The main payload in 16U4SBSP is Wireless Power Transfer (WPT) module consisting of Tx antenna systems and circuit components (amplifier, convertor, etc.). In addition, a Rx rectenna system is needed. The radio frequency energy spans from a range of approximately 1–30 GHz and wavelengths from approximately 1 to 30 cm. [24]

For the design of the beamforming steering antenna, up to 4 calibration pilots are considered as 3 are required to remove the location and electrical uncertainties, while the fourth source is used to remove tapering uncertainty. On the ground segment, the use of the pilot calibration strategy introduces the requirement to have cooperative transmitters on the ground that would send pilot signals to calibrate the array.

The Tx antenna configuration is a deployable membrane antenna, shown in Fig. 1.1. It has 1440 antenna elements, 240 for each triangle (Fig.1.3), each one with a gain of 11 dBi, with each element separated half wavelength. The target total mass is 3.5kg and the target stored volume of the HRM mechanism is 150 mm x 150 mm x 100 mm. [24]

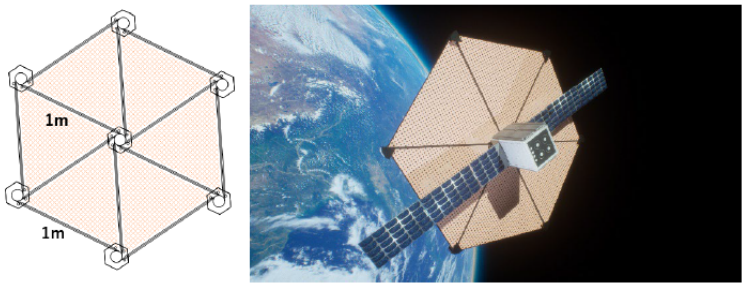

Figure 1.1: Deployable membrane hexagonal antenna (on the left), visualization of deployed membrane antenna (on the right). [24]

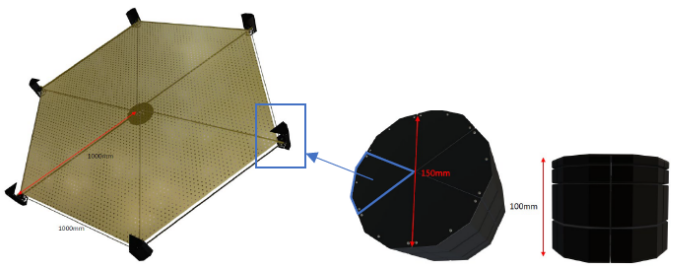

Figure 1.2: Fully deployed membrane hexagonal antenna 7N12B Model (on the left), Hold & Release Mechanism HRM (on the right). [24]

For feeding the RF into the antenna elements in the membrane, we are considering Microstrip lines. In summary, it is planned to feed the power by mounting an

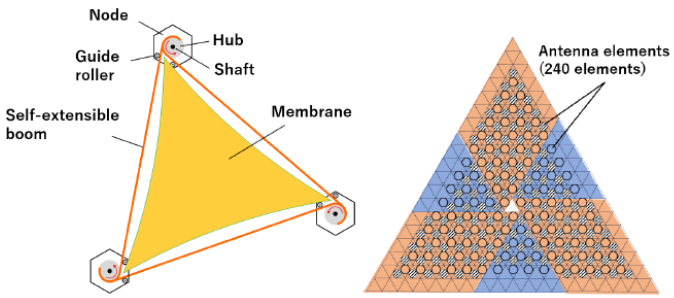

Figure 1.3: Mechanism for deployable structure. [24]

oscillator on the bus side, from which the power will be transmitted by microstrip lines to feed the antenna elements.

1.3 Propulsion

The presented propulsion sub-system refers to both the main propulsion system and the reaction control system. For both the main propulsion system and the reaction control system, some trade-offs are conducted. In particular one for the choice of the type of propulsion, and one for the type of propulsor to be used.

Regarding the reaction control system, it is not strictly necessary, since the attitude control can fully be accomplished by the reaction wheels, and wheels desaturation is performed by the magnetic torquers. However, a reaction control system has been included in the spacecraft for additional 6DOF control authority (for example, to support detumbling and reaction wheel desaturation if needed), and as a higher-thrust system for emergency collision avoidance maneuvers. The total impulse required for the RCS sub-system, as per requirement, is calculated assuming a total of 8 emergency collision avoidance maneuvers per spacecraft during the whole mission lifetime, this translates into a Delta-V per maneuver equal to approximately 0.27 m/s which, combined with an assumed spacecraft mass of 32 kg, translates into a total impulse for all 8 maneuvers of approximately 70 Ns. [24]

The selected main propulsion system is the Micro R^3 from Enpulsion, shown on the left in Fig. 1.4. It is a set of four electrospray thruster emitters using Indium as propellant. The full emitter box volume is 140x120x98.6 mm, while the PPU box volume is 140x120x34 mm. The nominal thrust is 1 mN at a nominal power level of 105 W, but a wide range of thrust, specific impulse and input power combinations are possible. The dry and wet mass are 2.6 kg and 3.9 kg respectively, for an available total impulse of no less than 30 kNs. The required heat-up power is between 20 and 40 W, and the standby power is between 10 and 15 W. The supply voltage is 28 $\pm$2 V.[24]

The selected component of the reaction control system is the IANUS system

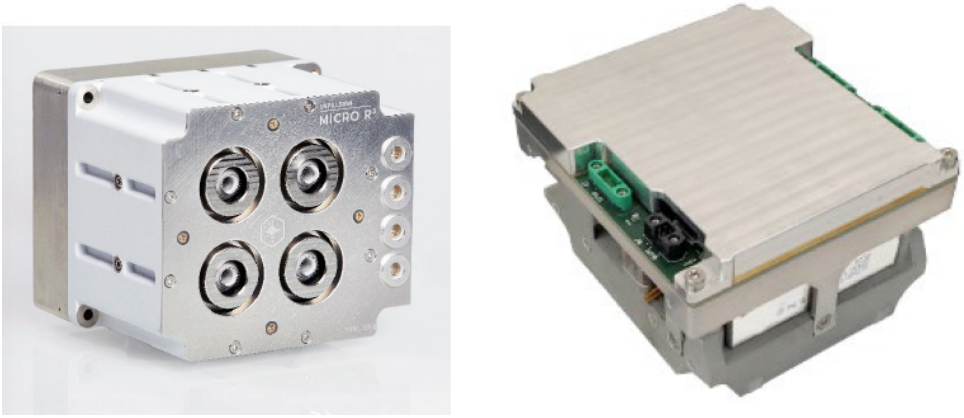

Figure 1.4: the Micro R^3 system from Enpulsion (on the left), and the IANUS system from t4i single module (on the right).[24]

developed by t4i (Italy). It is based on cold gas thrusters using R134a refrigerant as propellant. One single module, as shown on the right in Fig. 1.4, has 0.5U volume and a dry and wet mass of respectively 0.5 kg and 0.6 kg; however, in order to achieve full 6DOF control authority, two of these modules are required, which will also be the configuration employed by 16U4SBSP. The total impulse is 38 Ns per module (thus, 76 Ns in total for the two modules) and three possible thrust levels can be selected: 6.8, 10.6 or 26.2 mN, with the latter two options compatible with the requirements set for 16U4SBSP. The required power is 40 W while firing; no specific power levels are declared by the company for standby and heat-up, but these are expected to not exceed the values currently set by requirements. The supply voltage is 12 V unregulated, which is currently not compatible with requirement and will be left for further discussion in the next project phases to check if this requirement and/or the supply voltage characteristics of the system can be modified. [24]

1.4 Attitude Determination and Control and Navigation

This part presents the design of two of the most crucial sub-systems of the 16U4SBSP spacecraft: the Attitude Control and Determination System (ADCS) and the Navigation sub-system.

Some trade-offs are conducted to select the best component of this sub-systems. To simplify the integration process and allow for a more reliable design, the selection was limited to fully self-standing ADCS assemblies, not requiring additional component in order to perform all required functions. The critical requirements for the selection came from the capability of the system to cope with a 16U satellite

bus with external appendages (solar panels and deployable antenna) and the size to fit in the available volume onboard. [24]

The selected components are the EnduroSat 16U system including an attitude control computer and three CW5000 reaction wheels, and the FUGRO SpaceStar GNSS receiver (shown in Fig. 1.5). [24]

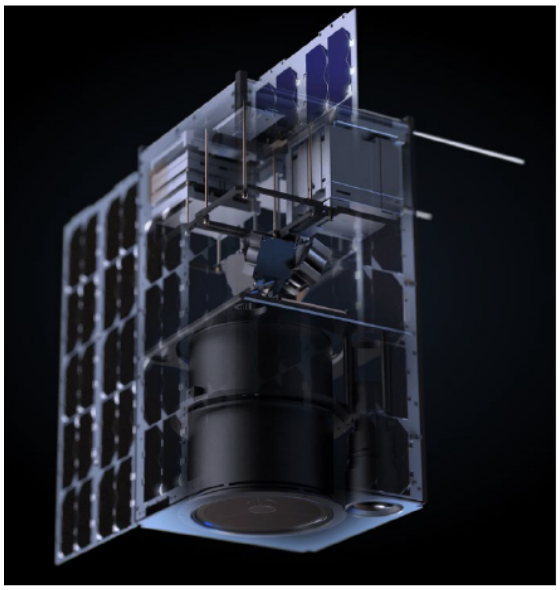

Figure 1.5: Skecht of the EnduroSat 16U platform, with ADCS components in the central part of the bus.[24]

The selected EnduroSat system is not a separate ADCS assembly, but it is designed as part of the full 16U platform available from the company. The system consists of a full set of components including in particular three reaction wheels, the ADCS control unit and two Star trackers. The total mass of the full set of ADCS components is 3.9 kg, for a total volume of 2U. The momentum storage capability of each wheel is 500 mNms, which allows to perform all de-tumbling and slew maneuvers only by means of the reaction wheels, as better explained in the following. The maximum wheel torque is 37 mNm, sufficient to meet with large margin all torque requirements for ground tracking and for counter-acting disturbance torques (the maximum expected disturbance torques are in the order of 1 mNm or less). [24]

The FUGRO SpaceStar GNSS receiver, selected after the trade-off on the available GNSS options, has a mass of 0.45 kg and a volume of 0.4U. It allows for an absolute positioning error of 10 cm RMS, which is already compatible with the mission requirements and can be further improved to approximately 5 cm by employing a “relative” link with differential GNSS using the data available from the inter-satellite link.[24]

1.5 Power System

This part presents the full range of hardware components selected for the Electrical Power System of the 16U4SBSP spacecraft, including the central Power Control Unit, the solar array assembly and the batteries for power storage, and the motivations and trade-offs that led to this final selection.

The batteries are considered the most critical EPS component in the 16U4SBSP spacecraft, due to their heavy requirements in terms of power storage and power peak/instantaneous power. Some trade-offs are conducted to select the best components for the Power System.

The battery selected is the Kongsberg/NanoAvionics 8S1P battery. In addition, for the EPS electronics (power conditioning and distribution unit) is selected the Kongsberg/NanoAvionics EPS electronics, shown in Fig. 1.6, to ensure maximum compatibility with the selected batteries. [24]

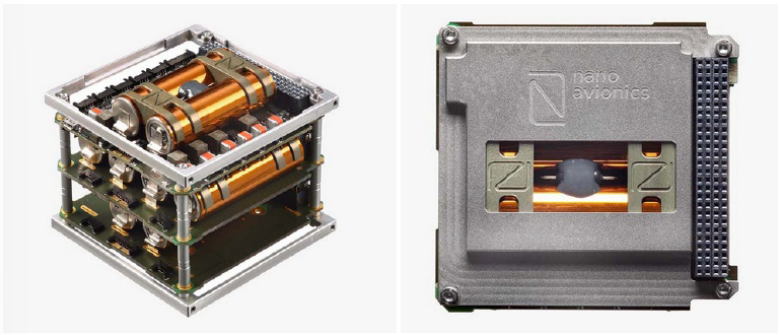

Figure 1.6: Pictures of the complete EPS box from Kongsberg/NanoAvionics. [24]

The selected components include a total of 4 stacked Li-ion battery units are used, which allows for a total battery capacity of 340.8 Wh BOL. Each of these four battery units has a volume of 0.4U. Each battery unit provides a peak power of 100 W, which allows to achieve a total of 400 W peak power with 4 units, thus meeting requirement. The power conditioning and distribution electronics is compatible to a wide range of solar panel input voltages (up to 42 V) and has a volume of 0.2U. [24]

To optimize the power generation capabilities of the spacecraft in function of the specific needs of the 16U4SBSP mission, the consortium has opted for a fully customized design of the solar array wings, built upon the 30% Triple Junction GaAs Solar Cell Assembly from AzurSpace, shown in Fig. 1.7. This solar cell assembly has 30.18 cm^2 area per cell, with a specific mass of 118 mg/cm^2. The maximum power point voltage is 2.409 V and the maximum power point current is 0.503 A, for a BOL efficiency higher than 29%. [24]

The final solar arrays configuration designed for the 16U4SBSP spacecraft consists of 2 separate wings, each with a total of 60 cells; additionally, in one of the two wings, 25 cells are present on the back side. With this configuration, a total power

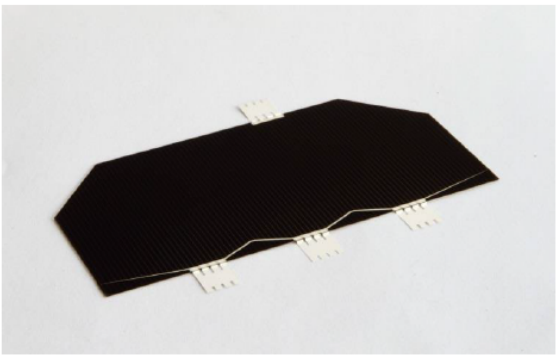

Figure 1.7: the Triple Junction GaAs Solar Cell Assembly from AzurSpace. [10]

generation capability of 144 W (72 W per wing) is available from the deployed wings, while 30 W are available in folded position before deployment.

1.6 Communication System

This part presents the trade-off results for the communications sub-system. Note that, given the specific characteristics of the 16U4SBSP and its Concept of Operations, two identical sets of radio and antenna need to be used by each spacecraft: one for the inter-satellite link and one for ground communication. The two communication systems are expected for simplicity to be identical. Since the requirement leaves the door open to two possible frequency bands (S band or X band), the main trade-off performed for the communications sub-system was to decide between these two frequency bands. It results that communicating in the S-band is a preferable option. [24]

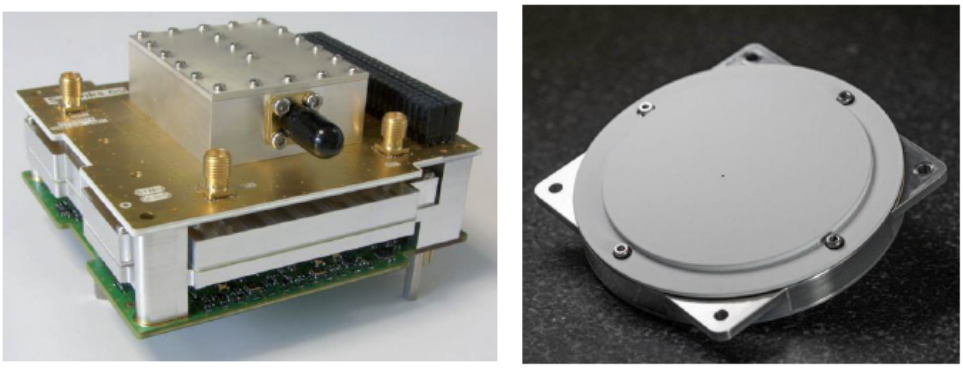

Figure 1.8: The Syrlinks EWC31 S-band radio (on the left) and the Anywaves S-band TT&C antenna (on the right). [24]

The selected S-band radio is the Syrlinks EWC31 model, shown on the left in Fig. 1.8. It is a flight-proven model, with integrated diplexer and capable of

operating in the 2200-2290 MHz frequency range (transmission) and the 2025-2110 MHz range (while receiving). The data rate can be in the range from 8 to 512 kbps, and the output power can be in the range from 27 to 36 dBm. The mass is 0.17 kg, the volume is 0.4U and the rated input power is 2 W. [24]

For what concerns the antenna, the Anywaves S-Band TT&C antenna has been currently selected. It is a patch antenna with strong flight heritage, with full duplex telemetry & telecommand capabilities. It can operate in a frequency range from 2025 to 2290 MHz, at a bandwidth higher than 265 MHz. It has a peak boresight gain of 6.5 dBi and a size of 84.3x84.3x12.1 mm. The mass is 0.139 kg and it can operate at temperatures between -120 and +120 ^{o}C. [24]

1.7 Structures and Mechanisms

This part shortly elaborates on the design choices made for the structural elements, the CubeSat deployer, and the spacecraft mechanisms.

For the 16U CubeSat structure, it is selected the fully qualified 16U structure provided by EnduroSat, previously shown in Fig. 1.5. This structure is fully built in Aluminium 6082 with hard-anodized surface and offers lightweight characteristics, with mass not higher than 3 kg. Some modifications to the available component structure will likely need to be made, especially to accommodate the main propulsion unit and the deployable antenna payload in the bottom 4U of the structure. [24]

The deployer selection will mainly depend on the finalized mass budget for the 16U4SBSP spacecraft, as obtained from the more detailed spacecraft design performed during Phases A and B. Two options are possible in this respect:

- final mass budget $<$ 32 kg: the 16U QuadPack dispenser from ISISpace, shown on the left in Fig. 1.9;
- final mass budget between 32 kg and 36 kg: EXOpod NOVA 16U S1 dispenser from ExoLaunch, shown on the right in Fig. 1.9.

For the solar panel tracking mechanism, three main mechanisms are included in the architecture.

- the solar arrays deployment mechanism
- the payload antenna deployment system
- the solar panel tracking mechanism (or SADA, Solar Array Drive Assembly).

Based on these requirements, the μSADA system produced by the company IMT has been selected for the 16U4SBSP spacecraft. The IMT µSADA system is

Figure 1.9: The ISISpace 16U QuadPack dispenser (on the left) and the EXOpod NOVA 16U S1 dispenser (on the right). [24]

based on a pointing mechanism with ± 0.3 deg pointing accuracy and full 180deg rotation capabilities of both wings in both directions, with power consumption of 0.5 W when pointing and 0.1 W in standby. It also offers a simultaneous deployment function for the two solar array wings, requiring a total power of 4.5 W during deployment, and can therefore also be used as solar arrays deployment mechanism. [24]

1.8 Thermal Control

A preliminary thermal analysis for the 16U4SBSP spacecraft is performed in chapter 5. The analysis is focused on a simplified single-node steady-state balance for the whole spacecraft, to predict the range of temperatures expected during operation and define a coating strategy on the external surface of the spacecraft for passive thermal control. In addition, it is conducted the definition of a strategy and subsystem design for dissipating the significant amount of heat produced by the payload during the power beaming phase.

In chapter 5, the passive coating thermal control selected is described. In addition to the passive coating, 5 active heaters are included in the spacecraft to be strategically placed to the most critical sub-systems and components for active thermal control in emergency or non-ideal conditions. [24]

Regarding the payload heat management, the maximum heat energy to be dissipated is equal to 22,06 Wh, and the total power of 132,4 W has to be dissipated. After careful consideration, the option of using radiators has been discarded. Dissipating such a large amount of power would require a deployable radiator, which poses significant reliability risks.

Therefore, the final selected solution is the phase-change material. This material stores the dissipated energy as latent heat, which is then gradually released during the eclipse phase of the orbit. This approach not only manages the energy dissipation effectively but also helps mitigate the cold conditions experienced during the eclipse. The material selected for a preliminary design is Tetracosane

($C_{24}H_{50}$), a paraffin characterized by a good compromise between melting temperature ($50.6°C$) and latent heat for melting (255 kJ/kg). The amount of Tetracosane required to dissipate the heat energy is 0,312 kg, which translate to a volume of the payload heat management box equal to 0,584 U. The external part of the box is assumed to be made of aluminium with 2 mm wall thickness; including also in this case a 50% margin to take into account any additional aluminium elements, including the internal fins/protrusions for better heat distribution, this leads to a mass of 0.490 kg for the aluminium elements in the box, and a total mass of 0.802 kg for the full payload heat management box. [24]

1.9 Command and Data Handling

The selected onboard computer shown in Fig. 1.10, the FERMI from Argotec, is originally designed for deep-space CubeSat missions, which allows for superior properties in terms of radiation hardening. The rated power consumption is slightly higher than 5 W, for a total mass of 534 g and 0.4U volume. The CPU features a dual-core processor with a wide range of available data interfaces and supply voltages. This onboard computer features a dedicated on-board software including, among other features, a built-in support for FDIR functions. A total of 16 GB are available as embedded mass memory. [24]

Figure 1.10: The Argotec FERMI onboard computer. [24]

1.10 Spacecraft Configuration

This part presents the final configuration of the 16U4SBSP spacecraft (as resulting from the design choices presented in the previous parts). Figures from 1.11 to 1.17 present in detail the spacecraft configuration. The main highlights of this configuration can be summarized as follows:

- One 4U side of the spacecraft (the side looking at nadir direction in power beaming mode) is fully used by the payload (deployable antenna + payload electronics at the center of the 4U unit), with the payload heat management box based on phase change material placed on top of the payload electronics.

- The opposite 4U side of the spacecraft (the side looking at zenith direction in power beaming mode) is fully used by the main propulsion system, centered with the nominal axis of the spacecraft, and the two RCS modules, on two opposite sides of the main propulsion unit.
- The two star trackers are on two opposite lateral sides of the spacecraft, placed in oblique direction with respect to the body-fixed reference frame to minimize straylight effects from the Sun.
- The first S-band antenna (for ground communication) is placed on the spacecraft side looking at nadir direction in power beaming mode, immediately underneath the payload electronics; the other S-band antenna (for inter-satellite communication) is placed on one of the side faces of the spacecraft.
- The GNSS antenna is placed in a corner of the spacecraft side looking at zenith direction.

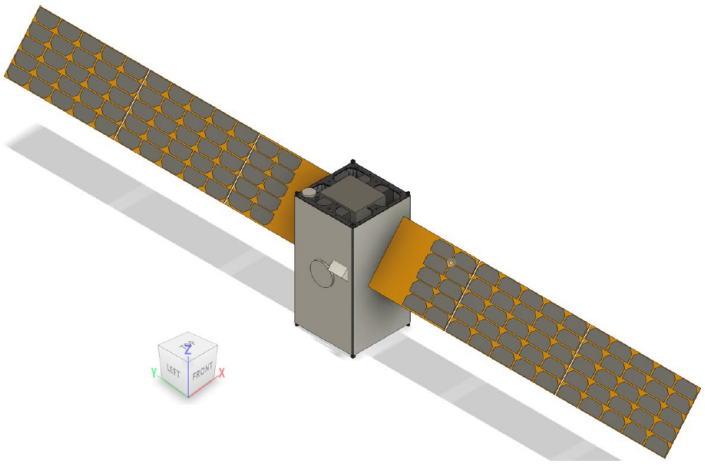

Figure 1.11: 16U4SBSP spacecraft with cover panels, solar array wings deployed.[24]

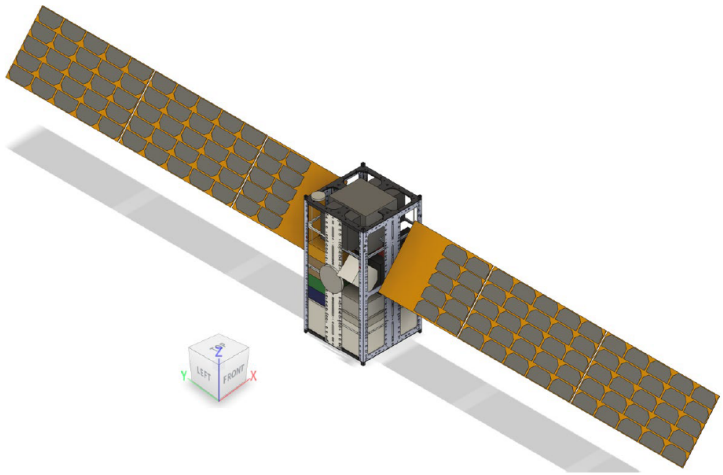

Figure 1.12: 16U4SBSP spacecraft without cover panels, solar array wings deployed.[24]

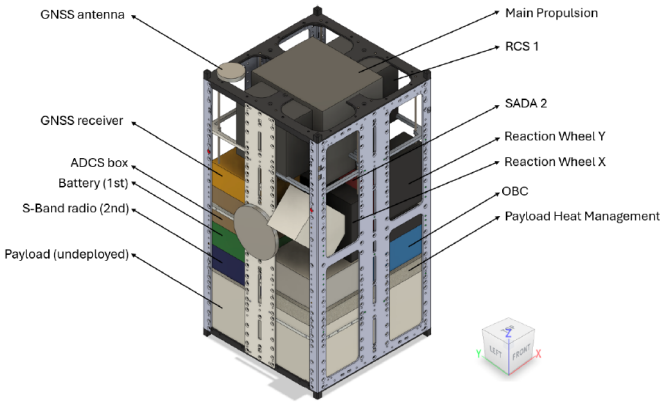

Figure 1.13: X-/Y- view of the 16U4SBSP spacecraft without cover panels and solar array wings.[24]

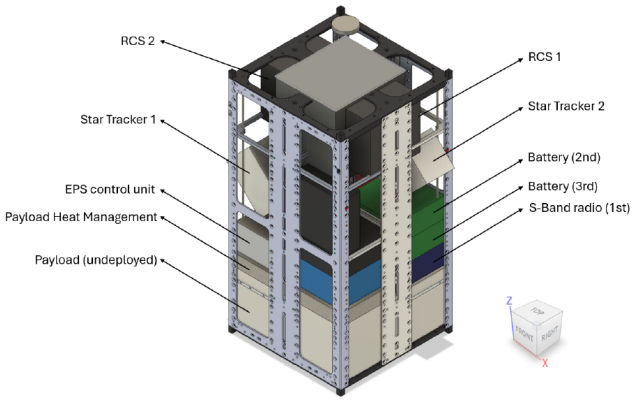

Figure 1.14: X+/Y- view of the 16U4SBSP spacecraft without cover panels and solar array wings.[24]

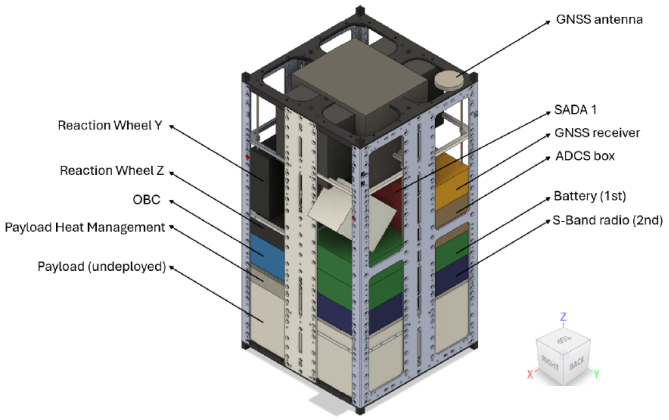

Figure 1.15: X+/Y+ view of the 16U4SBSP spacecraft without cover panels and solar array wings.[24]

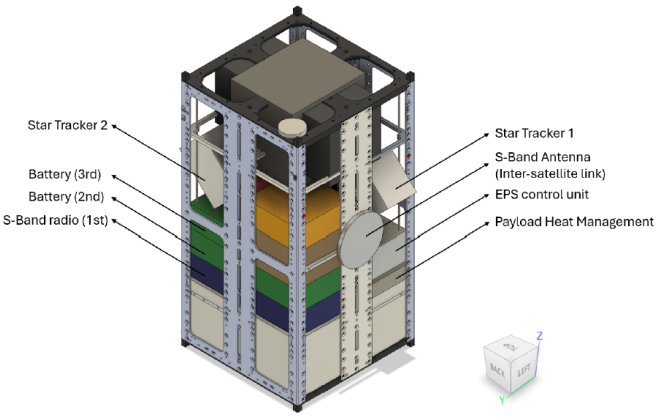

Figure 1.16: X-/Y+ view of the 16U4SBSP spacecraft without cover panels and solar array wings.[24]

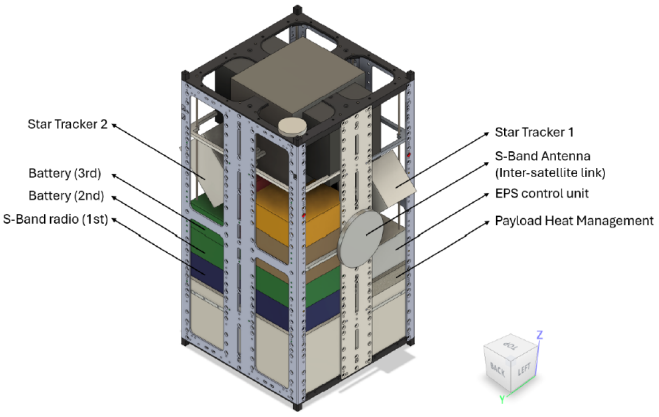

Figure 1.17: Z- view of the 16U4SBSP spacecraft without cover panels and solar array wings.[24]

Chapter 2

Dynamical Model

In this chapter, we shall examine in some detail the motion of a spacecraft around a celestial body. At any given time in its journey, the spacecraft is subject to several masses and may be experiencing external perturbations other than gravitational ones. The trajectory is described by the following differential equation: [6]

$$\ddot{\vec{r}} = -G(M+m)\frac{\vec{r}}{r^3} + \vec{p} \tag{2.1}$$

where G is the universal gravitational constant, M is the mass of the central body, m is the mass of the spacecraft, $\vec{r}$ is the position vector of the spacecraft relative to the central body, and $\vec{p}$ is the acceleration due to the perturbations. The first term of equation (2.1) refers to the Keplerian Orbits, they are the close-form solutions of the two-body equation of relative motion. Propagating the Keplerian Orbits means assuming that there are only two objects in space and that their spherically symmetric gravitational fields are the only source of interaction between them. Since this equation will be used to analyze the motion of satellites orbiting about the Sun, the mass of the orbiting body m will be much less than that of the Sun M. Hence, it is convenient to define the parameter μ called the gravitational parameter: [6]

$$\mu = GM \qquad \ddot{r} = -\mu\frac{r}{r^3} + p \tag{2.2}$$

In this chapter, we consider a few perturbation accelerations that cause the motion to deviate from a Keplerian orbit. The most significant perturbations are the ones due to non-spherical central body, atmospheric drag and solar radiation pressure.

2.1 Gravitational Perturbation

The Earth's shape deviates from a perfect sphere and is better described as an oblate ellipsoid, with greater mass concentrated around the equator rather than the polar regions. This non-uniform mass distribution results in various orbit perturbations and precessions.[6] Additionally, the Earth's non-homogeneous mass distribution leads to small irregular variations in the planet's gravity field, contributing to the complexities of gravitational interactions.

A typical starting point is to write the actual gravity potential as:[6]

$$V(r) = V_0(r) - R(r) \tag{2.3}$$

where $V_0(r)$ is the reference potential, typically the dominant point mass potential and $R(r)$ is the potential function due to all other variations from the spherical homogenous idealization of the Earth's mass distribution. [12]

Assuming that the Earth has an arbitrary shape and composition as shown in the figure below

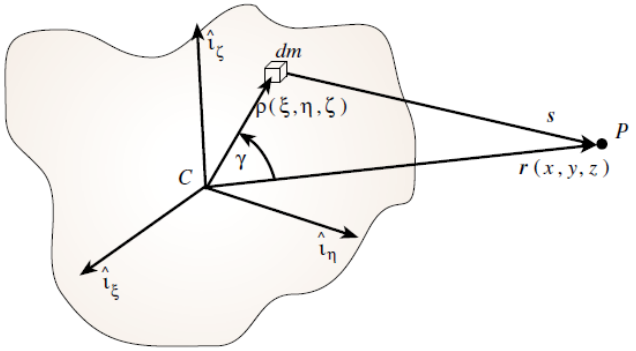

Figure 2.1: Gravity potential of an arbitrary body using cartesian coordinates [12]

the coordinate system $C : \{\hat{i}_\xi, \hat{i}_\eta, \hat{i}_\zeta\}$ is fixed with the body. The coordinate origin is not necessarily fixed to the center of mass at this point. The aim is to determine the gravitational potential that a spacecraft would experience at an arbitrary point P outside the body. [12]

The finite body can be considered as the sum of an infinite number of infinitesimal mass components dm. Each component is infinitesimal and it produces an elementary point differential mass gravitational field. The gravitation field dV at point P due to the differential mass dm is then given by [12]

$$dV = -\frac{G\ dm}{s} \tag{2.4}$$

where s is the magnitude of the relative position vector between dm and P. While using the relative position vector s to express the infinitesimal potential field

of dm, it is necessary to integrate this result to obtain the total gravitational field. This integration is simplified if we express all vectors in the body fixed frame C. [12] Hence

$$s = r - \rho \tag{2.5}$$

Note $s^2 = s \cdot s = r^2 + \rho^2 - 2\rho \cdot r$, leading to the law of cosines; the scalar relative distance s is then expressed as

$$s = r\left(1 + \left(\frac{\rho}{r}\right)^2 - 2\left(\frac{\rho}{r}\right) cos\gamma\right)^{\frac{1}{2}} \tag{2.6}$$

Substituting Eq.(2.6) into Eq.(2.4), the gravitational potential of dm is expressed as

$$dV(r, \rho, \gamma, dm) = -\frac{G\, dm}{r\left(1 + \left(\frac{\rho}{r}\right)^2 - 2\left(\frac{\rho}{r}\right) cos\gamma\right)^{\frac{1}{2}}} \tag{2.7}$$

The next step is to integrate the gravitational potential field of the entire body, but we can simplify these calculations by using the Legendre polynomials $P_k(\nu)$ which are a set of orthogonal polynomials. Taking $(1 - 2\nu x - x^2)^{-\frac{1}{2}}$, we can expand it using the binomial theorem and then collect on x^k. [12] It leads to

$$(1 - 2\nu x - x^2)^{-\frac{1}{2}} = \sum_{k=0}^{\infty} P_k(\nu) x^k \tag{2.8}$$

By Eq. (2.8) it is possible to deduce recursively the first four Legendre polynomials, given by

$$P_0(\nu) = 1 \tag{2.9a}$$

$$P_1(\nu) = \nu \tag{2.9b}$$

$$P_2(\nu) = \frac{(3\nu^2 - 1)}{2} \tag{2.9c}$$

$$P_3(\nu) = \frac{(5\nu^3 - 3\nu)}{2} \tag{2.9d}$$

These polynomials satisfy the zero mean condition and the orthogonality condition.[12] They had been obtained by applying the recursive formula[12]

$$P_{n+1}(\nu) = \frac{2n+1}{n+1}\nu P_n(\nu) - \frac{n}{n+1} P_{n-1}(\nu) \tag{2.10}$$

Now it is easier to use the Legendre identity in Eq. (2.8) and to rewrite the gravitational potential of dm as an infinite sum

$$dV(r, \rho, \gamma, dm) = -\frac{G\ dm}{r} \sum_{k=0}^{\infty} \left(\frac{\rho}{r}\right)^k P_k(cos\gamma) \tag{2.11}$$

It is assumed that the ratio ρ/r is less than one, which means that the point of interest P is outside of the body.

Finally, it is possible to integrate over the entire body. By doing that, the dependence on ρ, γ and dm is lost. We obtain a general solution of the gravitation potential field of an arbitrary body B [12]

$$V(r) = -\frac{G\,m}{r} - \frac{G}{r}\sum_{k=1}^{\infty}\int\int\int_{B}\left(\frac{\rho}{r}\right)^{k} P_k(cos\gamma)dm \tag{2.12}$$

This approach applies to a body of any shape and density variation, with the only limitation being that the coordinate system C is fixed within the body. It is noticeable that using the Legendre polynomials in the infinite series expression allows us to break down the gravity field components as a series of less relevant contributions. Thanks to the condition $\rho/r < 1$, the contribution of the k-th element, which is multiplied by $(\rho/r)^k$, goes to zero as k grows infinitely large. As $r \to \infty$, in Eq. (2.12) the first term is the most relevant. Hence, as the distance r increases, the potential of any arbitrary body converges towards that of a point mass. [12]

There are various methods to model the gravitational potential field. For example, MacCullagh's approximation uses the body inertias. In this analysis, we use the spherical harmonic gravity potential method which describes the gravity potential field in terms of a spherical harmonic series. [17]

Given an arbitrary body, it is possible to express the gravity potential in terms of spherical coordinates. The infinitesimal body mass position can be written as $\vec{\rho} = \vec{\rho}(\rho, \lambda, \beta)$. In the same way, the position vector of the point P is written as $\vec{r} = \vec{r}(r, \theta, \phi)$. The angle γ is the one between $\vec{\rho}$ and $\vec{r}$ position vectors. [12]

For the arbitrary body B, the general gravity potential field expression is:

$$V(r) = -\frac{G\,m}{r} - \frac{G}{r}\sum_{k=1}^{\infty}\int\int\int_{B}\left(\frac{\rho}{r}\right)^{k} P_k(cos\gamma)dm \tag{2.13}$$

It is possible to express the differential mass element dm using the body-fixed spherical coordinates ρ, λ and β

$$dm = D(\rho, \lambda, \beta)\rho^2 cos\beta\, d\rho\, d\beta\, d\lambda \tag{2.14}$$

with $D = D(\rho, \lambda, \beta)$ being the local density of the arbitrary body B. [12] We can use the spherical trigonometric law of cosines

$$cos\gamma = sin\phi\, sin\beta + cos\phi\, cos\beta\, cos(\theta - \lambda) \tag{2.15}$$

Making use of the *associated Legendre Functions* [2] will simplify the development of the gravitational spherical harmonic series.

$$P_k^j(\nu) = (1-\nu^2)^{\frac{1}{2}j}\frac{d^j}{d\nu^j}(P_k(\nu)) \tag{2.16}$$

The parameter j is referred to as the order of the associated Legendre function, while k is referred to as the degree. Note that zeroth-order associated Legendre functions are the Legendre polynomials. [12]

$$P_k^0(\nu) \equiv P_k(\nu) \tag{2.17}$$

Furthermore, since $P_k(\nu)$ is a polynomial expression of degree k, then it must be true that

$$P_k^j = 0 \qquad \forall j > k \tag{2.18}$$

The associated Legendre functions for Legendre polynomials up to third degree as explicitly given as:

$$P_1^1(\nu) = \sqrt{1-\nu^2} \qquad P_2^1(\nu) = 3\nu\sqrt{1-\nu^2} \qquad P_3^1(\nu) = \frac{3}{2}\sqrt{1-\nu^2}(5\nu^2-1) \tag{2.19a}$$

$$P_2^2(\nu) = 3(1-\nu^2) \qquad P_3^2(\nu) = 15\nu(1-\nu^2) \tag{2.19b}$$

$$P_3^3(\nu) = 15(1-\nu^2)^{\frac{3}{2}} \tag{2.19c}$$

For our analysis, we set $\nu = sin\,\alpha$. Hence, the corresponding associated Legendre functions up to the second degree are [12]

$$P_1^1(sin\,\alpha) = cos\,\alpha \tag{2.20a}$$

$$P_2^1(sin\,\alpha) = 3\,sin\,\alpha\,cos\,\alpha \tag{2.20b}$$

$$P_2^2(sin\,\alpha) = 3\,cos^2\,\alpha \tag{2.20c}$$

Next step is to notice that the first Legendre polynomial can now be written in terms of associated Legendre functions by making use of the spherical trigonometric identity in Eq. (2.15).

By performing all the calculations, the following formula of the gravitational potential field is obtained, expressed in terms of spherical coordinates as

$$V(r,\phi,\theta) = -\frac{Gm}{r} - \sum_{k=1}^{\infty}\frac{1}{r^{k+1}}\Bigg(A_kP_k\,(sin\phi) + \sum_{j=1}^{k}P_k^j(sin\phi)\big(B_k^j cos\,j\theta + C_k^j sin\,j\theta\big)\Bigg) \tag{2.21}$$

where the coefficients A_k are named zonal harmonics, B_k^j and C_k^j are named sectorial harmonics. [12]

For the case of a body with rotational symmetry, the gravitational potential field function V is expressed as the sum of the point mass contribution and the zonal harmonics. [12]

$$V(r,\phi) = -\frac{Gm}{r} - \sum_{k=2}^{\infty} \frac{1}{r^{k+1}} A_k P_k \ (sin\phi) \tag{2.22}$$

Note that the mass distribution is not changed when a symmetric body rotates about its symmetry axis, so the rotation of this body about the symmetry axis does not affect the gravity field. Therefore, the Earth rotation does not change the gravity field if rotational symmetry is assumed. This greatly simplified the equations of motion. [12]

The conventional definition in orbital mechanics for the zonal gravitational harmonics is [12]

$$J_k = -\frac{A_k}{r_{eq}^k} \tag{2.23}$$

with r_{eq} is the equatorial radius of the body B. So now the gravity potential V can be expressed as its most famous form:

$$V(r,\phi) = -\frac{Gm}{r}\left[1 - \sum_{k=2}^{\infty} \left(\frac{r_{eq}}{r}\right)^k J_k P_k \ sin\phi\right] \tag{2.24}$$

From this equation, it can be noted that as the point P moves away from the body B (i.e. $r \to \infty$), the effect of the zonal harmonics quickly lowers to zero. [12]

The value of J_k are tipically obtained by observing the motion of a satellite about the body and then extracting these harmonics through an estimation method. It is impossible to obtain values for J_k through integration of its analytical expression due to the inaccurate knowledge of the Earth's mass distribution $D(\rho, \lambda, \beta)$. For the Earth, the first six zonal harmonics are: [17]

$$J_2 = 0.00108263$$
$$J_3 = -2.33936(10^{-3})J_2$$
$$J_4 = -1.49601(10^{-3})J_2$$
$$J_5 = -0.20995(10^{-3})J_2$$
$$J_6 = 0.49941(10^{-3})J_2$$

The J_2 harmonic refers to the oblateness perturbation and it is the dominant harmonic.It is the cause of a highly noticeable precession of the near-Earth satellite

orbits. In this analysis it is considered the perturbations from J_2 to J_4. At this point, we can set $\mu = G\,m$.

The gravitational perturbation function $R(r)$ is given by [12]

$$\begin{aligned} R(\vec{r}) = &- \frac{J_2}{2}\frac{\mu}{r}\left(\frac{r_{eq}}{r}\right)^2 (3sin^2\phi - 1) \\ &- \frac{J_3}{2}\frac{\mu}{r}\left(\frac{r_{eq}}{r}\right)^3 (5sin^3\phi - 3sin\phi) \\ &- \frac{J_4}{8}\frac{\mu}{r}\left(\frac{r_{eq}}{r}\right)^4 (35sin^4\phi - 30sin^2\phi + 3) \end{aligned} \tag{2.25}$$

Then, the gradient of $R(\vec{r})$ is computed to obtain the perturbing acceleration $\vec{a}_{j_i}$ due to J_i, in terms of inertial cartesian coordinates $\vec{a} = -\nabla R(\vec{r})$. It is used $z/r = sin\phi$:

$$\vec{a}_{J2} = -\frac{3}{2}J_2\left(\frac{\mu}{r^2}\right)\left(\frac{r_{eq}}{r}\right)^2 \begin{pmatrix} \left(1 - 5\left(\frac{z}{r}\right)^2\right)\frac{x}{r} \\ \left(1 - 5\left(\frac{z}{r}\right)^2\right)\frac{y}{r} \\ \left(3 - 5\left(\frac{z}{r}\right)^2\right)\frac{z}{r} \end{pmatrix} \tag{2.26}$$

$$\vec{a}_{J3} = -\frac{1}{2}J_3\left(\frac{\mu}{r^2}\right)\left(\frac{r_{eq}}{r}\right)^3 \begin{pmatrix} 5\left(7\left(\frac{z}{r}\right)^3 - 3\left(\frac{z}{r}\right)\right)\frac{x}{r} \\ 5\left(7\left(\frac{z}{r}\right)^3 - 3\left(\frac{z}{r}\right)\right)\frac{y}{r} \\ 3\left(10\left(\frac{z}{r}\right)^2 - \frac{35}{5}\left(\frac{z}{r}\right)^4 - 1\right) \end{pmatrix} \tag{2.27}$$

$$\vec{a}_{J4} = -\frac{5}{8}J_4\left(\frac{\mu}{r^2}\right)\left(\frac{r_{eq}}{r}\right)^4 \begin{pmatrix} \left(3 - 42\left(\frac{z}{r}\right)^2 + 63\left(\frac{z}{r}\right)^4\right)\frac{x}{r} \\ \left(3 - 42\left(\frac{z}{r}\right)^2 + 63\left(\frac{z}{r}\right)^4\right)\frac{y}{r} \\ -\left(15 - 70\left(\frac{z}{r}\right)^2 + 63\left(\frac{z}{r}\right)^4\right)\frac{z}{r} \end{pmatrix} \tag{2.28}$$

[12]

2.2 Atmospheric Drag

The atmospheric drag poses a significant challenge to spacecraft trajectories, particularly at lower altitudes. On Earth, a 99.9999% of the atmosphere is concentrated below an altitude of 100 km. [6] This dense lower atmosphere exerts a substantial drag on spacecraft, necessitating careful trajectory and thermal management strategies.

The effects of atmospheric drag are manifold. Not only does it reduce the spacecraft's velocity and altitude, but it also generates intense heat through aerodynamic heating. This phenomenon can lead to temperatures exceeding $2000°C$ [6], posing

a grave risk of thermal damage and even complete incineration if the spacecraft lacks adequate thermal protection systems. Therefore, mitigating the impact of atmospheric drag is paramount for the safety and success of space missions.

The atmosphere has been modelized by various numerical models, describing how the temperature, pressure and density change across different ranges of altitude. In this analysis, it has been taken into account the USSA76, US Standard Atmospherere 1976 (NOAA/NASA/USAF, 1976) [1]. This model provides the atmospheric density profile from sea level to an altitude of 1000 km, as shown in Fig. 2.2.

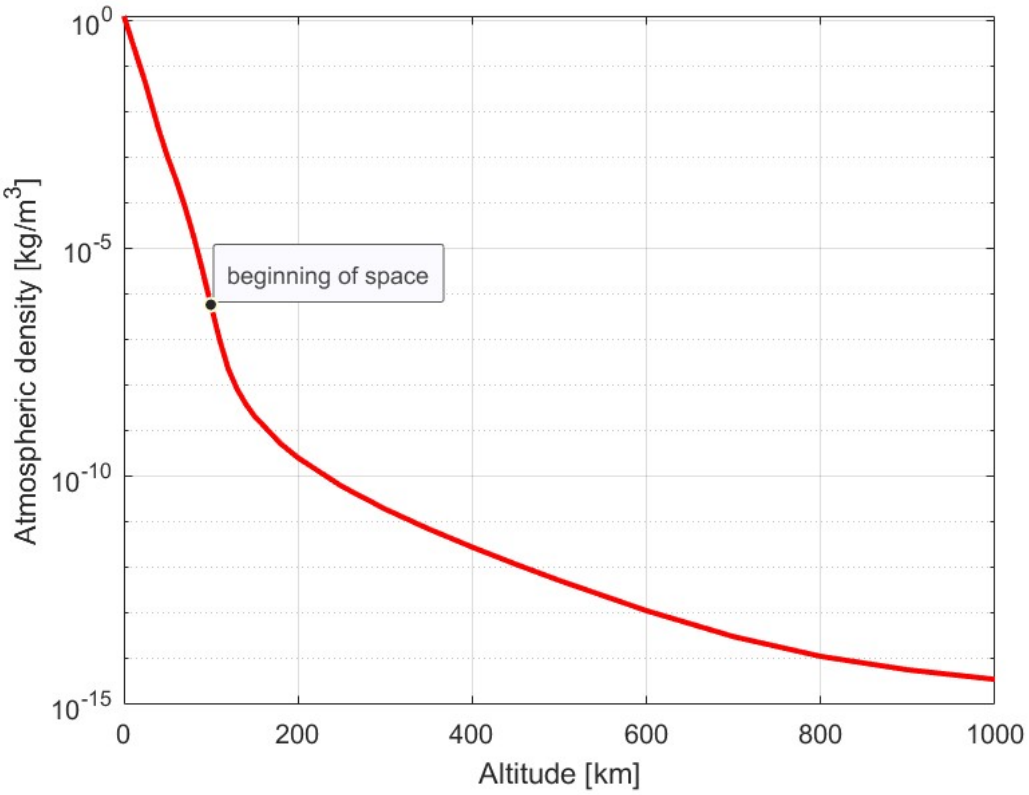

Figure 2.2: USSA76 Atmospheric density versus altitude

This figure is obtained by selecting the density ρ_i at 28 altitudes z_i in the USSA76 table. Then, these values are interpolated with the exponential functions:[6]

$$\rho(z) = \rho_i \cdot e^{-\frac{(z-z_i)}{H_i}} \tag{2.29}$$

where $z_i \leq z < z_{i+1}$ and $H_i = (z_{i+1} - z_i)/ln(\rho_{i+1}/\rho_i)$.

According to USSA76, the atmosphere is conceptualized as a spherically symmetrical gaseous envelope spanning 1000 kilometers around the Earth. Its characteristics remain constant and reflect a state of moderate solar activity. The hypothetical changes in properties with altitude approximate the year-round conditions at mid-latitudes, averaged over multiple years. While the model offers realistic atmospheric density values, they may not precisely align with actual observations at specific locations or times.

In order to evaluate the effect of this perturbation, it is necessary to start with the calculation of the spacecraft velocity relative to the atmosphere [6]

$$\vec{v}_{rel} = \vec{v} - \vec{v}_{atm} \tag{2.30}$$

where $\vec{v}$ is the inertial velocity of the spacecraft and $\vec{v}_{atm}$ is the velocity of the atmosphere in that point. [6] The atmosphere rotates with the Earth with an angular velocity ω_E relative to the geocentric equatorial frame. Therefore $\vec{v}_{atm} = \vec{\omega}_E \times \vec{r}$.

$$\vec{v}_{rel} = \vec{v} - \vec{\omega}_E \times \vec{r} \tag{2.31}$$

Keeping in mind that the drag acts in the opposite direction to the relative velocity of the object, it is possible to say that:

$$\vec{D} = -D\hat{v}_{rel} \tag{2.32}$$

where $\hat{v}_{rel}$ is the unit vector in the direction of the relative velocity, and

$$D = \frac{1}{2}\rho v_{rel}^2 C_D A \tag{2.33}$$

where A is the frontal area of the spacecraft (the area normal to the relative velocity vector) and C_D is the dimensionless drag coefficient.

It is easy to find the perturbing acceleration from the drag force as $\vec{p} = \vec{D}/m$ with m the spacecraft's mass

$$\vec{p} = -\frac{1}{2}\rho v_{rel}\left(\frac{C_D A}{m}\right)\vec{v}_{rel} \tag{2.34}$$

2.3 Solar Radiation Pressure

The solar radiation is composed of photons, which are elementary particles made of waves of electromagnetic radiation. The photons are massless and they travel at the speed of light ($c = 2.998 \cdot 10^8 m/s$)[18]. They have an energy and a momentum that are not equal to zero, even though their mass is zero. The energy (in Joules)

of a photon is hf, where f is the frequency of its electromagnetic wave (in Hertz), and h is the Planck constant ($h = 6.626 \cdot 10^{-34} J \cdot s$). The momentum of a photon is hf/c, its energy divided by the speed of light.

The light that illuminates the spacecraft is the one coming from the visible surface of the Sun, the photosphere. It acts like a blackbody emitting radiation, spanning from low-energy radio waves on up the visible spectrum and beyond to high-energy ultraviolet light and X-rays. For studying the intensity of the radiation, it is useful to consider the Stefan-Boltzmann law [6]

$$S = \sigma T^4 \tag{2.35}$$

where $\sigma = 5.670 \cdot 10^{-8}\ W/m^2K^4$ is the Stefan-Boltzmann constant, T is the temperature of the blackbody. The photosphere has a temperature of $T = 5777K$, so the intensity radiated from the Sun is :

$$S_0 = 5.670 \cdot 10^{-8}(5777)^4 = 63.15 \cdot 10^6\ W/m^2 \tag{2.36}$$

To evaluate the intensity of solar radiation that reaches the satellite it is necessary to consider the radius of photosphere R_0 and the distance of the Sun's center from the satellite R_{sat} [6]

$$S = S_0 \left(\frac{R_0}{R_{sat}} \right)^2 \tag{2.37}$$

The distance from the satellite to the center of the Sun changes over time. In order to calculate R_{sat}, it is essential to know the exact position of the Sun, as explained in section 2.3.1.

The photosphere's radius is $R_0 = 696000\ km$. R_{sat} can be calculated by

$$\vec{R}_{sat} = \vec{R}_{sun} - \vec{R} \tag{2.38}$$

where R_{sun} and R are the positions of the Sun and the satellite in the geocentric equatorial frame.

S is the energy flux (energy per unit time per unit area) transported by photons across a surface normal to the radiation direction. In order to find the momentum flux, which is the solar radiation pressure P_{SR}, it is necessary to divide S by the speed of light [6]

$$P_{SR} = \frac{S}{c} \tag{2.39}$$

Let's assume that the spacecraft is a sphere of radius R, adopting the cannonball model. Then the perturbing force $\vec{F}$ on the satellite due to the radiation pressure $\frac{S}{c}$ is

$$\vec{F} = -\mu \frac{S}{c} C_R A_{SC} \hat{u} \tag{2.40}$$

where $\hat{u}$ is the unit vector pointing from the satellite toward the Sun. [6] The negative sign indicates that the solar radiation force is directed outward from the Sun. A_{SC} is the absorbing area of the spacecraft, which is πR^2 for the cannonball model. ν is the shadow function, which has the value 0 if the satellite is in the Earth's shadow; otherwise $\nu = 1$. C_R is the radiation pressure coefficient, which lies between 1 and 2. When the surface acts as a blackbody, absorbing all momentum from the incident photon stream, the value of C_R is 1 and it raises the pressure described in Eq. (2.39). When C_R equals 2, all incident radiation is reflected, reversing the direction of incoming photon momentum and thereby doubling the force exerted on the satellite. [6]

Being m the mass of the satellite, then the perturbing acceleration $\vec{p}$ due to solar radiation di $\vec{F}/m$ or

$$\vec{p} = -p_{SR}\hat{u} \tag{2.41}$$

where the magnitude of the perturbation is

$$p_{SR} = \nu \frac{S}{c} \frac{C_R A_{SC}}{m} \tag{2.42}$$

As shown in Eq.(2.42) the magnitude of solar radiation pressure perturbation depends on the satellite's area-to-mass ratio $A_{SC/m}$. This mean that satellite that are very large but with very low mass (such as solar sails) are the most affected by solar radiation pressure. The solar radiation pressure influences the most at higher orbital altitudes, where the atmospheric drag is comparatively negligible. [6]

2.3.1 Solar Position

As previously discussed, it is fundamental to know the solar position at which the analysis is performed. This helps us to evaluate the distance satellite-sun and to estimate the shadow factor ν. The date of the analysis can be translated to a Julian Day number. The Julian Day number is the number of days since noon UT on January 1, 4713 BCE. The origin of this timescale is placed in ancient times so we need not deal with positive and negative dates, except for prehistoric events. The Julian day count is a continuous and uniform count of days, without any consideration for leap years or different numbers of days in different months. The number of days between two events is found by simply subtracting the Julian day of one from that of the other. [6]

J_0 is the symbol for the Julian day number at 0h UT (that is halfway into the Julian day), at any other UT the Julian day is given by [23]

$$JD = J_0 + \frac{UT}{24} \tag{2.43}$$

There exist many different algorithms and tables for obtaining the value of J_0 from the ordinary year (y), month (m) and day (d). The one used in this analysis can be found in Boulet (1991) [3], it consists of the formula:

$$J_0 = 367\ y - INT\left\{\frac{7\left[y + INT\left(\frac{m+9}{12}\right)\right]}{4}\right\} + INT\left(\frac{275\ m}{9}\right) + d + 1\ 721\ 013{,}5 \quad (2.44)$$

where y, m and d are integers lying in the following ranges:

$$1901 \leq y \leq 2099$$
$$1 \leq m \leq 12$$
$$1 \leq d \leq 31$$

$INT(x)$ means retaining only the integer portion of x, without rounding. [23]

From the number JD corresponding to the date of the analysis, it is possible to calculate the Solar position. To do that, let's start with the evaluation of the obliquity ε and solar ecliptic longitude λ, both of them appear into the expression for the unit vector pointing at the position of the Sun $\hat{u}$. [23]

According to the *The Astronomical Almanac* [25] the apparent solar ecliptic longitude (in degrees) is given by the formula

$$\lambda = L + 1.915^\circ sin M + 0.0200^\circ sin 2M \qquad (0^\circ \leq \lambda \leq 360^\circ) \quad (2.45)$$

where L and M are, respectively, the mean longitude and the mean anomaly of the Sun, both in degrees

$$L = 280.459^\circ + 0.98564736^\circ\ n \qquad (0^\circ \leq L \leq 360^\circ) \quad (2.46)$$
$$M = 357.529^\circ + 0.98560023^\circ\ n \qquad (0^\circ \leq M \leq 360^\circ) \quad (2.47)$$

n is the number of days since JD2000,

$$n = JD - 2\,451\,545.0 \quad (2.48)$$

The above formulas for L, M and λ may deliver angles outside the range 0° to 360°. In those cases, the angle has to be reduced by appropriate multiples of 360° . [25]

The obliquity in degrees is

$$\varepsilon = 23.439^\circ - 3.56(10^{-7})n \quad (2.49)$$

Finally, the distance r_s from the Earth to the Sun is

$$r_s = (1.00014 - 0.01671\, cos M - 0.000140\, cos 2M) AU \quad (2.50)$$

where AU is the astronomical unit ($1\ AU = 149\,597\,870.691 km$).

2.3.2 Shadow Function

In the formula of the solar radiation pressure's vector, it appears the shadow function. It has the value of $\nu = 0$ if the satellite is in the Earth's shadow; otherwise $\nu = 1$. [6]

Therefore, it is necessary to evaluate the shadow function at every time of the orbit propagation. It is noticeable, indeed, that if the satellite is not receiving solar illumination then it will not be vulnerable to perturbations due to solar radiation pressure. [6]

To estimate when the satellite condition of illumination, we can use the following simple procedure. [29]

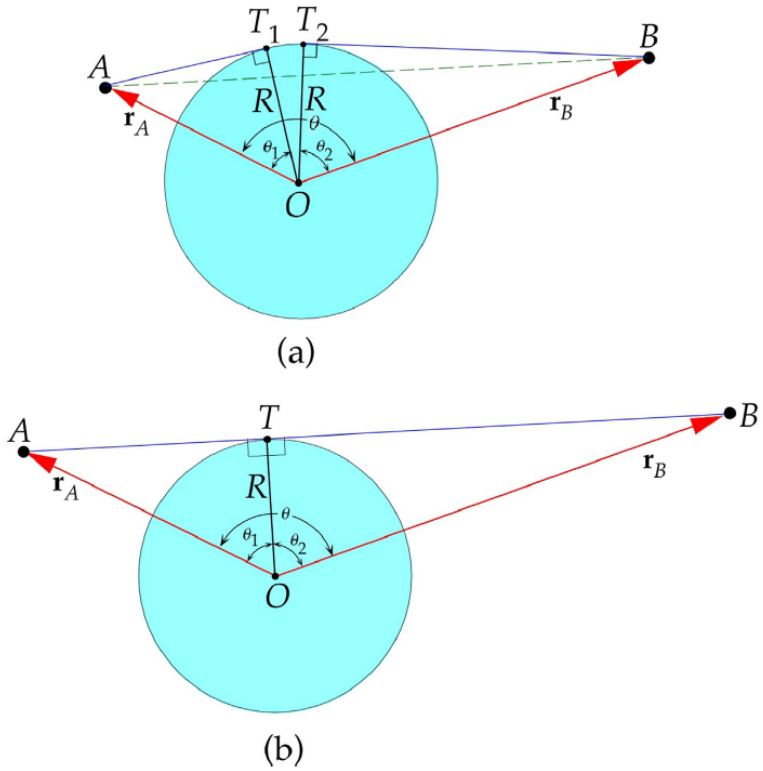

Figure 2.3: a) Situation of satellite in shadow. b) Situation of satellite in light. [6]

Let's consider two object A and B, orbiting around a central body of radius R. In this case, A and B will be the satellite and the Sun, while the central body will be the Earth. The two position vectors $\vec{r}_A$ and $\vec{r}_B$ define a plane, represented in Fig.2.3. The angle θ between the two position vectors may be found from the dot product operation. [29]

$$\theta = cos^{-1}\left(\frac{\vec{r}_A \cdot \vec{r}_B}{r_A r_B}\right) \tag{2.51}$$

In the Fig.2.3 two points of tangency to the Earth's circumference are displayed, T_1 and T_2. The radii OT_1 and OT_2 along with the tangent lines AT_1 and BT_2 and the position vectors $\vec{r}_A$ and $\vec{r}_B$ comprise the two right triangles OAT_1 and OBT_2. The angles at the vertex O of these two triangles are obtained from [29]

$$\theta_1 = cos^{-1}\left(\frac{R}{r_A}\right) \qquad \theta_2 = cos^{-1}\left(\frac{R}{r_B}\right) \tag{2.52}$$

Therefore, if the line AB intersects the central body (as in Fig.2.3-a), it means there is no line of sight and that the satellite is not illuminated. [29]

$$\theta_1 + \theta_2 < \theta \qquad \rightarrow \qquad \nu = 0 \tag{2.53}$$

Meanwhile, if the line does not intersect the central body, it means that the satellite is illuminated by the Sun. [29]

$$\theta_1 + \theta_2 \geq \theta \qquad \rightarrow \qquad \nu = 1 \tag{2.54}$$

Chapter 3

Satellite Formation in Heliotropic Orbit

The scope of the 16U4SBSP mission is to demonstrate the feasibility of Space-Based Solar Power (SBSP) using CubeSats in a distributed swarm configuration from Earth orbit. The mission aims to validate with a small-scale mission the beamforming power transmission model developed by the consortium and, in this way, confirm that it is feasible and convenient to provide SBSP by means of a larger constellation of spacecraft (larger both in terms of number and size). This concept uses seven 16U CubeSats in order to deliver 1kW-scale wireless energy via radio-frequency (RF) beaming. The transmission can be utilized for both space-to-ground and space-to-space applications.

Using the technology of SBSP can be a fundamental key in time of crisis. More frequent critical events had forced us to search for emergency backup power sources. Industries, household and hospitals may be forced to go out of service at any time, leading to economic and social losses. Space-based emergency supply systems, as aimed by the intended mission concept, shall in the short-term provide a sustainable, flexible and redundant solution to the above mentioned problems.

Therefore, for this application the power supply is primarily needed at night, in order to complement ground-based solar arrays. Indeed the types of orbit which offer significant advantages for this case are the ones that have a fixed orientation with respect to the Sun. The types of orbit that have been taken into account are: Sun-synchronous and Heliotropic orbit.

The Sun-synchronous orbit is a near-polar orbit type that allows a satellite to fly over a specific point on Earth's surface at the same local solar time. [7] This trait is attained by maintaining a precise inclination and altitude, causing the orbit's Right Ascension of the Ascending Node (Ω) to precess at the same rate as Earth orbits around the Sun, thereby synchronizing with the solar cycle. The choice of this type of orbit for the mission can maximizes illumination during operational periods and minimizes the energy storage requirements, as the satellites are strategically

positioned to efficiently leverage sunlight.

In the following section, an analysis of the stability of CubeSat formations in a heliotropic orbit will be presented to determine if this orbit could be a better solution than a Sun-synchronous orbit.

3.1 Heliotropic Orbit

Solar radiation pressure (SRP) and the uneven distribution of gravitational forces from the central body are among the most significant disturbances affecting the orbital dynamics of spacecraft. Various strategies have been devised to maintain stable spacecraft orbits, depending on whether SRP or gravitational irregularities predominate at the given altitude. In cases where solar radiation pressure is the primary factor, potential orbit options include terminator orbits, equatorial Sun-frozen orbits, and quasi-terminator orbits.[8] Conversely, when the central body's gravitational irregularities are more influential, Sun-synchronous orbits and precessing orbits are among the solutions of interest.[8] Additionally, for situations where an irregular gravity field dominates, frozen orbits and body-fixed periodic orbits become particularly relevant.[8]

Sun-frozen and Heliotropic orbits are two orbital categories that can take advantage of strong solar radiation pressure and body oblateness perturbations. These two groups of orbit overlap: Heliotropic orbit situated in the equatorial plane are Sun-frozen. [8]

Commonly, a frozen-eccentricity orbit requires that the eccentricity vector be constant in time. [29] At the same way, a Sun-frozen orbit requires that the eccentricity vector is constant with respect to the Sun line.

Heliotropic orbits typically display eccentricity, with their periapsis positioned on the opposite side of the Sun from the body. Conversely, Antiheliotropic orbits have their periapsis directed toward the Sun. These orbits are characterized by an eccentricity selected to ensure that the combined effects of solar radiation pressure and oblateness perturbations result in the average alignment of the orbit's apoapsis toward the Sun. The fundamental characteristics of a Heliotropic orbit are represented in Fig.3.1. Heliotropic orbits belong to a category of orbits that was initially identified during the examination of the dynamics of planetary dust orbits, with the term coined specifically within the study of Saturnian ring dynamics. [8]

The analysis of the Heliotropic solution begins by examining the secular variation of the line of nodes and the line of apsides due to Earth's oblateness. In this chapter, the identification of Heliotropic orbits is limited to gravitational effects, considering only the J2 term. [30] However, a comprehensive analysis would require including higher harmonic terms and solar pressure. Thus, this analysis provides an initial indication of potential solutions for identifying Heliotropic orbits.

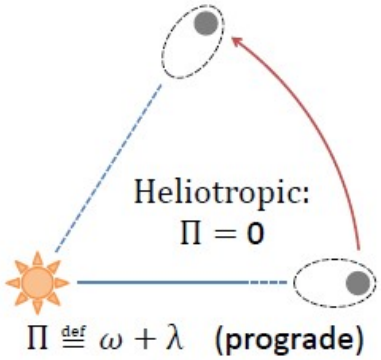

Figure 3.1: Heliotropic orbit definition
[8]

The secular variations of the right ascension of the ascension of the ascending node and the argument of the perigee due to J2 can be written as: [29]

$$\dot{\Omega} = -\frac{3nR_E^2 J_2}{2p^2} cos\, i \tag{3.1}$$

$$\dot{\omega} = \frac{3nR_E^2 J_2}{4p^2} \left(4 - 5sin^2 i\right) \tag{3.2}$$

By combining Eqs. 3.1 and 3.2 it is found the simple Sun-Synchronous condition:

$$\Delta_{SS} = \frac{3nR_E^2 J_2}{4p^2} \left(4 - 5sin^2 i\right) - \frac{3nR_E^2 J_2}{2p^2} cos\, i - \frac{2\pi}{P_E} = 0 \tag{3.3}$$

Eq. 3.3 is valid for prograde orbits, i.e. with an inclination from 0° to 90°. For retrograde orbits, the helio-synchronicity condition reads:

$$\Delta_{SS} = -\frac{3nR_E^2 J_2}{4p^2} \left(4 - 5sin^2 i\right) - \frac{3nR_E^2 J_2}{2p^2} cos\, i - \frac{2\pi}{P_E} = 0 \tag{3.4}$$

In the following, the term heliotropic will be used to identify orbits that satisfy conditions 3.3 or 3.4.

Figure 3.2 shows the level curves of Δ_{SS}. It has been assumed a constant perigee at an altitude of 500 km, the graph represents curves for different inclinations and altitudes of the apogee. The red curves, corresponding to $\Delta_{SS} = 0$, signify the Heliotropic orbits.

Initially, the analysis focuses on a Heliotropic orbit with a perigee altitude of 500 km. This selection facilitates a more convenient comparison and allows for a trade-off with the 500 km circular Sun-synchronous orbit.

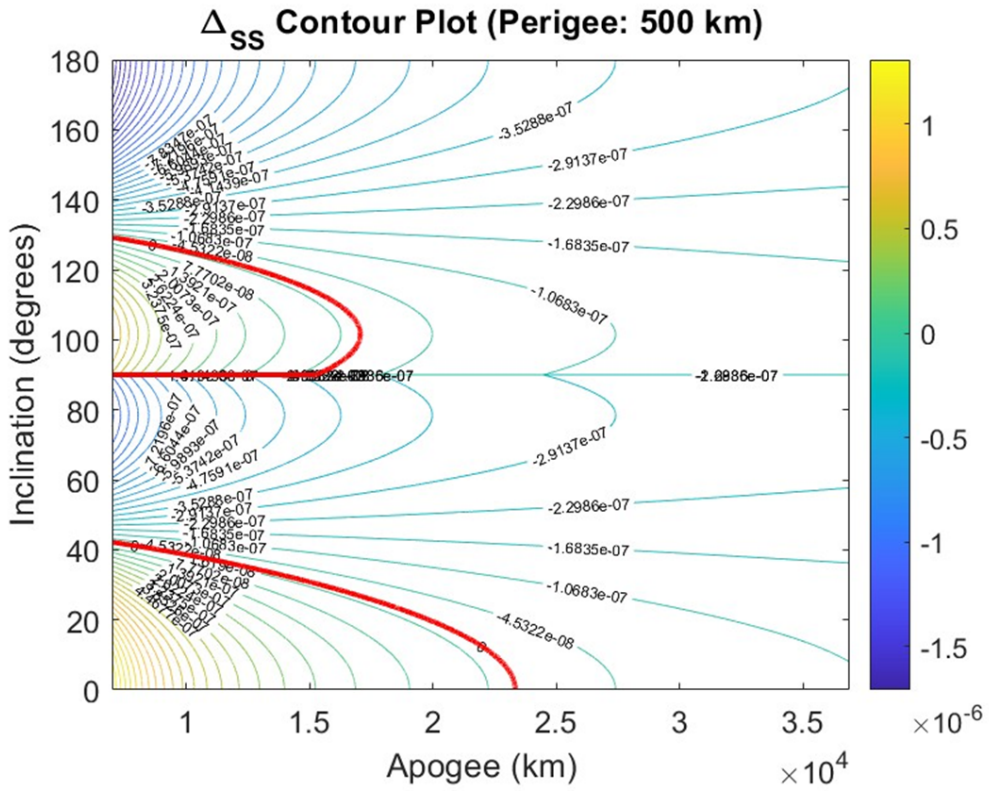

Figure 3.2: Heliotropic resonant solutions for a perigee altitude of 500 km

Using Figure 3.2 as a reference, it has been possible to select a specific combination of inclination and apogee's altitude within the family group of Heliotropic orbits (red line in the graph) that fulfills the conditions outlined Eqs. 3.3 or 3.4.

The possible range of inclinations spans from about 0° to 40° and from 90° to 130°. The equatorial plane has been discarded because of the lack of Ground Station in those areas. Indeed, it is more convenient to select a polar inclination, because there are more Ground Stations available and because this choice leads to an easier comparison to the other candidate orbit. Therefore, the classical orbital elements, described in Tab.3.1, were selected to define the chosen Heliotropic orbit.

Perigee radius	r_p	6 878 km
Apogee radius	r_a	16 903,20 km
Semimajor axis	a	11 890,6 km
Inclination	i	97,4014 °
RAAN	Ω	0 °
omega	ω	0 °
theta	θ	0 °

Table 3.1: Classical orbital parameters defining the chosen Heliotropic orbit

Defining the spacecraft's characteristics is crucial for propagating the dynamical model. In this analysis, the spacecraft's shape is approximated using the "Cannonball Model"[19] . This simplification offers the easiest way to estimate solar radiation pressure and drag perturbations. Widely adopted in preliminary mission analysis (Phase 0/A), this model provides a first-order estimation of these perturbations' impact. It treats the spacecraft's shape as a sphere with a constant reflectivity coefficient and drag coefficient along its surface.

In Tab. 3.2, the main characteristics of the spacecraft are summarized.

Drag Coefficient	C_D	2,2
Reflectivity Coefficient	C_R	1,2
Area/mass ratio	A/m	0,02 m^2/kg

Table 3.2: Characteristics of the approximated sphere-shaped spacecraft

The orbit can be represented in the ECI frame as shown in Fig. 3.3, the Earth-Centered Inertial reference frame. This reference frame does not rotate with the Earth but maintains a fixed orientation relative to distant stars. [14] The origin of the ECI frame is located at the Earth's center of mass and is composed of three orthogonal axes. The x-axis is aligned with the vernal equinox, providing a fixed direction in space that intersects both the Earth's equatorial plane and the ecliptic plane. The y-axis extends perpendicularly from the x-axis within the equatorial plane, pointing east. The z-axis is perpendicular to the Earth's equatorial plane, extending towards the North Pole, thus completing a right-handed coordinate system.

At this point, it is crucial to determine whether this orbit is stable or if it will decay within the mission's duration (approximately 180 days). To assess this, we utilize the dynamical model described in Chapter 2, which accounts for perturbations due to atmospheric drag, solar radiation pressure, and Earth's oblateness. Running the analysis for 180 days, the resulting graph shown in Fig. 3.4 illustrates the evolution of the perigee and apogee's altitudes. From Fig. 3.4, it is evident that the altitudes of both the perigee and apogee remain quite constant and do not decay. This provides valuable insight into the stability of the orbit for a generic spacecraft.

Furthermore, it is useful to have a basic understanding of the magnitude of the perturbations that act upon the spacecraft in the selected Heliotropic orbit. In Fig.3.5 is shown how the three main perturbations analyzed act in each of the three directions of the RTN frame [4]. The Radial-Tangential-Normal (RTN) reference frame offers a localized view of object motion in orbit around the Earth. This frame is used for describing the relative motion of satellites; its axes are oriented based on the instantaneous position and velocity of a reference satellite or object. The Radial axis points from the center of the Earth directly towards the object. The Tangential (or Along-Track) axis lies in the plane of the object's orbit, pointing in the direction

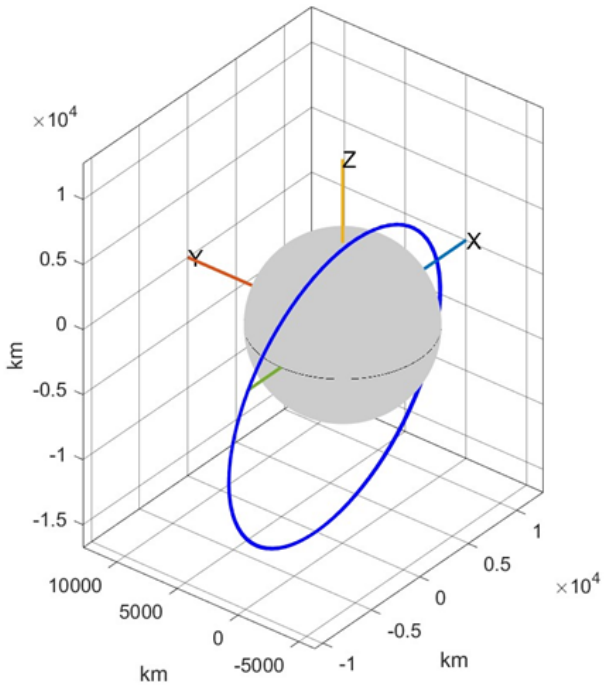

Figure 3.3: Heliotropic polar orbit of 500 km perigee altitude

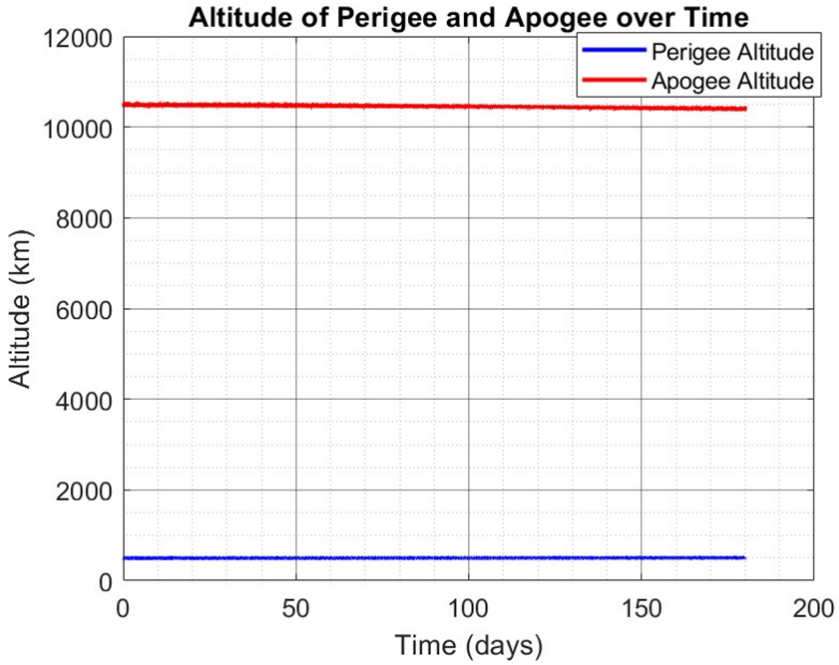

Figure 3.4: Perigee and Apogee's altitude over the mission's duration time.

of its velocity vector. The Normal (or Cross-Track) axis is perpendicular to the orbital plane, pointing in the direction of the orbital angular momentum vector.

It is noticeable that, in each direction, the major perturbation is the one due to the gravitational field. In the radial direction, the spacecraft is affected by gravitational perturbation and the solar radiation pressure. In the along-track direction, the effect of the drag is added to the perturbations. In the cross-track direction, the spacecraft is affected by the drag component due to the atmosphere rotation.

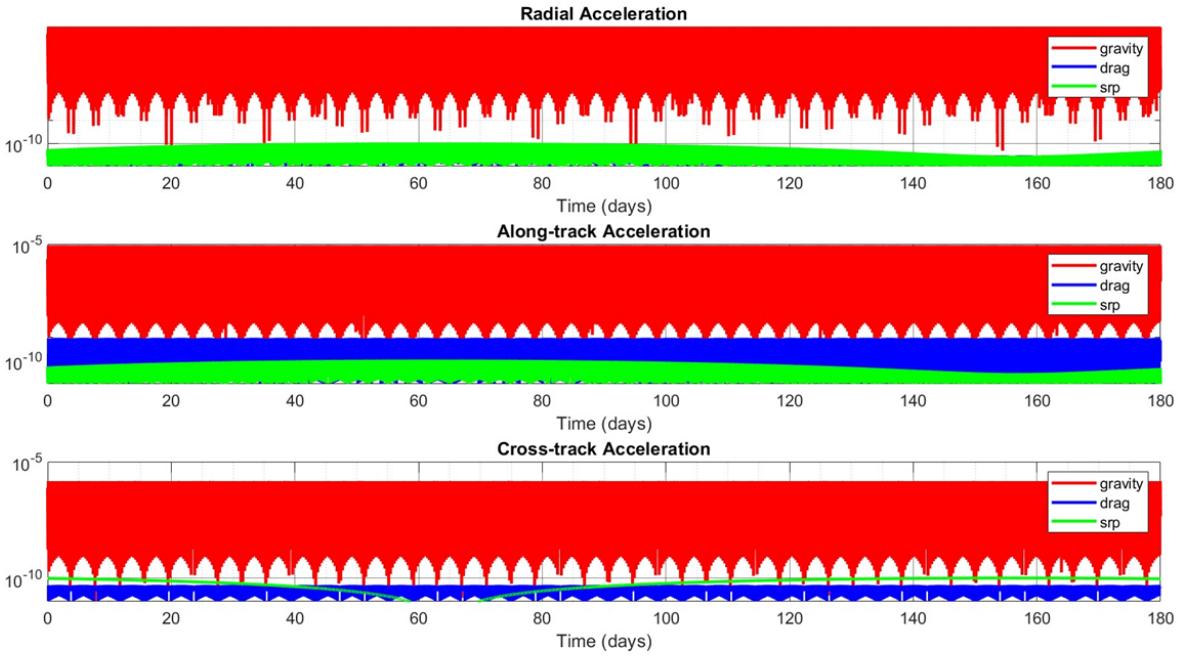

Figure 3.5: Orbital perturbations $[km/s^2]$ affecting the evolution of the formation over 6 months. The gravitational, drag and SRP perturbations are in red, blue and green respectively.

3.2 Spacecraft Formation Flying

In addition to analyzing the evolution of the perigee and apogee over time, it is also important to evaluate the variations in key classical orbital elements: semi-major axis, eccentricity and inclination. The swarm configuration comprises seven CubeSats arranged in a circular formation, with one central chief CubeSat and six deputy CubeSats arranged hexagonally around it. [24]

The Hill-Clohessy-Wiltshire model, utilized in the relative motion problem for

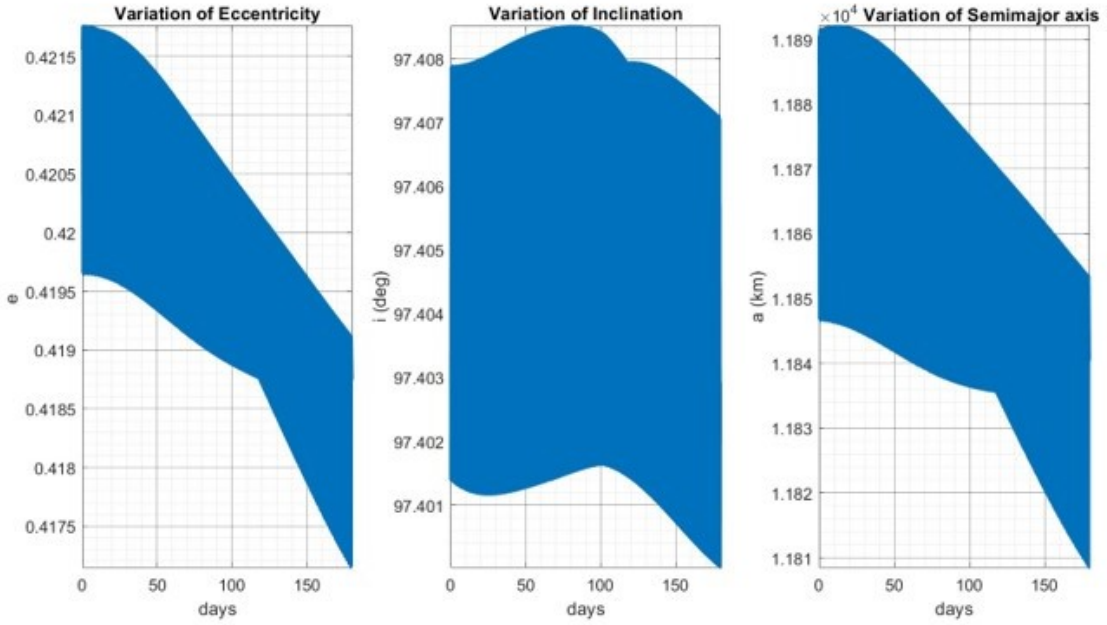

Figure 3.6: Evolution of the main Classical Orbital Elements (eccentricity, inclination and semimajor axis) over the mission's duration time.

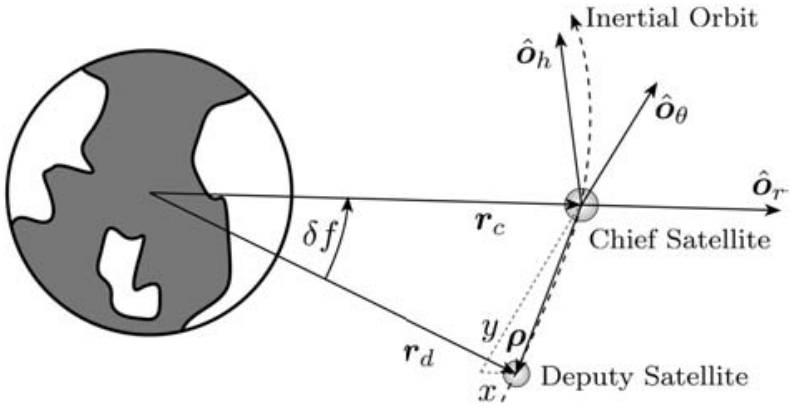

Figure 3.7: Illustration of a leader-follower type of a two-spacecraft formation. [12]

artificial satellites, is recognized for offering a valuable set of equations to address challenges related to rendezvous and formation-flying, particularly optimal control problems. [21] These equations presuppose that the chief spacecraft is in a circular orbit and that the deputy spacecraft maintains small relative distances and velocities in relation to the chief.

In Fig. 3.7, the inertial chief position is expressed through the vector $r_c(t)$, while the deputy satellite position is given by $r_d(t)$. Utilizing the Hill coordinate frame proves advantageous for depicting how the relative orbit geometry appears from the

perspective of the chief spacecraft. Its origin is at the chief satellite position and its orientation is given by the vector triad $\{\hat{O}_r, \hat{O}_\theta, \hat{O}_h\}$ shown in Fig. 3.7 and Fig.3.8. The vector $\hat{O}_r$ is in the orbit radius direction, while $\hat{O}_h$ is parallel to the orbit momentum vector in the orbit normal direction. The vector $\hat{O}_\theta$ then completes the right-hand coordinates system. [12] Mathematically, these O frame orientation vectors are expressed as

$$\hat{O}_r = \frac{\vec{r}_c}{r_c} \tag{3.5a}$$

$$\hat{O}_\theta = \hat{O}_h \times \hat{O}_r \tag{3.5b}$$

$$\hat{O}_h = \frac{\vec{h}}{h} \tag{3.5c}$$

with $\vec{h} = \vec{r}_c \times \dot{\vec{r}}_c$.

For the formation flying aspect of this mission, the model is more intricate than a simple leader-follower setup. As shown in Fig. 3.8, the spacecrafts are on slightly different orbits that satisfy specific constraints. These constraints ensure the relative orbit is bounded and prevent the spacecraft from drifting apart. In this arrangement, the chief satellite acts as the central focal point around which all deputy satellites revolve.

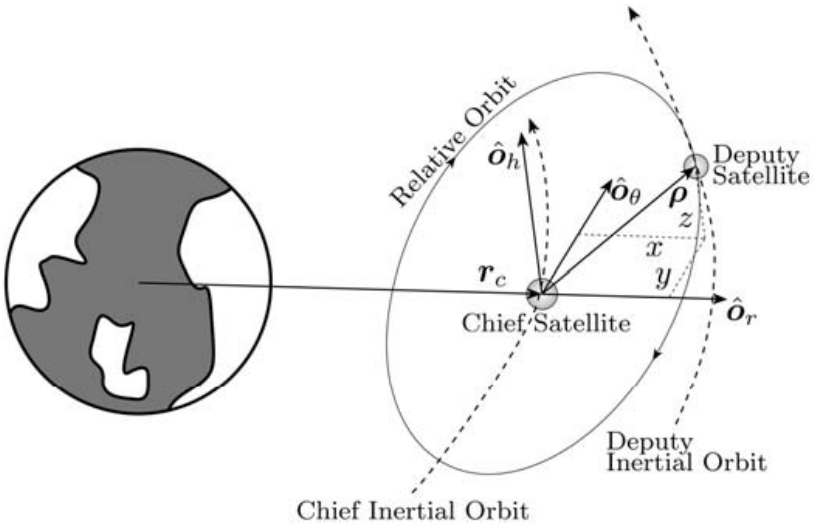

Figure 3.8: Illustration of a general type of spacecraft formation with out-of-orbit plane relative motion.[12]

3.2.1 Clohessy - Wiltshire Equations

In this subsection, the relative orbit is described using the Cartesian coordinate vector $\vec{\rho} = (x, y, z)^T$. The vector components are taken in the rotating chief Hill

frame. The benefit of employing Hill frame coordinates lies in the immediate clarity they provide regarding the physical dimensions of the relative orbit. The (x, y) coordinates define the relative orbit motion in the chief orbit plane. The z coordinate defines any motion out of the chief orbit plane. [12]

To derive the relative equations of motion using Cartesian coordinates in the rotating Hill frame, it's necessary to express the deputy satellite's position vector in the following manner:

$$\vec{r}_d = \vec{r}_c + \vec{\rho} = (r_c + x)\hat{O}_r + y\,\hat{O}_{theta} + z\,\hat{O}_h \tag{3.6}$$

where the r_c is the current orbit radius of the chief satellite. The angular velocity vector of the rotating Hill frame O relative to the inertial frame N is given by

$$\vec{\omega}_{O/N} = \dot{f}\hat{O}_h \tag{3.7}$$

with f being the chief frame true anomaly. The deputy satellite acceleration vector can be expressed using two derivatives with respect to the inertial frame:

$$\begin{aligned} \ddot{\vec{r}}_d = (\ddot{\vec{r}}_c + \ddot{\vec{x}} - 2\dot{\vec{y}}\dot{\vec{f}} - \ddot{\vec{f}}y - \dot{f}^2(r_c + x))\hat{O}_r \\ +(\ddot{\vec{y}} + 2\dot{\vec{f}}(\dot{\vec{r}}_c + \dot{\vec{x}}) + \ddot{\vec{f}}(r_c + x) - \dot{\vec{f}}^2 y)\hat{O}_\theta + \ddot{\vec{z}}\hat{O}_h \end{aligned} \tag{3.8}$$

This kinematic expression can be simplified by making use of the following identities. The chief orbit angular momentum magnitude is given by $h = r_c^2\dot{f}$. Because h is constant for Keplerian motion, taking the first time derivate of h yields

$$\dot{\vec{h}} = 0 = 2r_c\dot{\vec{r}}_c\dot{\vec{f}} + r_c^2\ddot{\vec{f}} \tag{3.9}$$

This orbit element constraint can be used to solve for the true anomaly acceleration:

$$\ddot{\vec{f}} = -2\frac{\dot{\vec{r}}_c}{r_c}\dot{\vec{f}} \tag{3.10}$$

Further, the chief satellite position can be written as $\vec{r}_c = r_c\hat{O}_r$. Taking two time derivatives with respect to the inertial frame and using the orbit equations of motion, the chief acceleration vector is expressed as

$$\ddot{\vec{r}}_c = (\ddot{\vec{r}}_c - r_c\dot{\vec{f}}^2)\hat{O}_r = -\frac{\mu}{r_c^3}\vec{r}_c = -\frac{\mu}{r_c^2}\hat{O}_r \tag{3.11}$$

Equating vector components in Eq.3.11, the chief orbit radius acceleration is expressed as:

$$\ddot{\vec{r}}_c = r_c\dot{\vec{f}}^2 - \frac{\mu}{r_c^2} = r_c\dot{\vec{f}}^2\left(1 - \frac{r_c}{p}\right) \tag{3.12}$$

Substituting Eqs. 3.10 and 3.12 into Eq. 3.18, the deputy acceleration vector expression is reduced to

$$\begin{aligned}\ddot{\vec{r}}_d = &\left(\ddot{\vec{x}} - 2\dot{\vec{f}}\left(\dot{\vec{y}} - y\frac{\dot{\vec{r}}_c}{r_c}\right) - x\dot{\vec{f}}^2 - \frac{\mu}{r_c^2}\right)\hat{O}_r \\ &+ \left(\ddot{\vec{y}} + 2\dot{\vec{f}}\left(\dot{\vec{x}} - x\frac{\dot{\vec{r}}_c}{r_c}\right) - y\dot{\vec{f}}^2\right)\hat{O}_\theta + \ddot{\vec{z}}\hat{O}_h\end{aligned} \tag{3.13}$$

Next, we substitute the kinematic acceleration expression in Eq. 3.13 into the orbit equations of motion. The deputy satellite orbital equations of motion are given by

$$\ddot{\vec{r}}_d = -\frac{\mu}{r_d^3}\vec{r_d} = -\frac{\mu}{r_d^3}\begin{pmatrix} r_c + x \\ y \\ z \end{pmatrix}_O \tag{3.14}$$

with $r_d = \sqrt{(r_c + x)^2 + y^2 + z^2}$. Equating Eqs. 3.13 and 3.14 , the exact nonlinear relative equations of motion are given by

$$\ddot{\vec{x}} - 2\dot{\vec{f}}\left(\dot{\vec{y}} - y\frac{\dot{\vec{r}}_c}{r_c}\right) - x\dot{\vec{f}}^2 - \frac{\mu}{r_c^2} = -\frac{\mu}{r_d^3}(r_c + x) \tag{3.15a}$$

$$\ddot{\vec{y}} + 2\dot{\vec{f}}\left(\dot{\vec{x}} - x\frac{\dot{\vec{r}}_c}{r_c}\right) - y\dot{\vec{f}}^2 = -\frac{\mu}{r_d^3}y \tag{3.15b}$$

$$\ddot{\vec{z}} = -\frac{\mu}{r_d^3}z \tag{3.15c}$$

The only assumption made is that no disturbances affect the satellite, hence the validity of the Keplerian motion assumption in the orbital equations of motion (Eq. 3.14). The relative equations of motion (Eq. 3.15) hold true for arbitrarily large relative orbits, even if the chief orbit is eccentric. Should the relative orbit coordinates (x, y, z) be significantly smaller than the chief orbit radius r_c, further simplification of Eq. 3.15 is possible. [12] The deputy orbit radius r_d is approximated as

$$r_d = r_c\sqrt{1 + 2\frac{x}{r_c} + \frac{x^2 + y^2 + z^2}{r_c^2}} \approx r_c\sqrt{1 + 2\frac{x}{r_c}} \tag{3.16}$$

This allows us to write

$$\frac{\mu}{r_d^3} \approx \frac{\mu}{r_c^3}\left(1 - 3\frac{x}{r_c}\right) \tag{3.17}$$

The term μ/r_c^3 can also be written in the following useful forms:

$$\frac{\mu}{r_c^3} = \frac{r_c}{p}\dot{\vec{f}}^2 = \frac{\dot{\vec{f}}^2}{1 + e\ cosf} \tag{3.18}$$

Note that the orbit elements shown in Eq.3.18 are chief orbit elements. Neglecting higher order terms, we are able to simplify the right-hand side of Eq.3.14 to

$$-\frac{\mu}{r_d^3}\begin{pmatrix} r_c + x \\ y \\ z \end{pmatrix}_O \approx -\frac{\mu}{r_c^3}\left(1 - 3\frac{x}{r_c}\right)\begin{pmatrix} r_c + x \\ y \\ z \end{pmatrix}_O \approx -\frac{\mu}{r_c^3}\begin{pmatrix} r_c - 2x \\ y \\ z \end{pmatrix}_O \tag{3.19}$$

By substituting Eq. 3.19 into Eq. 3.15 and subsequently simplifying, we obtain the relative orbit equations of motion, under the assumption that x, y, and z are negligible compared to the chief orbit radius r_c: [12]

$$\ddot{\vec{x}} - x\dot{\vec{f}}^2\left(1 + 2\frac{r_c}{p}\right) - 2\dot{\vec{f}}\left(\dot{\vec{y}} - y\frac{\dot{\vec{r_c}}}{r_c}\right) = 0 \tag{3.20a}$$

$$\ddot{\vec{y}} - 2\dot{\vec{f}}\left(\dot{\vec{x}} - x\frac{\dot{\vec{r_c}}}{r_c}\right) - y\dot{\vec{f}}^2\left(1 - \frac{r_c}{p}\right) = 0 \tag{3.20b}$$

$$\ddot{\vec{z}} + \frac{r_c}{p}\dot{\vec{f}}^2 z = 0 \tag{3.20c}$$

Using Eqs. 3.20 and 3.18, along with the true latitude $\theta = \omega + f$, the general relative equations of motion are rewritten in the common form [22]:

$$\ddot{\vec{x}} - x\left(\dot{\vec{\theta}}^2 + 2\frac{\mu}{r_c^3}\right) - y\ddot{\vec{\theta}} - 2\dot{\vec{y}}\dot{\vec{\theta}} = 0 \tag{3.21a}$$

$$\ddot{\vec{y}} + x\ddot{\vec{\theta}} + 2\dot{\vec{x}}\dot{\vec{\theta}} - y\left(\dot{\vec{\theta}}^2 - \frac{\mu}{r_c^3}\right) = 0 \tag{3.21b}$$

$$\ddot{\vec{z}} + \frac{\mu}{r_c^3}z = 0 \tag{3.21c}$$

If the chief satellite orbit is assumed to be circular, then $e = 0$, $p = r_c$, and the chief orbit radius r_c is constant. Because for a circular orbit the mean orbital rate n is equal to the true anomaly rate $\dot{\vec{f}}$, the relative equations of motion reduce to the simple form known as the *Clohessy-Wiltshire (CW) equations* [13] [31]:

$$\ddot{\vec{x}} - 2n\dot{\vec{y}} - 3n^2x = 0 \tag{3.22a}$$

$$\ddot{\vec{y}} + 2n\dot{\vec{x}} = 0 \tag{3.22b}$$

$$\ddot{\vec{z}} + n^2 z = 0 \tag{3.22c}$$

It's important to note that these equations of motion hold true only under the conditions where the chief orbit is circular and the relative orbit coordinates (x, y, z) are significantly smaller than the chief orbit radius r_c. The simplified form of the differential equations in Eq. 3.22 facilitates analytical integration, enabling closed-form solutions to the relative equations of motion. For instance, the differential equations governing the out-of-plane motion of the relative orbit, as depicted in Eq. 3.20, resemble those of a simple spring-mass system, for which a known solution exists.[12]

3.2.2 Orbit Element Difference Description

While employing Hill frame coordinates (x, y, z) is a widely adopted approach to describe a relative orbit, it bears the notable drawback that, for a non-circular orbit, solving their differential equations is necessary to determine the exact relative orbit geometry. [12] The relative orbit is determined through the chief orbit motion and the relative orbit initial conditions:

$$X = (x_0, y_0, z_0, \dot{\vec{x}}_0, \dot{\vec{y}}_0, \dot{\vec{z}}_0,)^T \tag{3.23}$$

To predict the position of a deputy satellite at a given time t, the corresponding differential equations in either Eq. 3.20 or Eq. 3.22 must be integrated forward to time t. Consequently, the six initial conditions outlined in Eq. 3.23 serve as six invariant quantities governing the motion of the relative orbit. However, they are not conducive to determining the instantaneous geometry of the relative orbit motion. Nevertheless, if the chief orbit is circular and the relative motion is linearized, then the CW equations possess an analytical solution. This holds true only under the conditions where the relative orbit dimension is negligible compared to the chief orbit radius (validating the linearization assumption), and if the chief orbit is circular. [12]

However, the Keplerian motion of a satellite can also be defined through six orbit elements:

$$(a, e, i, \Omega, \omega, \nu_0)^T \tag{3.24}$$

where a is the semi-major axis, e is the eccentricity, i is the orbit inclination angle, Ω is the longitude of the ascending node, ω is the argument of the pericenter, and ν is the true anomaly. Nevertheless when describing a relative orbit by differences in orbital elements, expressing the anomaly difference using $\delta\nu$ can be inconvenient. To overcome this, the desired anomaly difference between two orbits is often represented as the mean anomaly difference δM.[12]

Rather than resolving a differential equation for determining the present satellite states, one must resort to numerically solving Kepler's equation to establish the

current mean anomaly angle. Consequently, only one state M essentially requires resolution to determine the satellite position. This stands in contrast to the utilization of the X state vector, where all six states function as fast variables, exhibiting variability throughout the orbit. Hence, employing orbital elements simplifies both the orbit depiction and the computation of satellite position.[12] Therefore, from now on, the relative orbit will be define in terms of the orbit element difference vector:

$$(a_d - a_c, e_d - e_c, i_d - i_c, \Omega_d - \Omega_c, \omega_d - \omega_c, M_{0d} - M_{0c})^T = (\delta a, \delta e, \delta i, \delta\Omega, \delta\omega, \delta\nu_0)^T \tag{3.25}$$

where $\cdot_d$ is referred to the deputy satellite orbit vector, and $\cdot_c$ is referred to the chief orbit element vector. Utilizing the orbit element difference vector and the chief orbit element vector, the deputy satellite's position can be determined at any given time by resolving Kepler's equation. It's worth mentioning that the relative orbit description in Eq.3.25 imposes no assumptions regarding the relative orbit's size in comparison to the chief orbit radius, nor does it mandate that the chief orbit be circular.[12]

Describing the relative orbit in terms of differences in orbit elements enables us to draw specific conclusions regarding the geometry of the relative orbit. This concept is illustrated in Fig. 3.9. Both the inclination angle and the differences in the ascending node will influence the extent of the out-of-plane motion of the relative orbit. The inclination angle difference δi indicates the amount of out-of-plane motion that the relative orbit will exhibit as the satellite traverses the northern or southernmost regions. The ascending node difference reveals the expected out-of-plane motion as the satellite crosses the equator. For instance, if the computed orbit element differences for a given relative orbit yield δi as zero, it can be deduced immediately that the relative orbit will feature zero out-of-plane motion as the chief satellite passes the outer latitude extremes.[12]

3.2.3 Linearized Relative Orbit Motion for General Elliptic Orbit

The local Cartesian Hill frame coordinates x, y, and z are expressed in terms of the orbit element differences as

$$x = \delta r \tag{3.26a}$$

$$y = r(\delta\theta + cos\, i\ \delta\Omega) \tag{3.26b}$$

$$z = r(sin\,\theta\ \delta i - cos\,\theta\, sin\, i\ \delta\Omega) \tag{3.26c}$$

These equations establish a straightforward linear relationship between differences in orbit elements and the Cartesian coordinate vector $\vec{\rho}$ in the Hill frame.

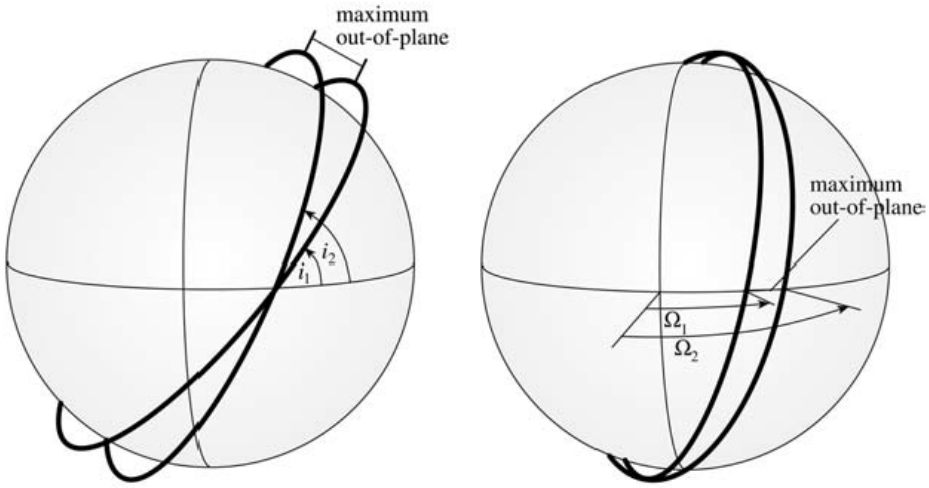

Figure 3.9: Relative orbit effect of having specific orbit element differences. [12]

The sole linearizing assumption made is that the relative orbit radius ρ is significantly smaller than the inertial chief orbit radius r. However, since this relationship must remain valid at all times, these linearized equations also serve as an approximation for the relative orbit motion $\vec{\rho}$ in terms of the true anomaly angle f. To correlate time with the true anomaly, Kepler's equations must be resolved. Yet, for delineating the relative orbit geometry using Hill frame Cartesian coordinates, a solution in terms of the true anomaly f is favored. This preference arises from the fact that by traversing f over a full revolution, the (x, y, z) coordinates derived from these equations will produce the linearized approximation of the relative orbit, dictated by a predetermined set of constant orbit element differences. It's important to highlight that no differential equations are employed in determining the motion of the relative orbit here. Additionally, the primary relative orbit radial (x direction), along-track (y direction), and out-of-plane (z direction) motions can be easily identified. [12]

When describing a relative orbit through orbit element differences, it is not convenient to describe the anomaly difference through $\delta\theta$ or δf. In elliptical chief orbits, the difference in true anomaly between two orbits fluctuates over the course of the orbit. To circumvent this variability, the desired anomaly difference between two orbits is usually stated in terms of a mean anomaly difference δM.[12]

To express the mean anomaly differences in terms of other anomaly differences, we make use of the mean anomaly definition

$$M = E - e\,sinE \tag{3.27}$$

and take its first variation to yield

$$\delta M = \frac{\delta M}{\delta E}\delta E + \frac{\delta M}{\delta e}\delta e = (1 - e\,cosE)\delta E + sinE\,\delta e \tag{3.28}$$

Using the mapping between eccentric anomaly E and true anomaly f

$$tan\frac{f}{2} = \sqrt{\frac{1+e}{1-e}}tan\frac{E}{2} \tag{3.29}$$

and taking its first variation, differences in E are then expressed as differences in f and e through

$$\delta E = \frac{\eta}{1 + e\,cosf}\delta f - \frac{sin\,f}{1 + e\,cosf}\,\frac{\delta e}{\eta} \tag{3.30}$$

with $\eta = \sqrt{1 - e^2}$. Substituting Eq. 3.30 into Eq. 3.28 and solving for δM using the orbit identities yields

$$\delta M = \frac{\eta}{(1 + e\,cosf)^2}(\eta^2\delta f - sin\,f(2 + e\,cosf)\delta e) \tag{3.31}$$

Now, using Eq. 3.31, differences in true anomaly are written in terms of differences in mean anomaly and differences in eccentricity

$$\delta f = \frac{(1 + e\,cosf)^2}{\eta^3}\delta M + \frac{sinf}{\eta^2}(2 + e\,cosf)\delta e \tag{3.32}$$

Let's define the orbit element difference vector $\delta\vec{e}$ to consist of

$$\delta\vec{e} = (\delta a, \delta e, \delta i, \delta\Omega, \delta\omega, \delta M)^T \tag{3.33}$$

It's worth noting that all these differences in orbit elements remain constant for Keplerian two-body motion. Moreover, in the subsequent discussion on relative orbit geometry, no singularities will arise; however, they may occur in the case of near-circular orbits.[12]

At this point, it is possible to substitute Eq. 3.32 into the linear mapping provided in Eq. 3.26 and simplify the result, we are now able to express the relative position coordinates (x, y, z) in terms of the orbit element differences in Eq. 3.33 through

$$x(f) \approx \frac{r}{a}\delta a + \frac{ae\,sinf}{\eta}\delta M - a\,cosf\delta e \tag{3.34a}$$

$$y(f) \approx \frac{r}{\eta^3}(1 + e\,cosf)^2\delta M + r\delta\omega + \frac{r\,sinf}{\eta^2}(2 + e\,cosf)\delta\,e + r\,cosi\,\delta\Omega \tag{3.34b}$$

$$z(f) \approx r(sin\theta\,\delta i - cos\theta\,sin\,i\,\delta\Omega) \tag{3.34c}$$

It's important to recognize that in this linearized mapping, the difference in the argument of perigee $\delta\omega$ does not manifest in the expression for $x(f)$. Additionally, these equations remain valid for both circular and elliptic orbits. Only the δM and δe terms introduce periodic elements to the radial x solution. Due to the dependency of r on the true anomaly f, all differences in orbit elements contribute both static offsets and periodic elements to the along-track y motion. In the case of the out-of-plane z motion, both the δi and $\delta\Omega$ terms govern the oscillations.[12]

To minimize the relative drift effect, all satellites must experience the same rates of change in Ω and ω. Consequently, the differences in inclination, semimajor axis, and eccentricity must be null: $\delta i, \delta a, \delta e = 0$. Under these conditions, and assuming a close formation with relative distances ranging from a few meters to a few tens of meters, the linear relative motion equations (Eq. 3.34) can be simplified as: [30]

$$x = \frac{a\ e\ sin(\nu+\omega)\delta M}{\eta} \tag{3.35a}$$

$$y = \frac{r(1+e\ cos\,\nu)^2\delta M}{\eta^3} + r\delta\omega + r\ cos\,i\ \delta\Omega \tag{3.35b}$$

$$z = -r\ cos(\nu+\omega)\ sin\,i\ \delta\Omega \tag{3.35c}$$

where $r = \frac{a(a-e^2)}{1+e\,cos\,\nu}$ and $\eta = \sqrt{1-e^2}$.

In this analysis, it has been considered and studied a formation in the cross-track direction, with near-polar inclination. So, the initial position of each CubeSat, of the six around the central one, within the RTN frame are given by

$$x = 0 \tag{3.36a}$$

$$y = r\ sin\theta \tag{3.36b}$$

$$z = r\ cos\theta \tag{3.36c}$$

where x_0, y_0, z_0 are the initial positions of the central satellite, r is the formation radius and θ is the phase of the i-th satellite on the circular formation. The values of θ are $60°, 120°, 180°, 240°, 300°, 360°$. So, the first step is to evaluate the position of the satellites through Eqs. 3.36. Then, it is possible to substitute the results into the Eqs. 3.35. As already said before, every CubeSat, both the chief and the deputies, has identical semimajor axes, eccentricities and inclinations. Furthermore, being the formation in cross-track direction, the δM that governs the radial variations is 0. It is clear that the resulting simplification leads to

$$\delta M = 0 \tag{3.37a}$$

$$\delta\omega = \frac{\delta y}{r} - cos\,i\delta\Omega \tag{3.37b}$$

$$\delta\Omega = -\frac{\delta z}{r\ cos(\theta+\omega)sin\,i} \tag{3.37c}$$

3.3 Analysis

In this chapter, we delve into the stability analysis of formation flying in Heliotropic orbits, building on the dynamic model established in the previous chapter. By applying this model, we aim to understand the evolution of the distances between spacecraft throughout the mission. Our focus is on identifying the factors that influence formation stability.

To evaluate the stability of the CubeSats' formation flying in the selected Heliotropic orbit, some graphs are displayed. The classical orbital elements of the chief CubeSat are visualized in Tab. 3.3.

Perigee Radius	r_p	6 878 km
Apogee radius	r_a	16 903,20 km
Semimajor axis	a	11 890,6 km
Inclination	i	97,4014°
RAAN	Ω	0°
omega	ω	90°
True anomaly	θ	90°

Table 3.3: Classical orbital elements of the chief spacecraft in the formation geometry.

Starting from the position of the chief CubeSat, the position of the six deputies satellites around it are calculated using the Eqs. 3.36 and 3.37. The orbit element difference vector is displayed in Tab. 3.4, as explained in the previous chapter the value of a, i, e, M are the same as the chief satellite's. The formation is represented in a Geocentric Equatorial frame, it has a radius of $100\,m$ as shown in Fig.3.10.

Satellite Index	$\delta\omega$	$\delta\Omega$
1	$0.9522 \cdot 10^{-5}$	$0.0516 \cdot 10^{-4}$
2	$0.8193 \cdot 10^{-5}$	$-0.0516 \cdot 10^{-4}$
3	$-0.1329 \cdot 10^{-5}$	$-0.1031 \cdot 10^{-4}$
4	$-0.9522 \cdot 10^{-5}$	$-0.0516 \cdot 10^{-4}$
5	$-0.8193 \cdot 10^{-5}$	$0.0516 \cdot 10^{-4}$
6	$0.1329 \cdot 10^{-5}$	$0.1031 \cdot 10^{-4}$

Table 3.4: Relative orbits of the six deputies CubeSats defined by the orbit element difference vector, with $\delta M = 0$, $\delta a = 0$, $\delta e = 0$ and $\delta i = 0$.

To evaluate the stability of the formation, it is necessary to define the relative distance variation of each deputy CubeSat with respect to the chief CubeSat as [24]

$$RDV = \frac{d(t) - d(0)}{d(0)} \times 100 \tag{3.38}$$

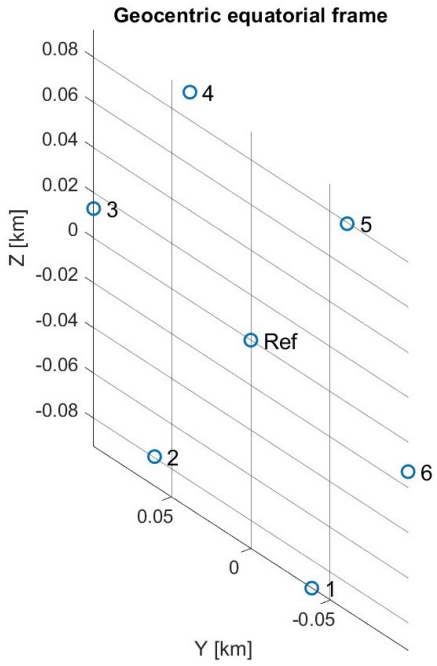

Figure 3.10: Formation geometry represented in the Geocentric Equatorial Frame.

where $d = |r_D - r_C|$, r_D and r_C are the norm of the deputy and the chief CubeSats. The RDV interval between $[-100\%, 100\%]$ is subdivided in three regions: $|RDV_{max}| < 10\%$ in green; $10\% < |RDV_{max}| < 50\%$ in yellow; $|RDV_{max}| > 50\%$ in red. For assumption, in this analysis two scenarios will be considered: the collision case considers the eventuality in which one of the deputy CubeSat is too close (-75% RDV) to the chief CubeSat; the divergence case considered the eventuality in which one of the deputy CubeSat is too far ($+50\%$ RDV) from the chief CubeSat.

Fig.3.11 shows the Relative Distance Variation evolution of the selected Heliotropic orbit. It is observable that within a few days the formation diverges up to -100%.

Furthermore, it is possible to observe the instability of the formation from Fig. 3.12, that shows the evolution of the drifts of semi-major axis, eccentricity and inclination. Indeed, the semi-major axis' drift is up to $0.025\,km$, which is not acceptable for a formation of $100\,m$ radius. These results indicate that the formation in the selected orbits will collide within a few hours if not controlled with propulsion.

It is useful to have an idea of the magnitude of the differential perturbations that act upon the CubeSats. In Fig. 3.13 are displayed the maximum differential drag and the maximum differential solar radiation pressure for each CubeSat.

It is possible to compare the previous results with the analysis conducted on

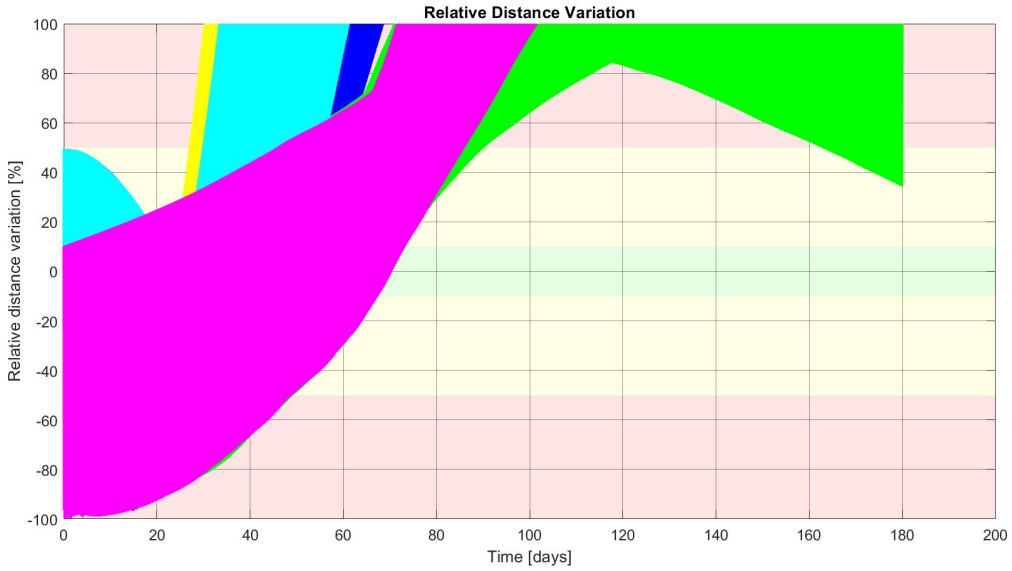

Figure 3.11: Relative distance variation evolution for the spacecraft formation in 500 km heliotropic orbit. Each color represents a CubeSat.

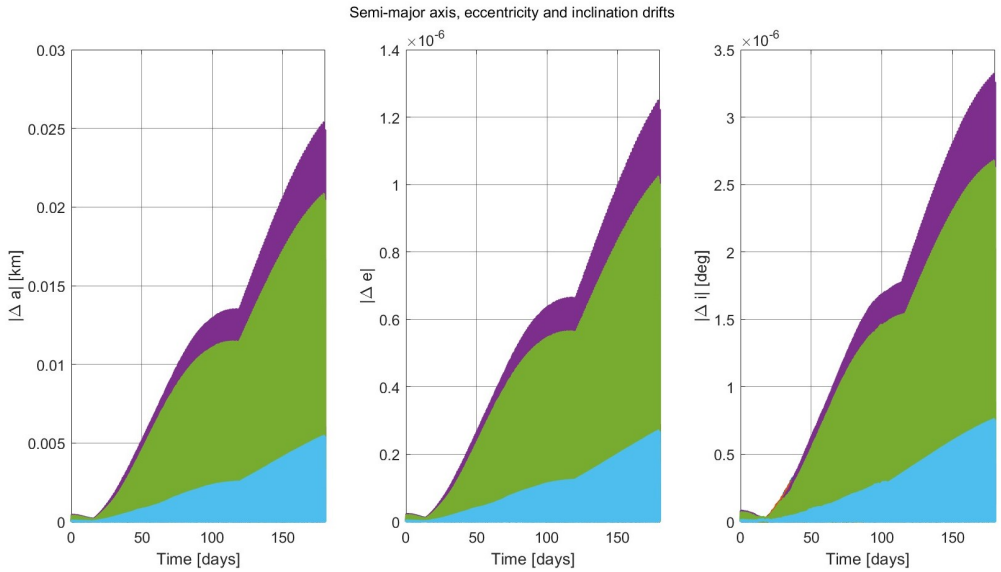

Figure 3.12: Semi-major axis, Eccentricity and Inclination drifts

a circular Sun Synchronous orbit. This type of orbit is a near-polar orbit, with same inclination of the case previously analyzed of Heliotropic orbit, and with an altitude of 500 km and the same formation's radius 100 m. As shown in Fig.3.14, the Sun-Synchronous orbit results to be a more stable solution than the Heliotropic one. Indeed, for the initial 20 days, the formation remains stable without encounter

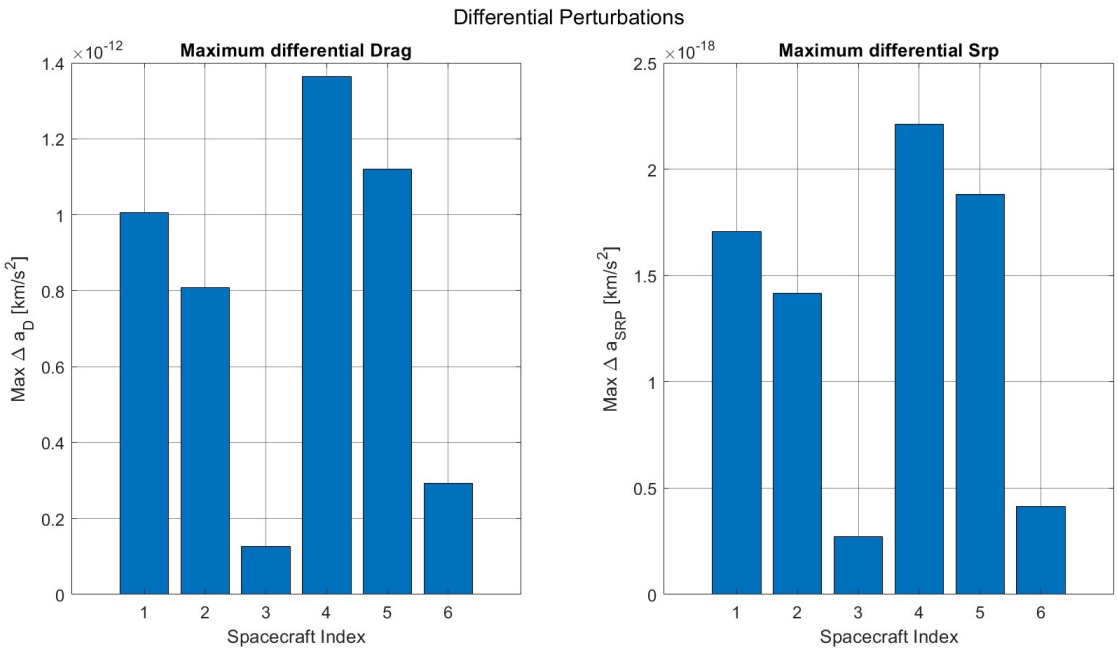

Figure 3.13: Differential Perturbations, maximum differential drag and maximum differential solar radiation pressure

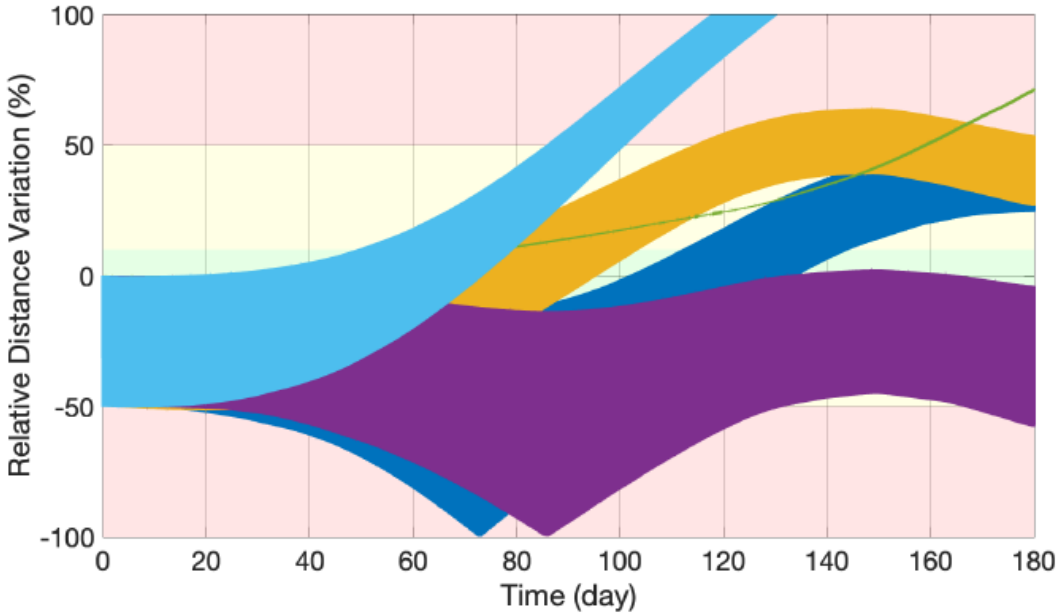

Figure 3.14: Relative distance variation evolution for the spacecraft formation in 500 km sun-synchronous orbit. Each color represents a CubeSat.

neither case of collision or divergence. Furthermore, the semi-major axis drift in

the case of Sun-Synchronous orbit is up to 0.01 km, which is an acceptable value for the studied formation. In this analysis, it is assumed that the attitude is perfectly known, implying an offset of zero.

3.3.1 Influence of ω on the Formation's Stability

As explained in Chapter 3.1, both Heliotropic and Anti-Heliotropic orbits exist. The heliotropic orbits typically have their periapsis positioned on the opposite side of the Sun from the body. Conversely, Anti-Heliotropic orbits have their periapsis directed toward the Sun. Therefore, it is useful to examine the stability for different orientations toward the Sun, which means running the analysis with different values of ω and Ω. By doing this, we want to investigate the cause of the instability of the formation.

Perigee Radius	r_p	6 878 km
Apogee radius	r_a	16 903,20 km
Semimajor axis	a	11 890,6 km
Inclination	i	97,4014°
RAAN	Ω	0°
omega	ω	18° - 45° - 90° - 135° - 162° - 225° - 270° - 315°
True anomaly	θ	90°

Table 3.5: Classical orbital elements of the chief spacecraft in the formation geometry

As done in Chapter 3.3, the position of the formation has been evaluate starting from the chief satellite's position (Tab. 3.5).

Analysis with $\omega = 18°$ and $\Omega = 0°$

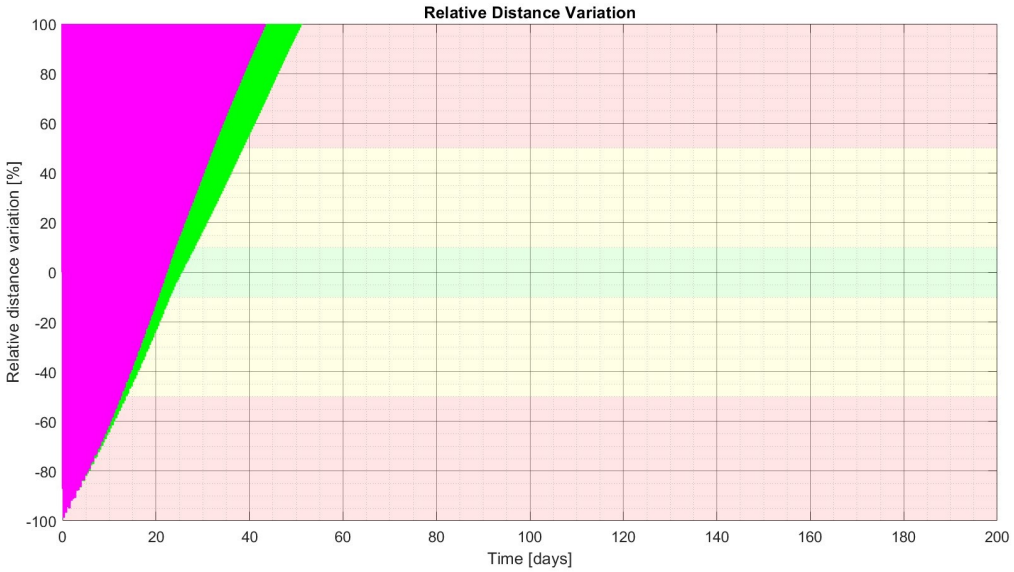

Figure 3.15: Relative distance variation evolution for the spacecraft formation in 500 km heliotropic orbit $\omega = 18°$. Each color represents a CubeSat.

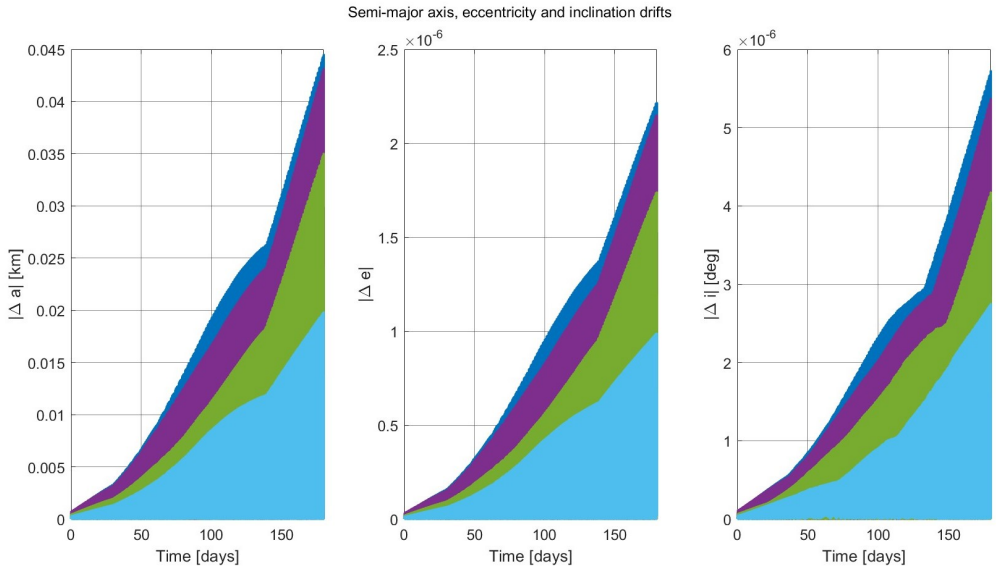

Figure 3.16: Semi-major axis, Eccentricity and Inclination drifts, $\omega = 18°$.

Analysis with $\omega = 45°$ and $\Omega = 0°$

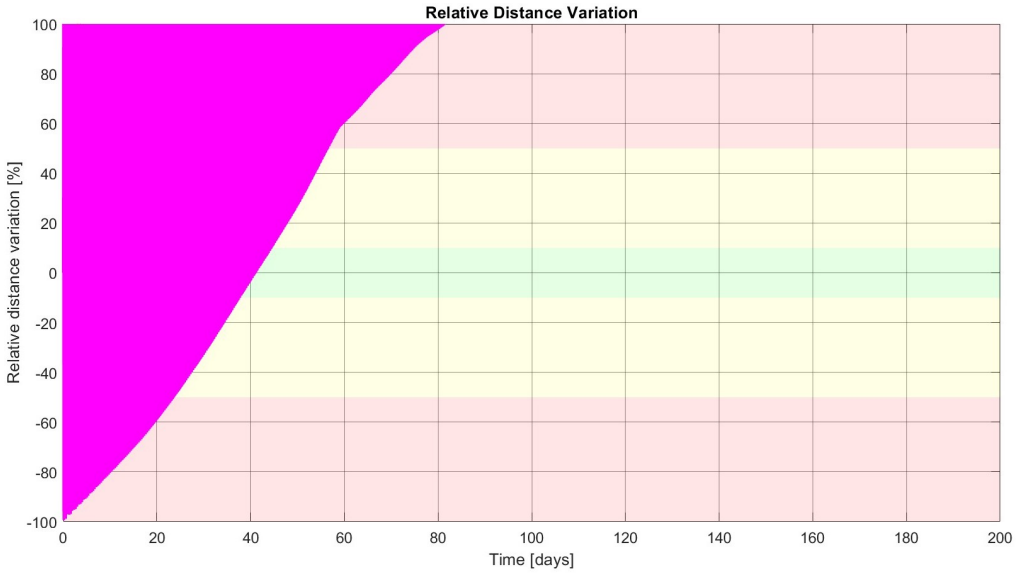

Figure 3.17: Relative distance variation evolution for the spacecraft formation in 500 km heliotropic orbit $\omega = 45°$. Each color represents a CubeSat.

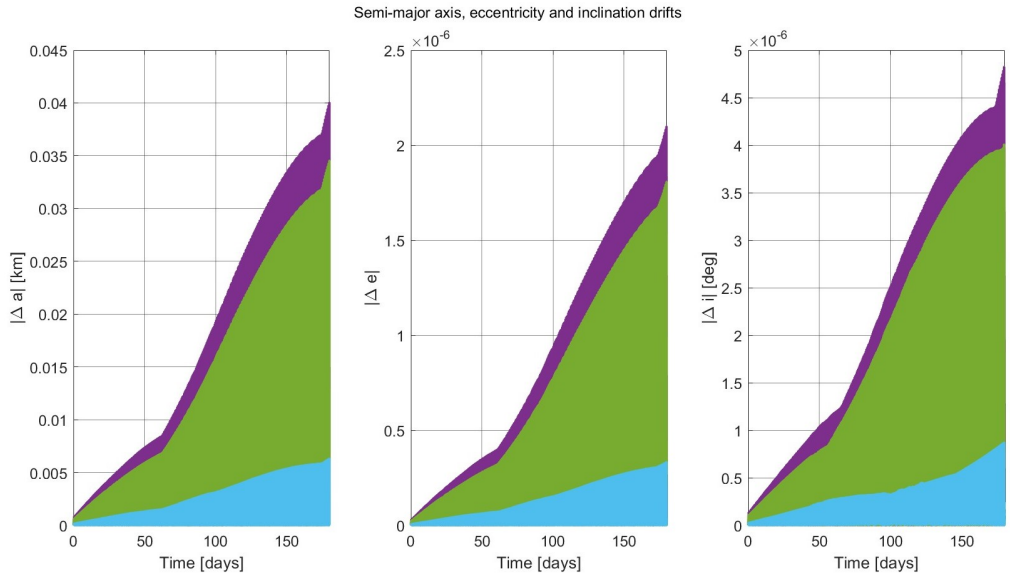

Figure 3.18: Semi-major axis, Eccentricity and Inclination drifts, $\omega = 45°$.

Analysis with $\omega = 135°$ and $\Omega = 0°$

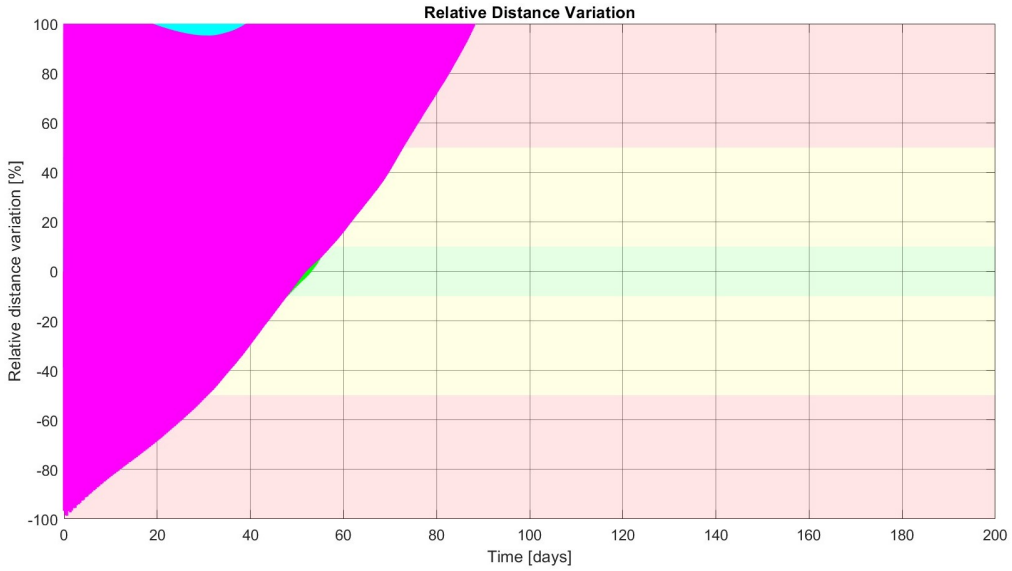

Figure 3.19: Relative distance variation evolution for the spacecraft formation in 500 km heliotropic orbit $\omega = 135°$. Each color represents a CubeSat.

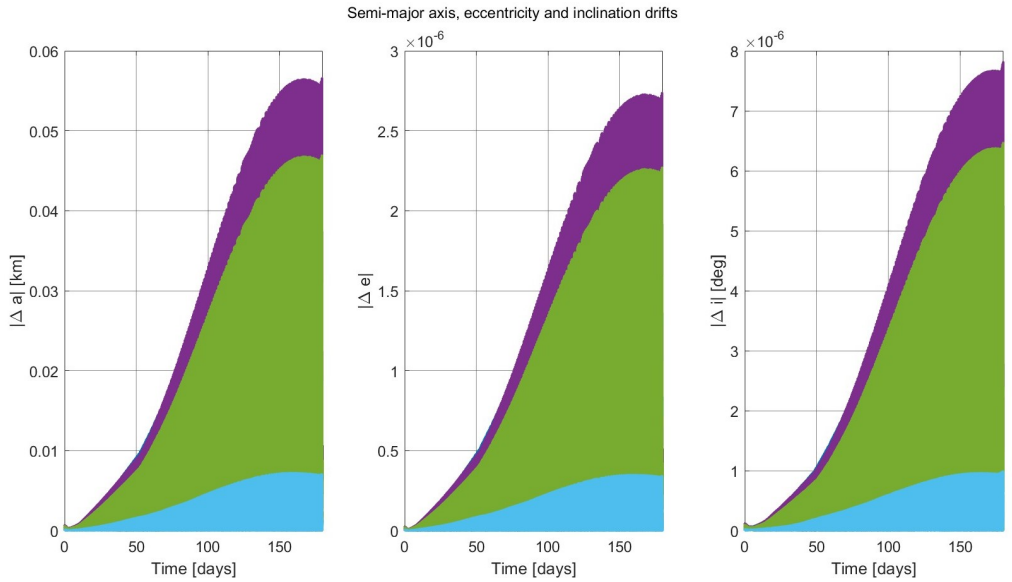

Figure 3.20: Semi-major axis, Eccentricity and Inclination drifts, $\omega = 135°$.

Analysis with $\omega = 162°$ and $\Omega = 0°$

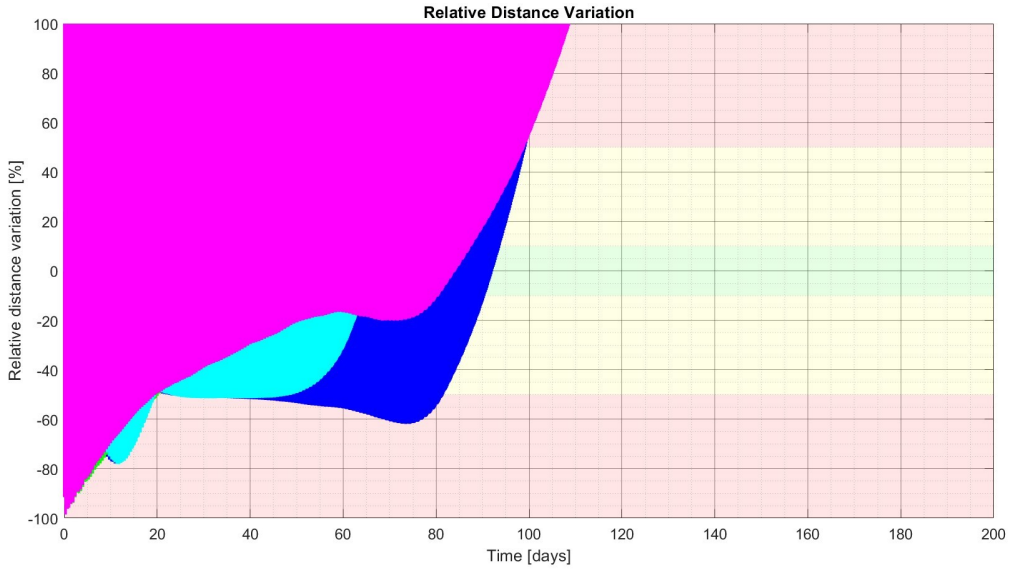

Figure 3.21: Relative distance variation evolution for the spacecraft formation in 500 km heliotropic orbit $\omega = 162°$. Each color represents a CubeSat.

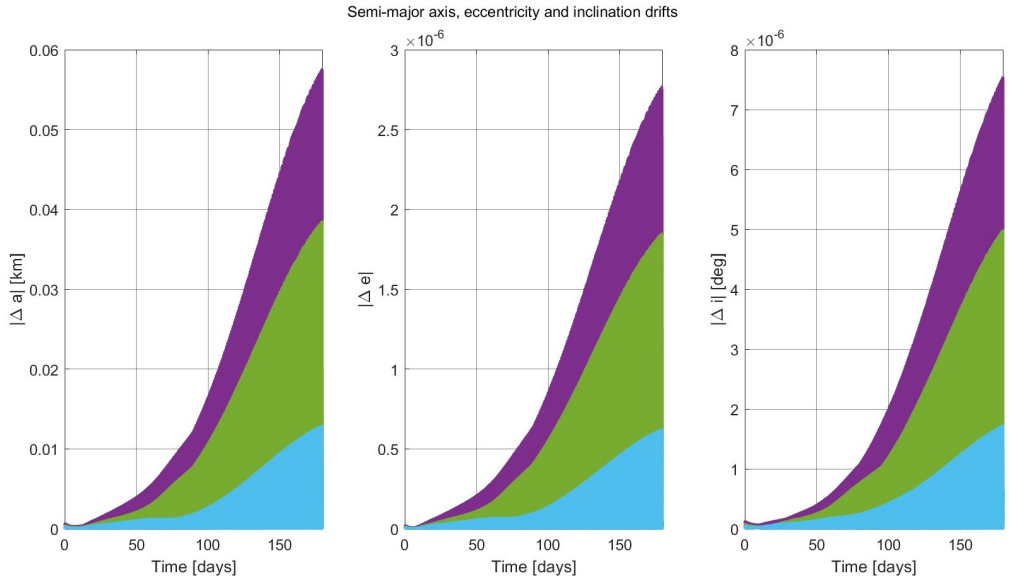

Figure 3.22: Semi-major axis, Eccentricity and Inclination drifts, $\omega = 162°$.

Analysis with $\omega = 225°$ and $\Omega = 0°$

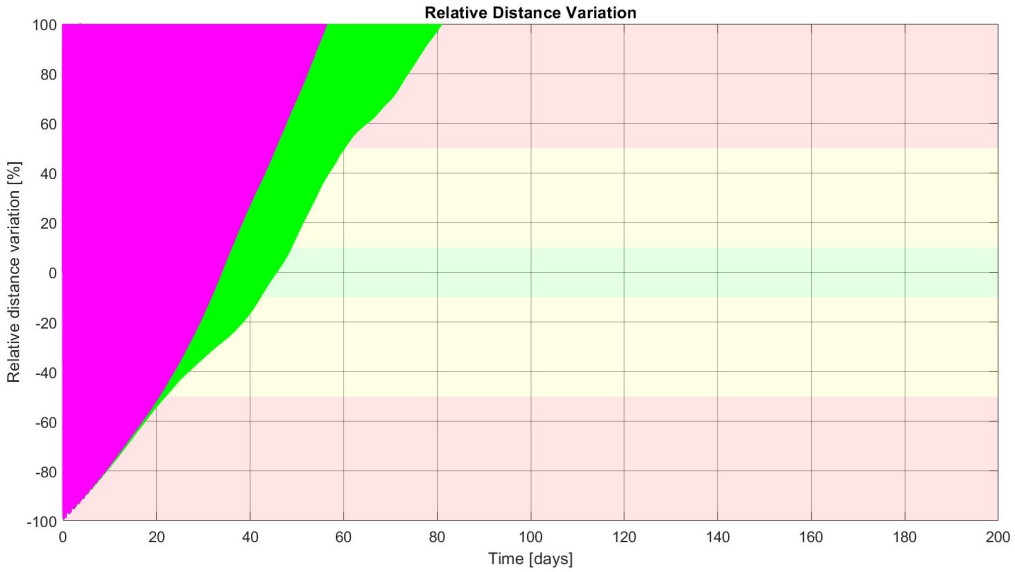

Figure 3.23: Relative distance variation evolution for the spacecraft formation in 500 km heliotropic orbit $\omega = 225°$. Each color represents a CubeSat.

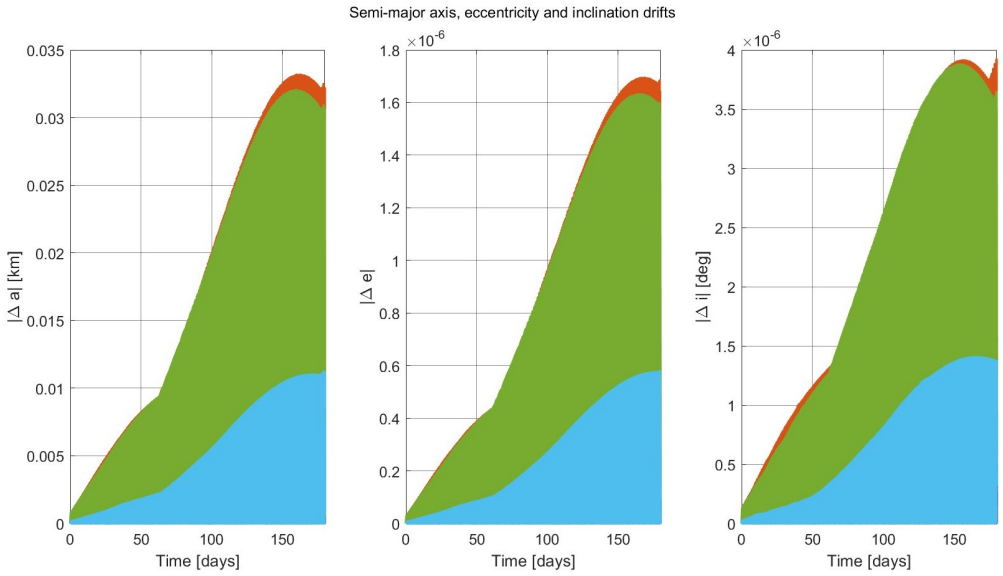

Figure 3.24: Semi-major axis, Eccentricity and Inclination drifts, $\omega = 225°$.

Analysis with $\omega = 270°$ and $\Omega = 0°$

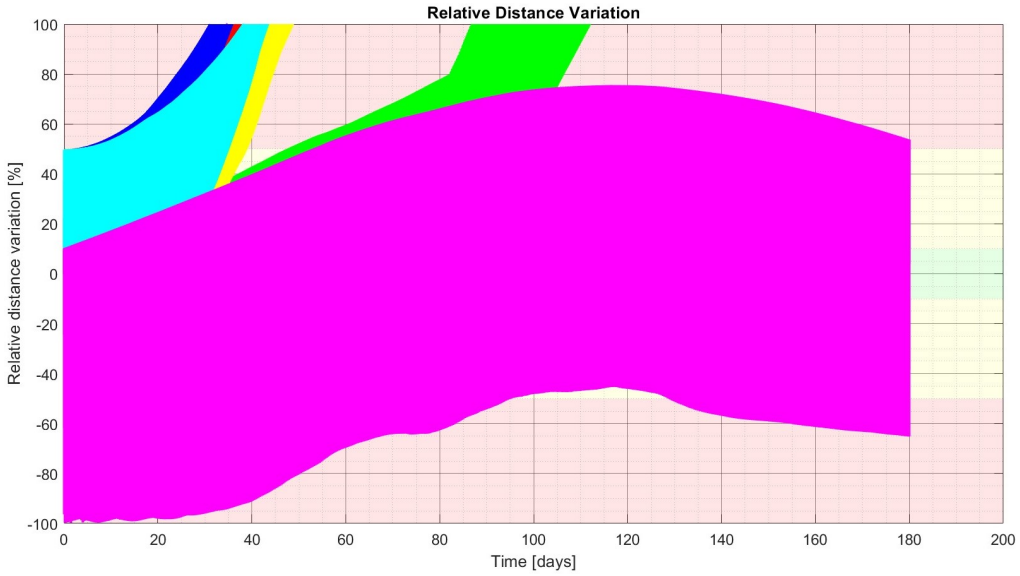

Figure 3.25: Relative distance variation evolution for the spacecraft formation in 500 km heliotropic orbit $\omega = 270°$. Each color represents a CubeSat.

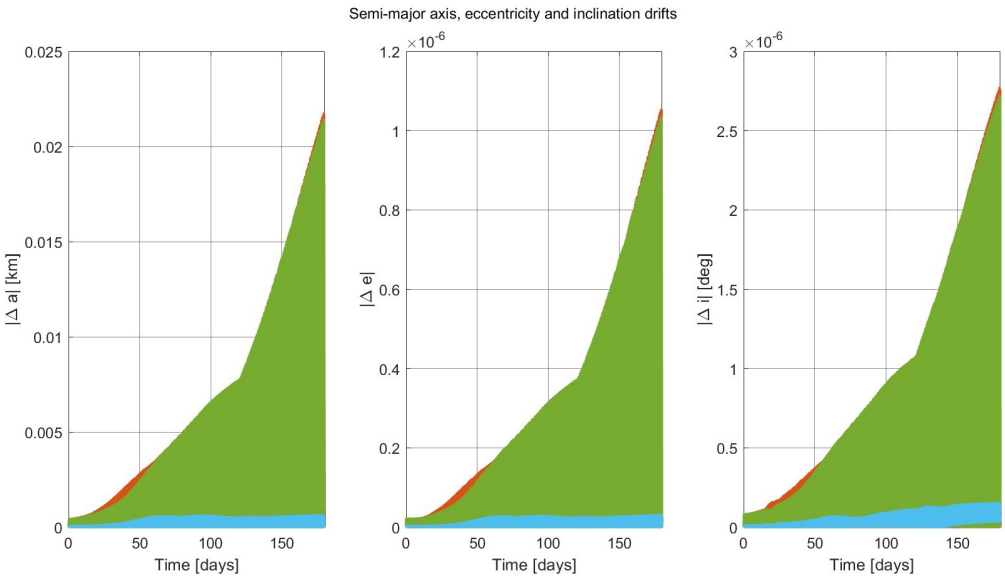

Figure 3.26: Semi-major axis, Eccentricity and Inclination drifts, $\omega = 270°$.

Analysis with $\omega = 315°$ and $\Omega = 0°$

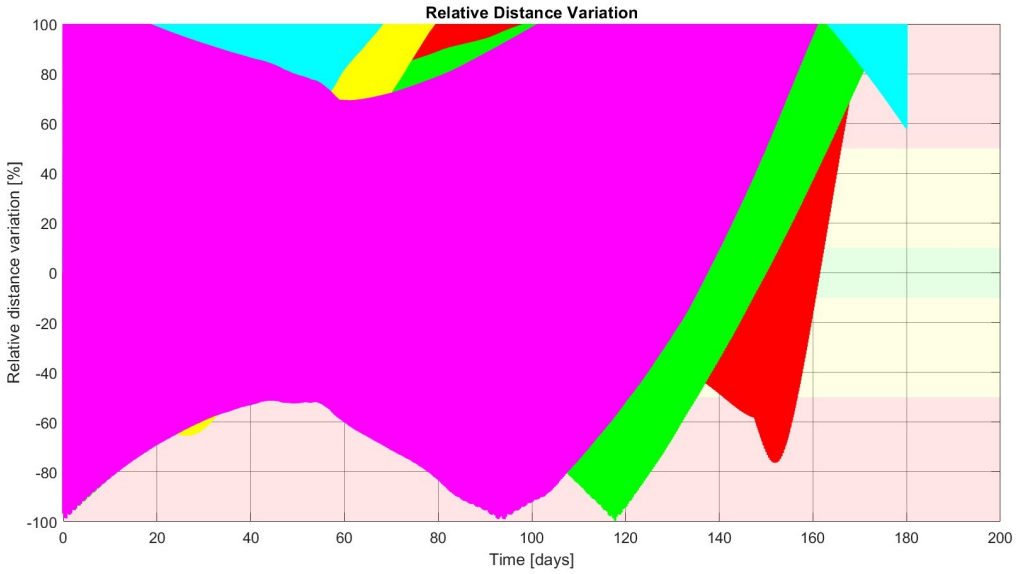

Figure 3.27: Relative distance variation evolution for the spacecraft formation in 500 km heliotropic orbit $\omega = 315°$. Each color represents a CubeSat.

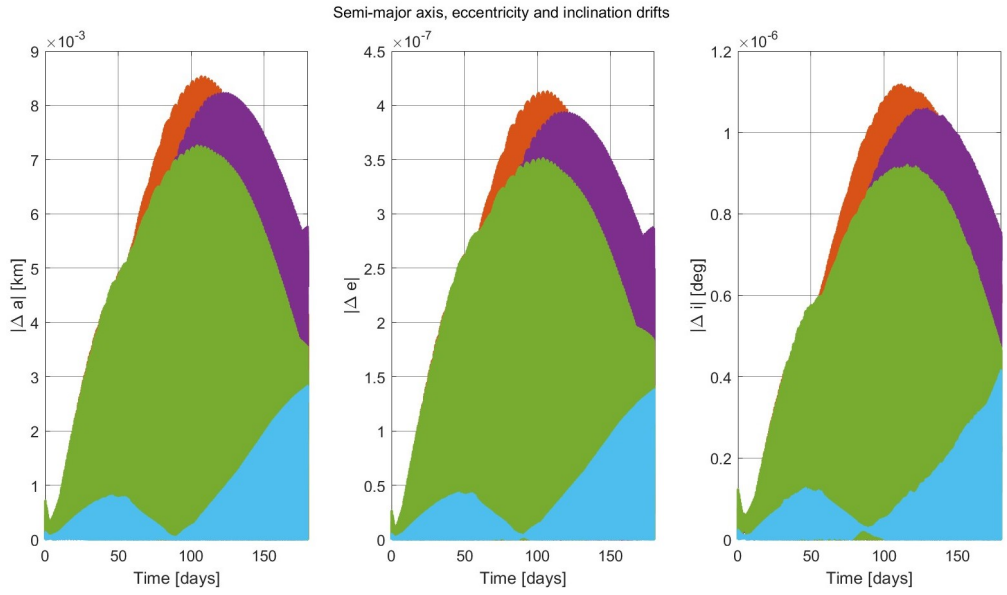

Figure 3.28: Semi-major axis, Eccentricity and Inclination drifts, $\omega = 315°$.

Looking at the previous graphs, it is clear that there is not a strong correlation between the instability and the changes of ω. In each case analyzed, the satellites diverge or collide within a few days. The more stable seems to be the case with $\omega = 270°$.

3.3.2 Influence of Ω on the Formation's Stability

In this Chapter, it is analyzed the influence of Ω on the formation's stability. As done in Chapter 3.3, the position of the formation has been evaluated starting from the chief satellite's position (Tab. 3.5), considering the value of $\omega = 270°$, because it resulted to be the more stable in the study conducted in the previous chapter 3.3.1.

Perigee Radius	r_p	6 878 km
Apogee radius	r_a	16 903,20 km
Semimajor axis	a	11 890,6 km
Inclination	i	97,4014°
RAAN	Ω	0° - 20° - 45° - 80° - 90° - 120° - 180° - 220° - 275° - 290° - 300° - 310° - 320° - 360°
omega	ω	270°
True anomaly	θ	90°

Table 3.6: Classical orbital elements of the chief spacecraft in the formation geometry

Analysis with $\omega = 270°$ and $\Omega = 20°$

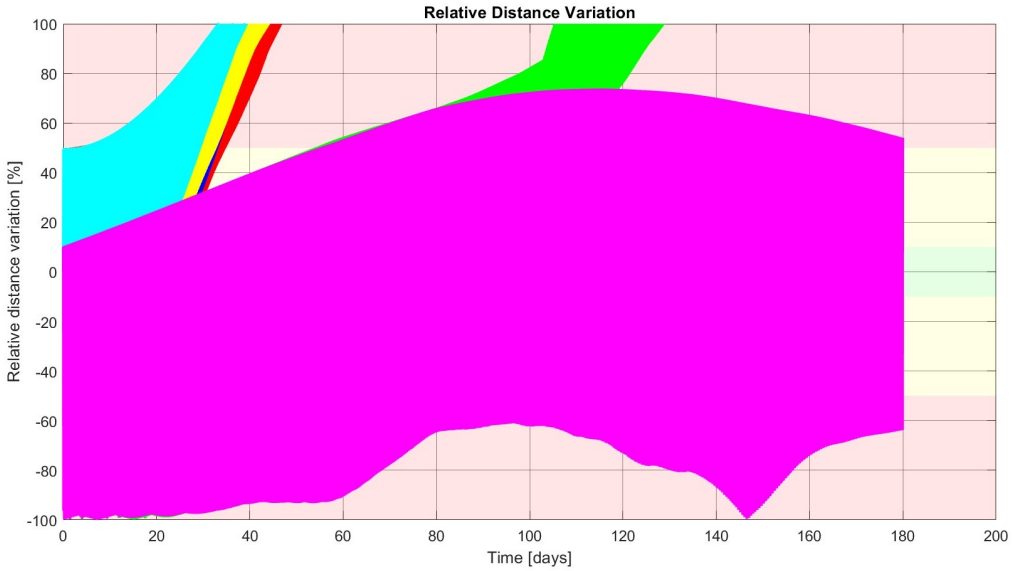

Figure 3.29: Relative distance variation evolution for the spacecraft formation in 500 km heliotropic orbit $\Omega = 20°$. Each color represents a CubeSat.

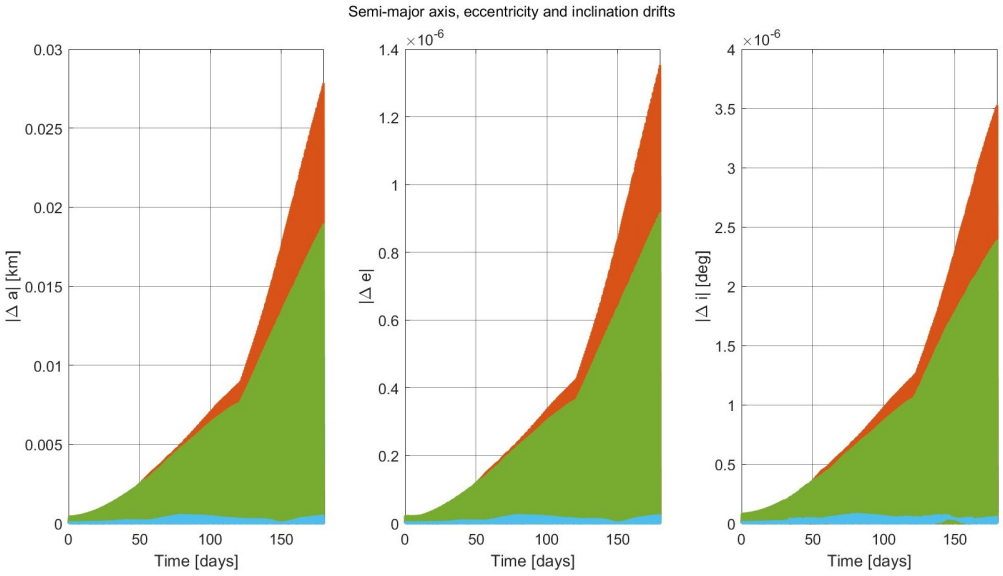

Figure 3.30: Semi-major axis, Eccentricity and Inclination drifts, $\Omega = 20°$.

Analysis with $\omega = 270°$ and $\Omega = 45°$

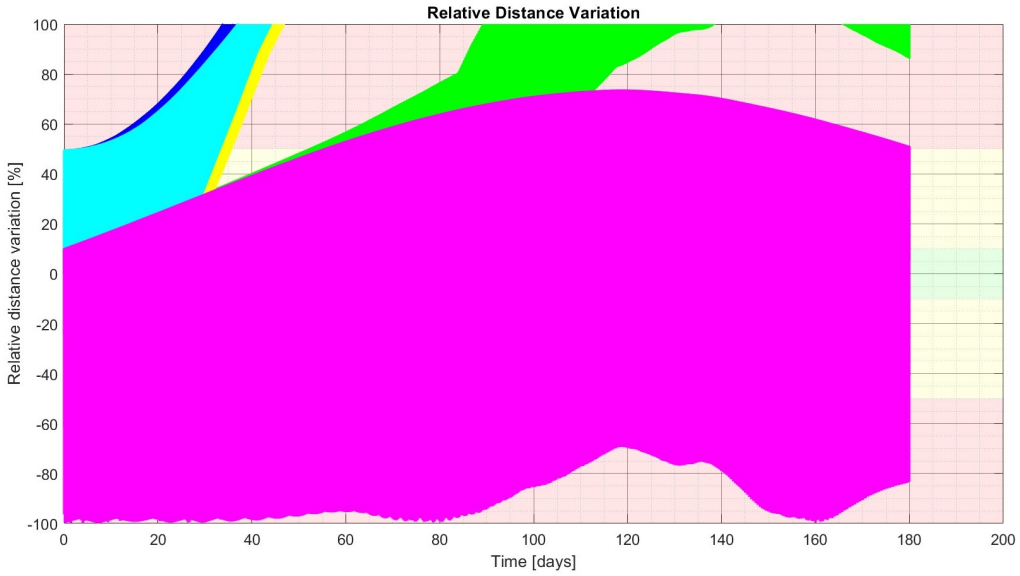

Figure 3.31: Relative distance variation evolution for the spacecraft formation in 500 km heliotropic orbit $\Omega = 45°$. Each color represents a CubeSat.

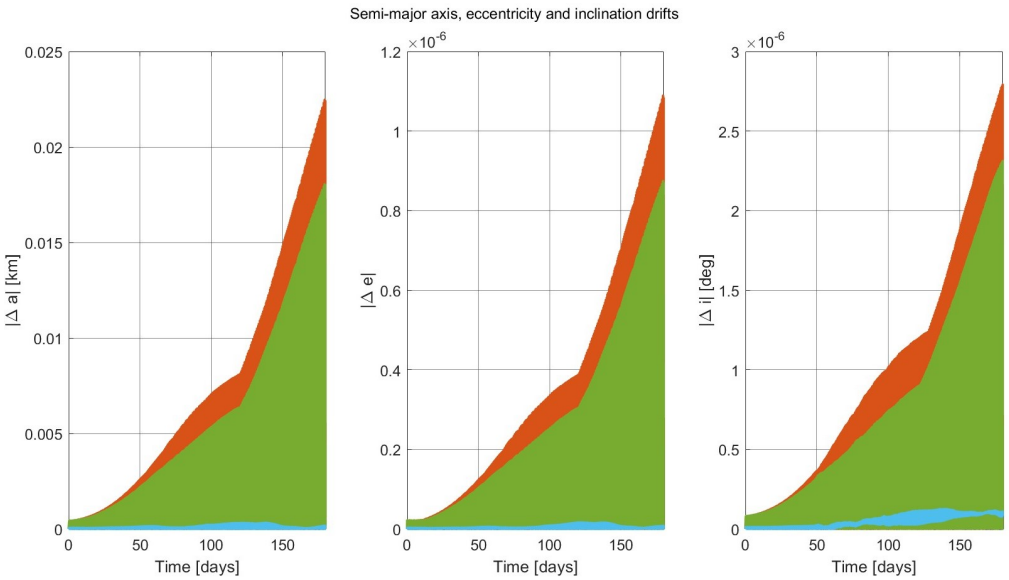

Figure 3.32: Semi-major axis, Eccentricity and Inclination drifts, $\Omega = 45°$.

Analysis with $\omega = 270°$ and $\Omega = 80°$

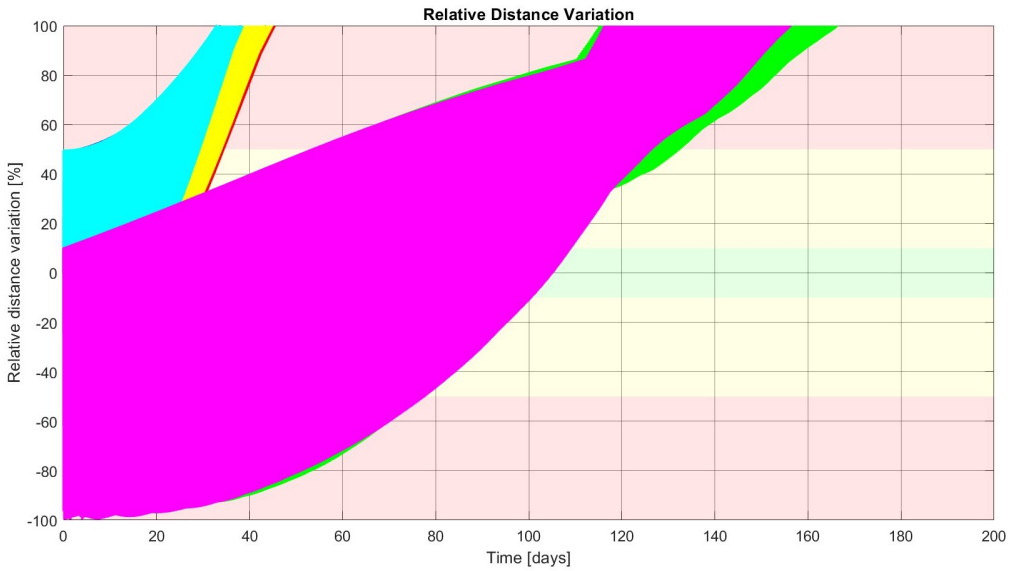

Figure 3.33: Relative distance variation evolution for the spacecraft formation in 500 km heliotropic orbit $\Omega = 80°$. Each color represents a CubeSat.

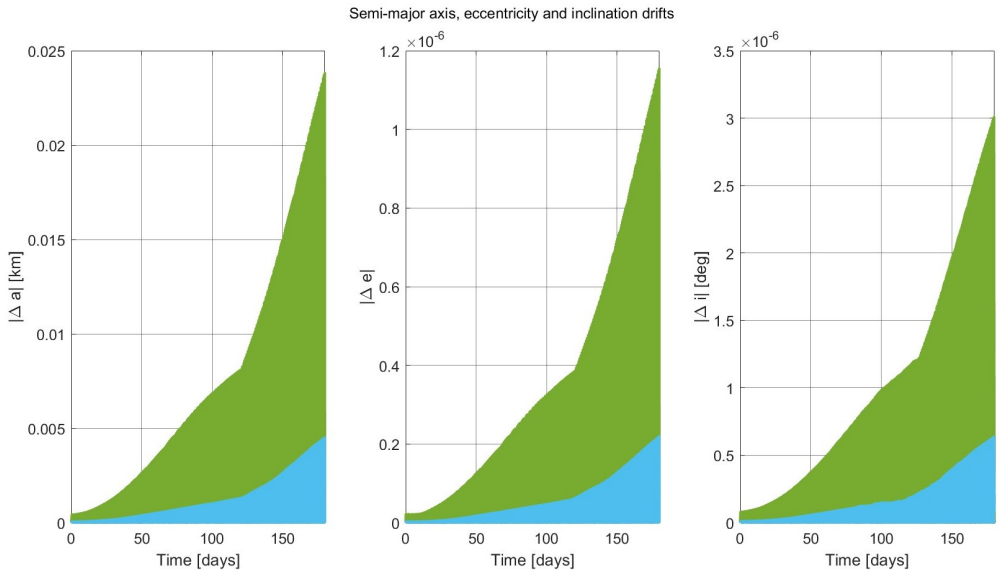

Figure 3.34: Semi-major axis, Eccentricity and Inclination drifts, $\Omega = 80°$.

Analysis with $\omega = 270°$ and $\Omega = 90°$

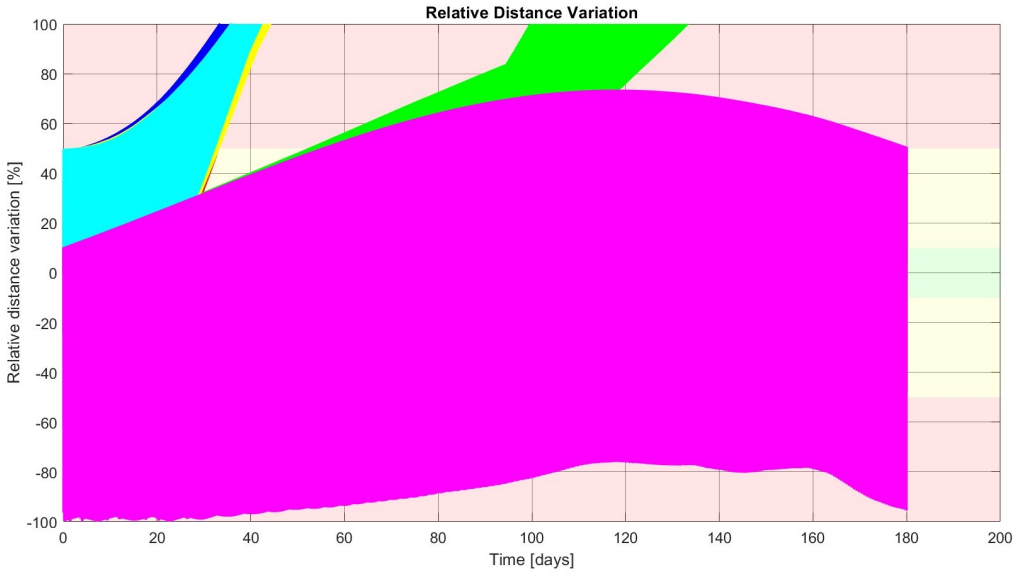

Figure 3.35: Relative distance variation evolution for the spacecraft formation in 500 km heliotropic orbit $\Omega = 90°$. Each color represents a CubeSat.

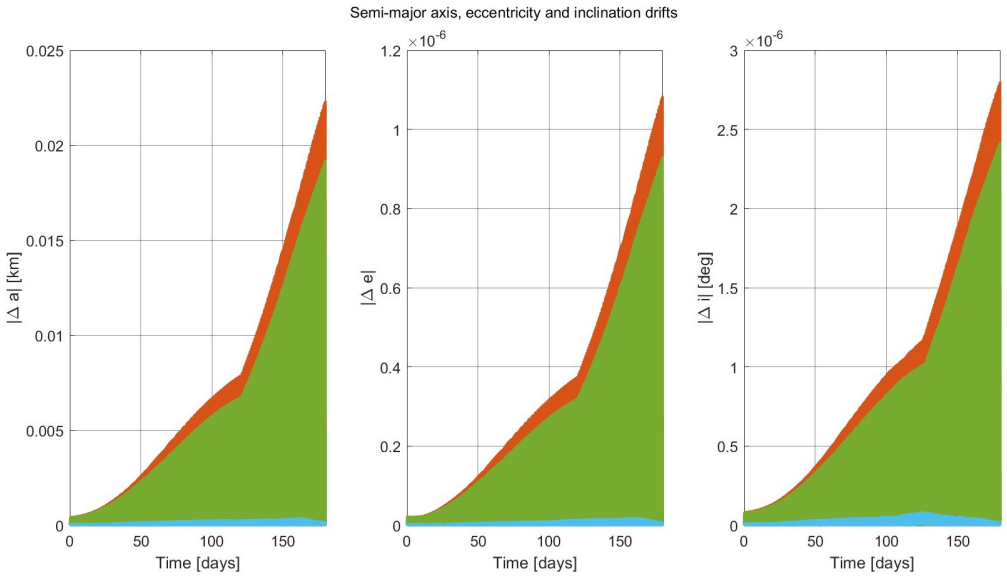

Figure 3.36: Semi-major axis, Eccentricity and Inclination drifts, $\Omega = 90°$.

Analysis with $\omega = 270°$ and $\Omega = 120°$

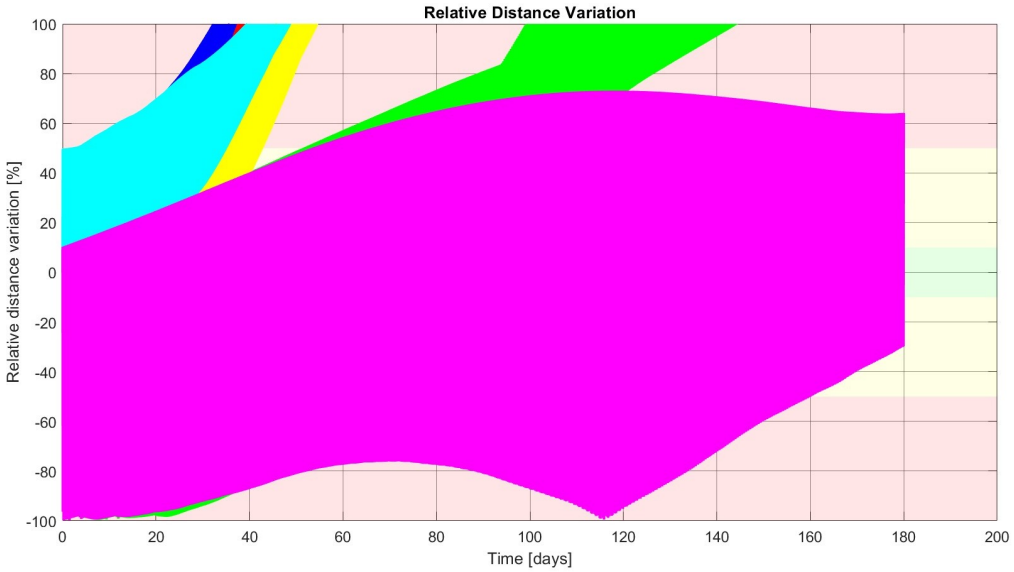

Figure 3.37: Relative distance variation evolution for the spacecraft formation in 500 km heliotropic orbit $\Omega = 120°$. Each color represents a CubeSat.

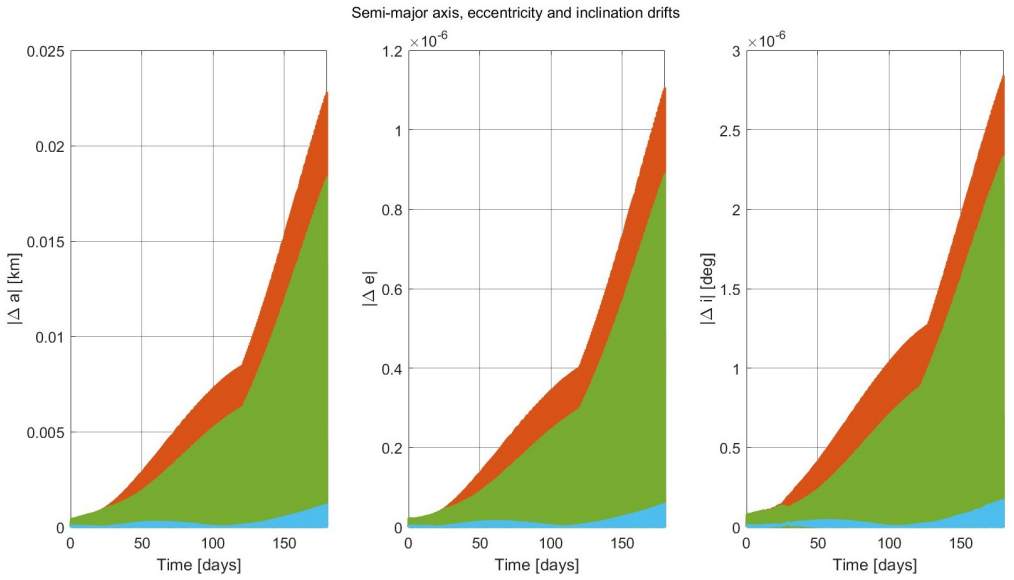

Figure 3.38: Semi-major axis, Eccentricity and Inclination drifts, $\Omega = 120°$.

Analysis with $\omega = 270°$ and $\Omega = 180°$

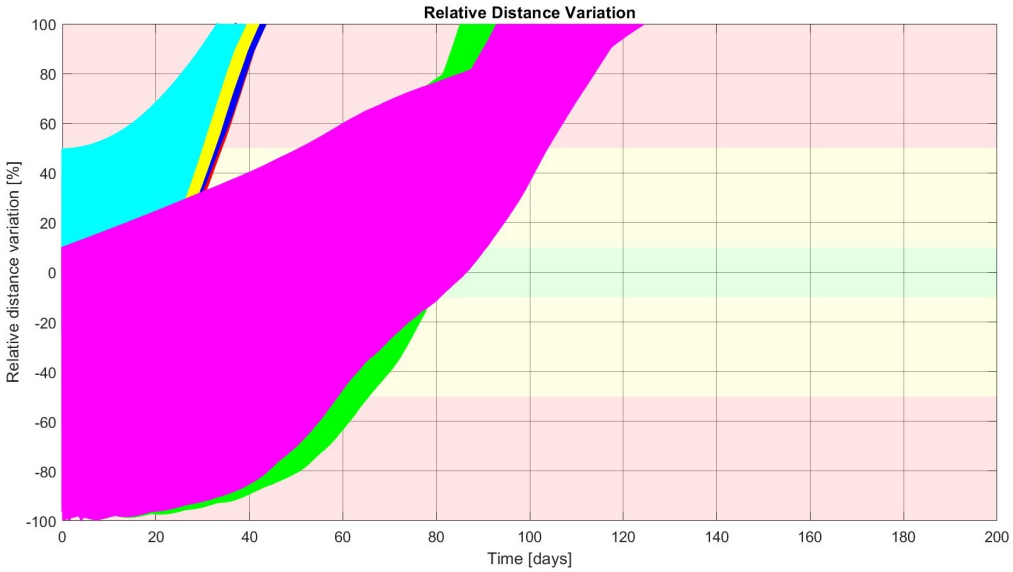

Figure 3.39: Relative distance variation evolution for the spacecraft formation in 500 km heliotropic orbit $\Omega = 180°$. Each color represents a CubeSat.

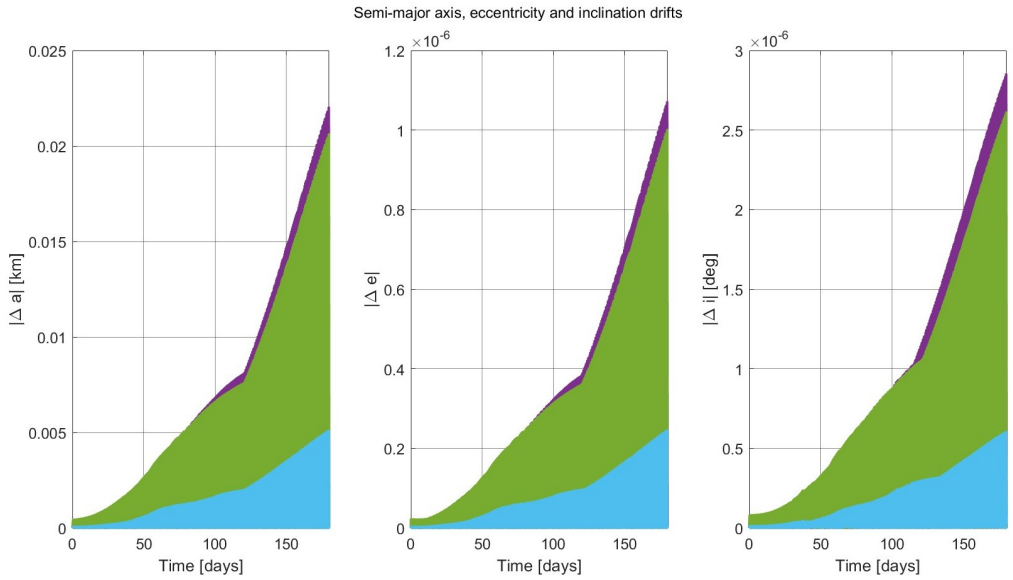

Figure 3.40: Semi-major axis, Eccentricity and Inclination drifts, $\Omega = 180°$.

Analysis with $\omega = 270°$ and $\Omega = 220°$

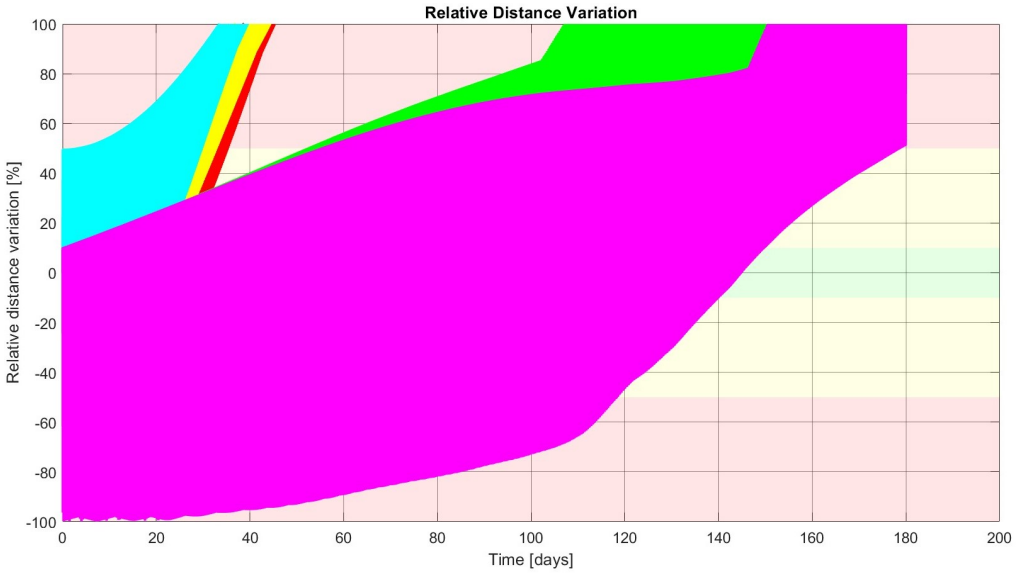

Figure 3.41: Relative distance variation evolution for the spacecraft formation in 500 km heliotropic orbit $\Omega = 220°$. Each color represents a CubeSat.

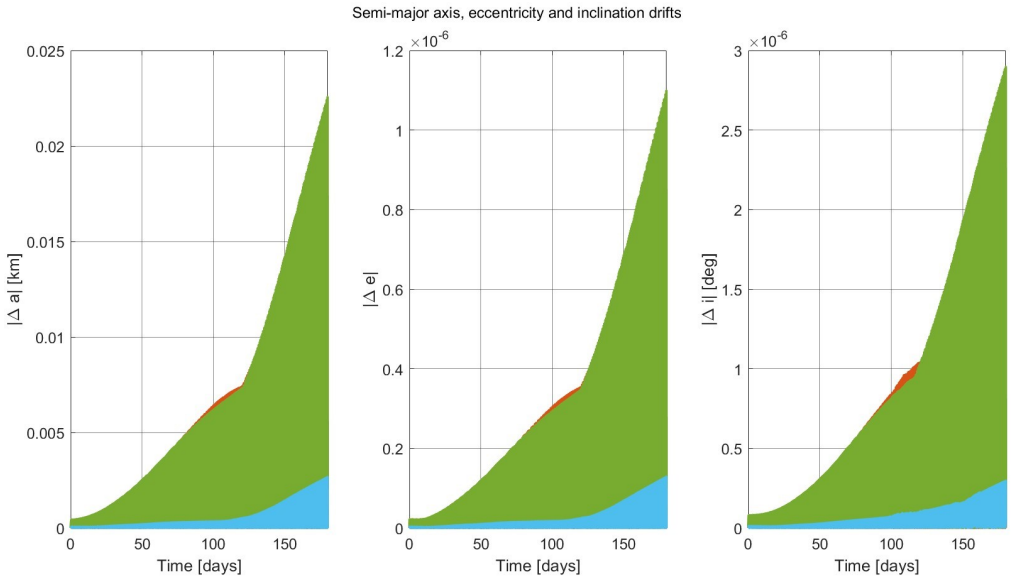

Figure 3.42: Semi-major axis, Eccentricity and Inclination drifts, $\Omega = 220°$.

Analysis with $\omega = 270°$ and $\Omega = 275°$

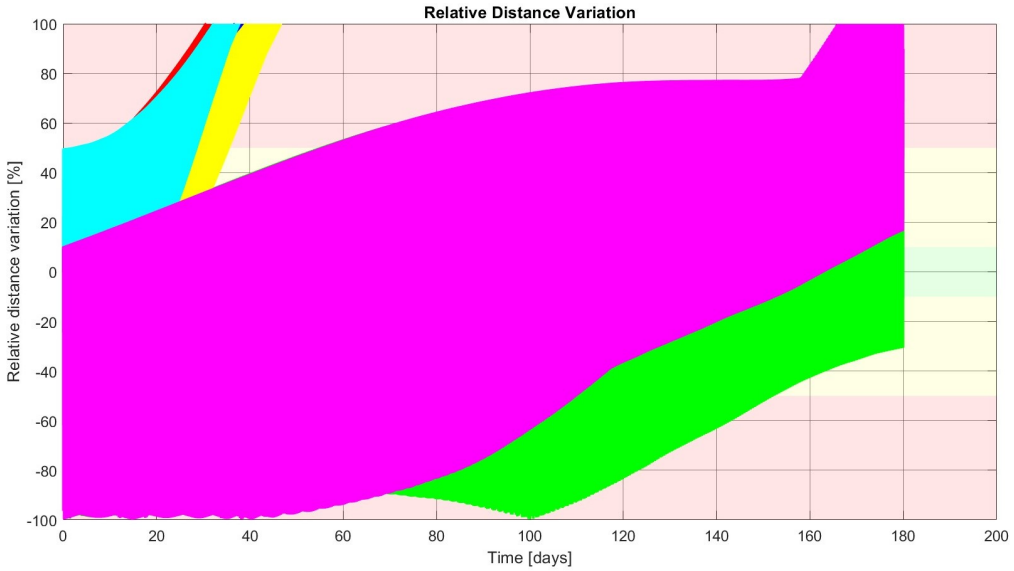

Figure 3.43: Relative distance variation evolution for the spacecraft formation in 500 km heliotropic orbit $\Omega = 275°$. Each color represents a CubeSat.

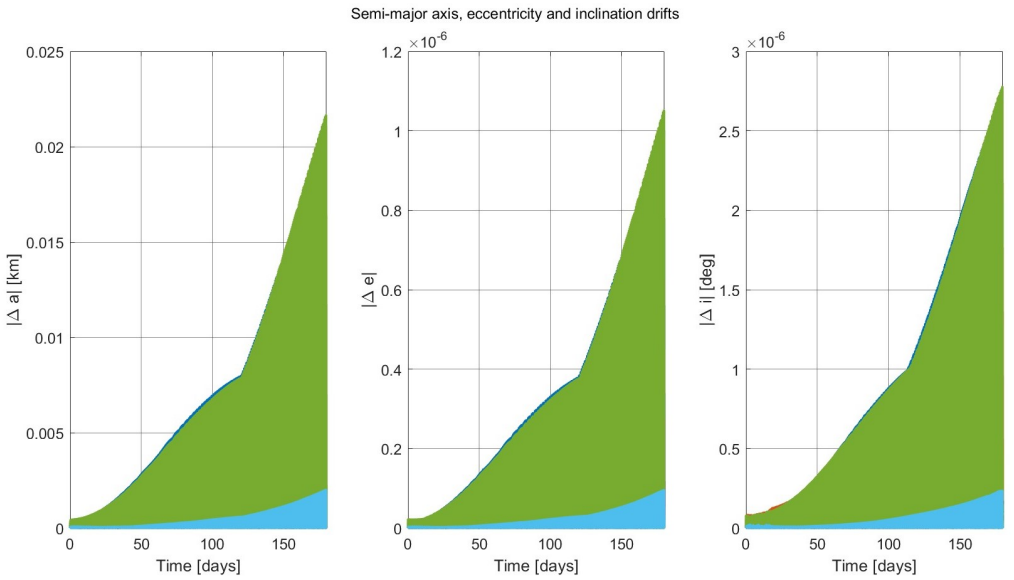

Figure 3.44: Semi-major axis, Eccentricity and Inclination drifts, $\Omega = 275°$.

Analysis with $\omega = 270°$ and $\Omega = 290°$

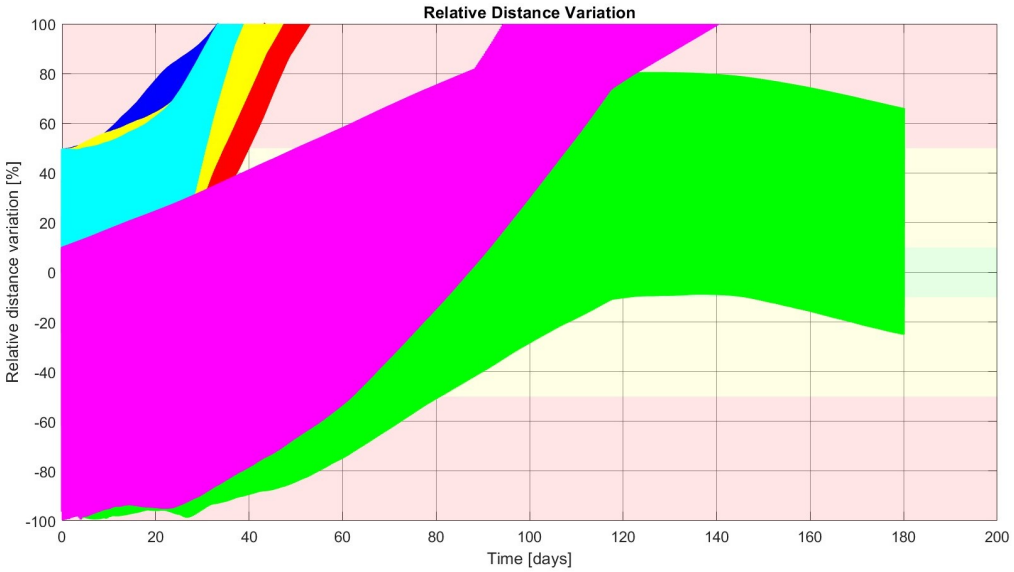

Figure 3.45: Relative distance variation evolution for the spacecraft formation in 500 km heliotropic orbit $\Omega = 290°$. Each color represents a CubeSat.

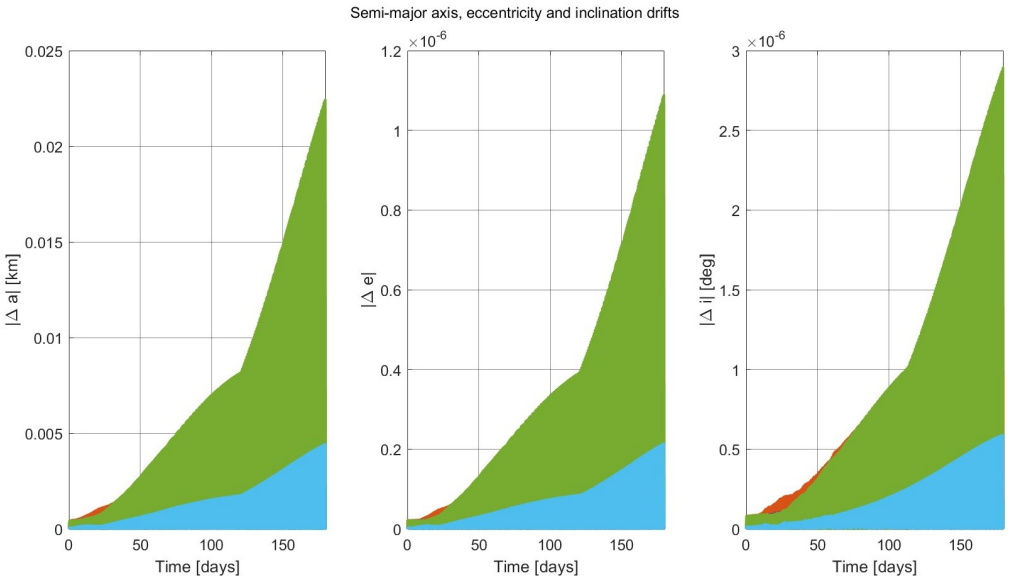

Figure 3.46: Semi-major axis, Eccentricity and Inclination drifts, $\Omega = 290°$.

Analysis with $\omega = 270°$ and $\Omega = 300°$

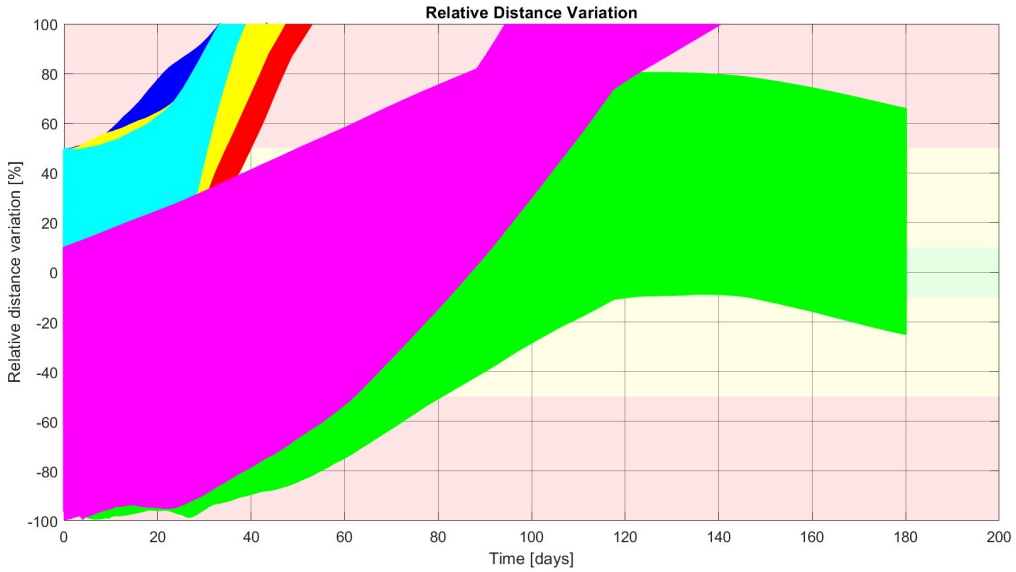

Figure 3.47: Relative distance variation evolution for the spacecraft formation in 500 km heliotropic orbit $\Omega = 300°$. Each color represents a CubeSat.

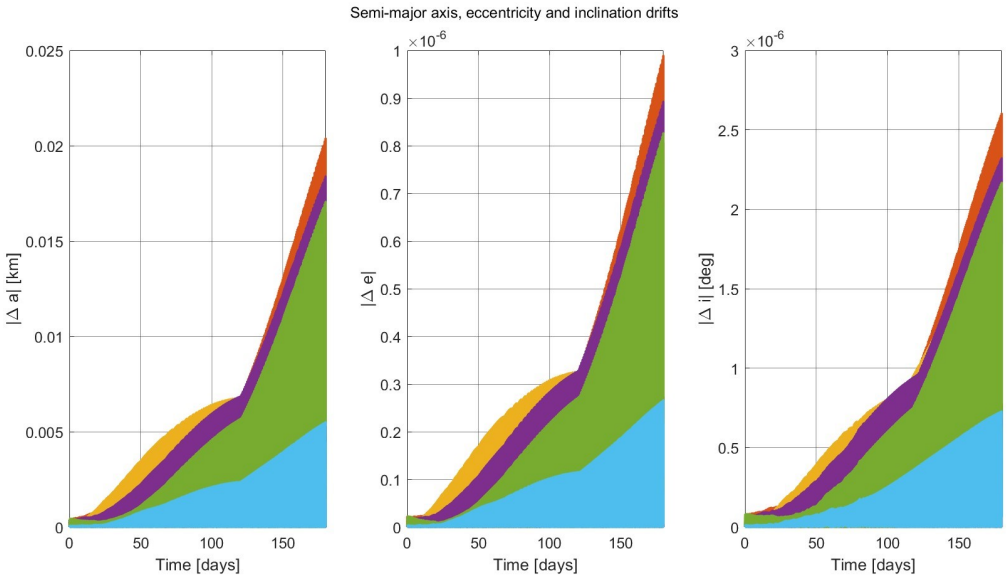

Figure 3.48: Semi-major axis, Eccentricity and Inclination drifts, $\Omega = 300°$.

Analysis with $\omega = 270°$ and $\Omega = 310°$

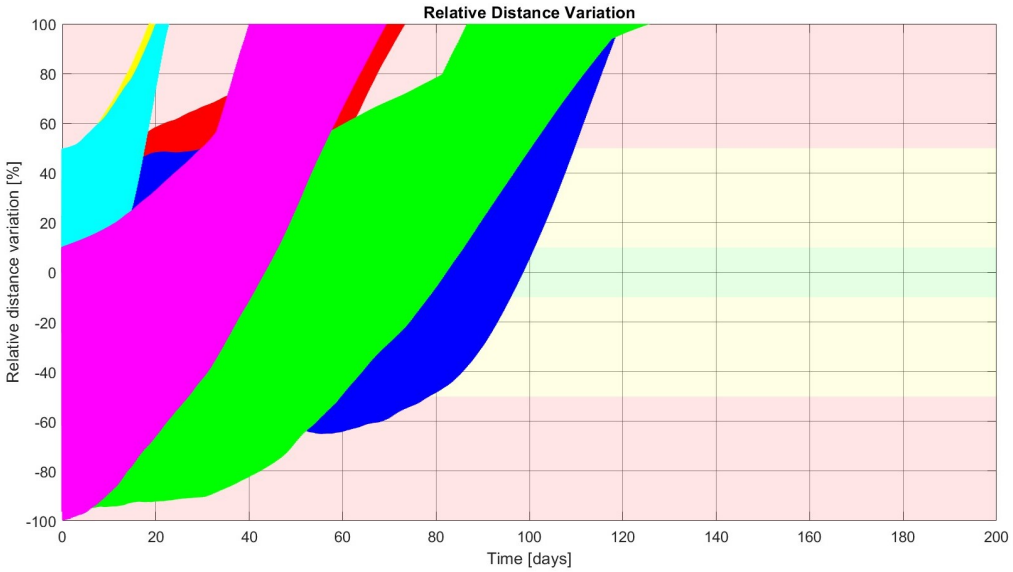

Figure 3.49: Relative distance variation evolution for the spacecraft formation in 500 km heliotropic orbit $\Omega = 310°$. Each color represents a CubeSat.

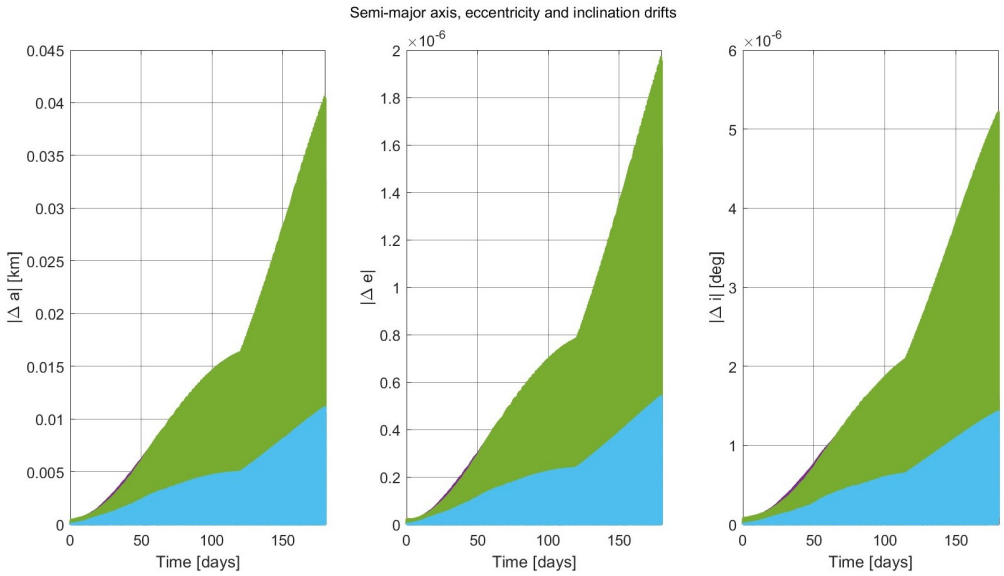

Figure 3.50: Semi-major axis, Eccentricity and Inclination drifts, $\Omega = 310°$.

Analysis with $\omega = 270°$ and $\Omega = 320°$

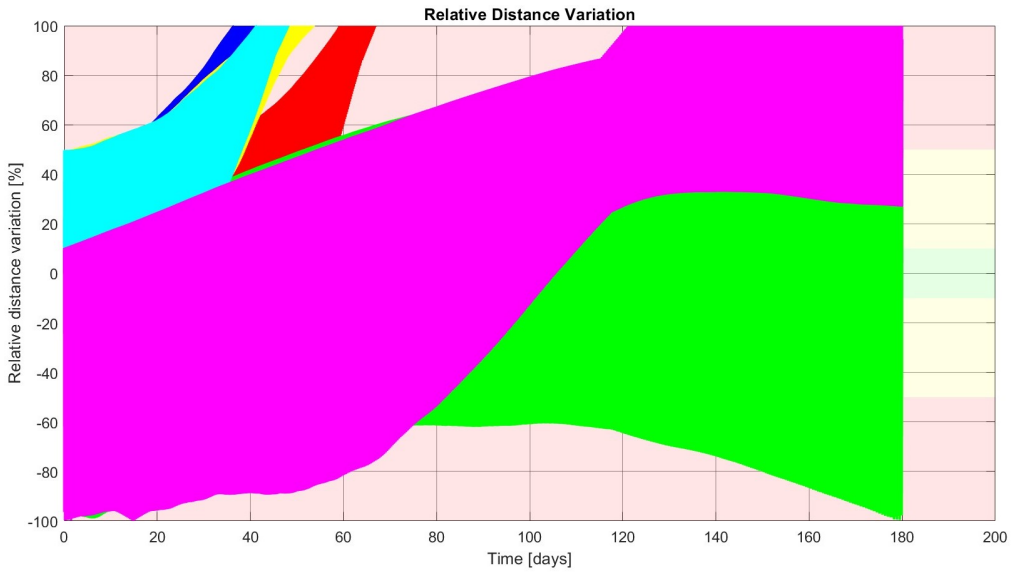

Figure 3.51: Relative distance variation evolution for the spacecraft formation in 500 km heliotropic orbit $\Omega = 320°$. Each color represents a CubeSat.

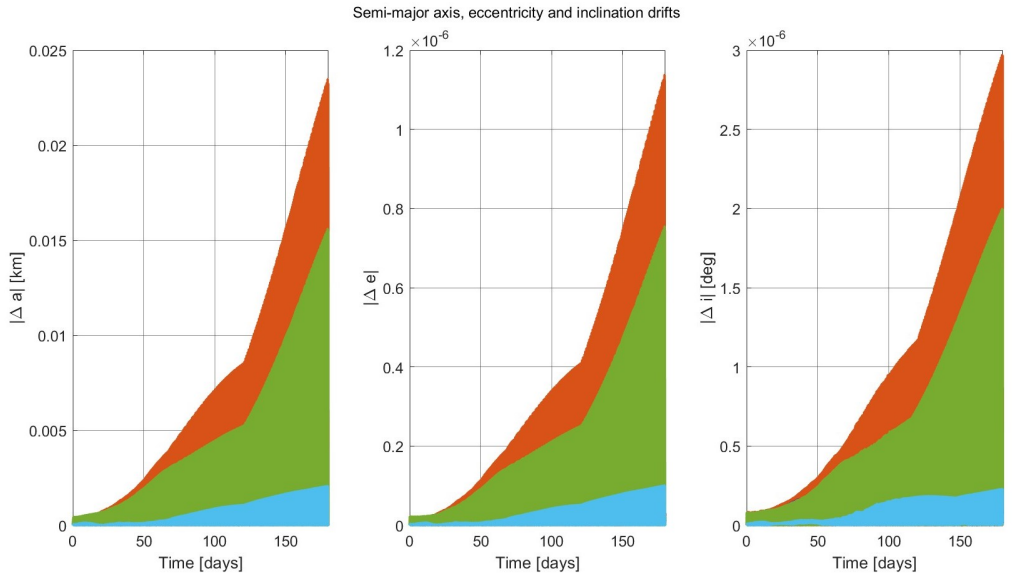

Figure 3.52: Semi-major axis, Eccentricity and Inclination drifts, $\Omega = 320°$.

v

Looking at the previous graphs, as it resulted in chapter 3.3.1, it is clear that there is not a strong correlation between the instability and the changes of Ω. In each case analyzed, the satellites diverge or collide within a few days. The more stable seems to be the case with $\Omega = 300°$. In particular, looking at the graphs of the relative distance variation, for each case two satellites (pink and green ones) seem to change the evolution, instead the evolution of the other four satellites remain the same.

3.3.3 Influence of the Formation's Radius on the Formation's Stability

In this Chapter, it is analyzed the stability of the formation depending on the radius of the formation. As done in Chapter 3.3, the position of the formation has been evaluated starting from the chief satellite's position (Tab. 3.7), considering the value of $\omega = 270°$ and $\Omega = 300°$, because it resulted to be the more stable in the study conducted in the previous chapters 3.3.1 and 3.3.2.

Perigee Radius	r_p	6 878 km
Apogee radius	r_a	16 903,20 km
Semimajor axis	a	11 890,6 km
Inclination	i	97,4014°
RAAN	Ω	300°
omega	ω	270°
True anomaly	θ	90°
Formation's radius	r	$10\,m$ - $100\,m$ - $1000\,m$

Table 3.7: Classical orbital elements of the chief spacecraft in the formation geometry.

Examining the graphs from 3.53 to 3.58, it is evident that instability is present in all three cases studied. This indicates that the formation's radius is not a determining factor for stability, as stability does not depend on it.

Analysis with $r = 10\,m$

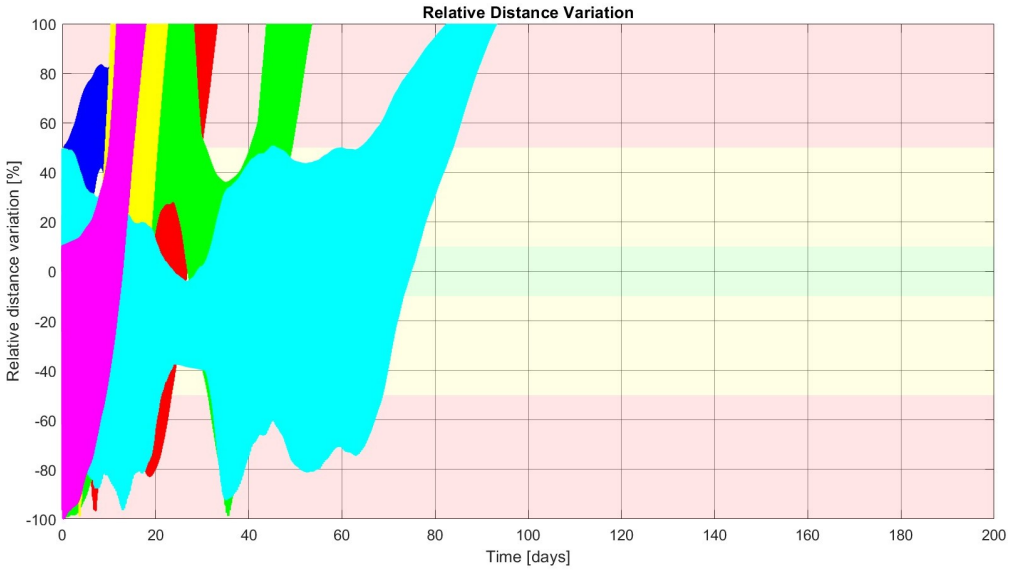

Figure 3.53: Relative distance variation evolution for the spacecraft formation in $500\,km$ heliotropic orbit, formation's radius $r = 10\,m$. Each color represents a CubeSat.

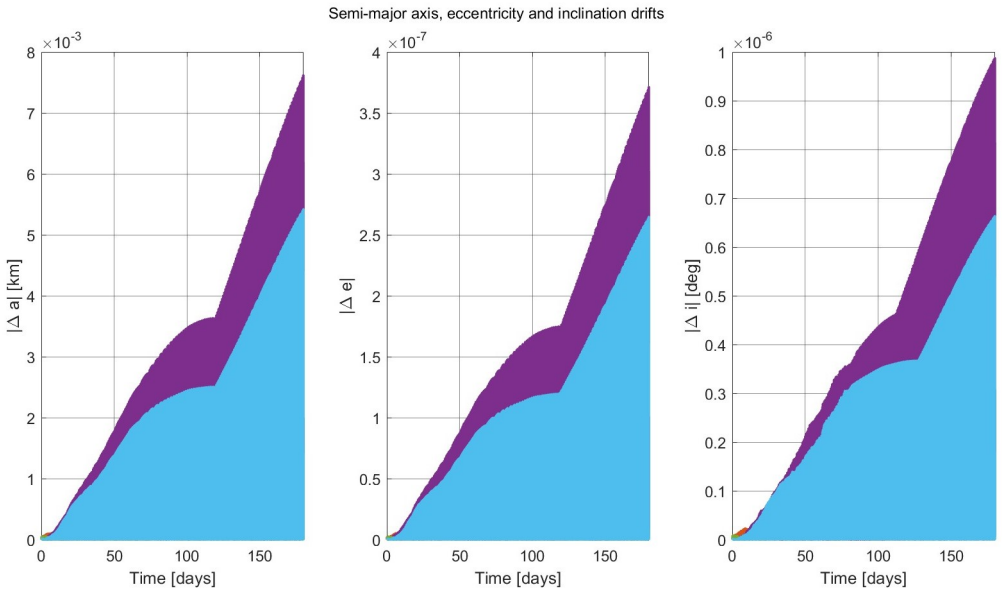

Figure 3.54: Semi-major axis, Eccentricity and Inclination drifts, formation's radius $r = 10\,m$.

Analysis with $r = 100\,m$

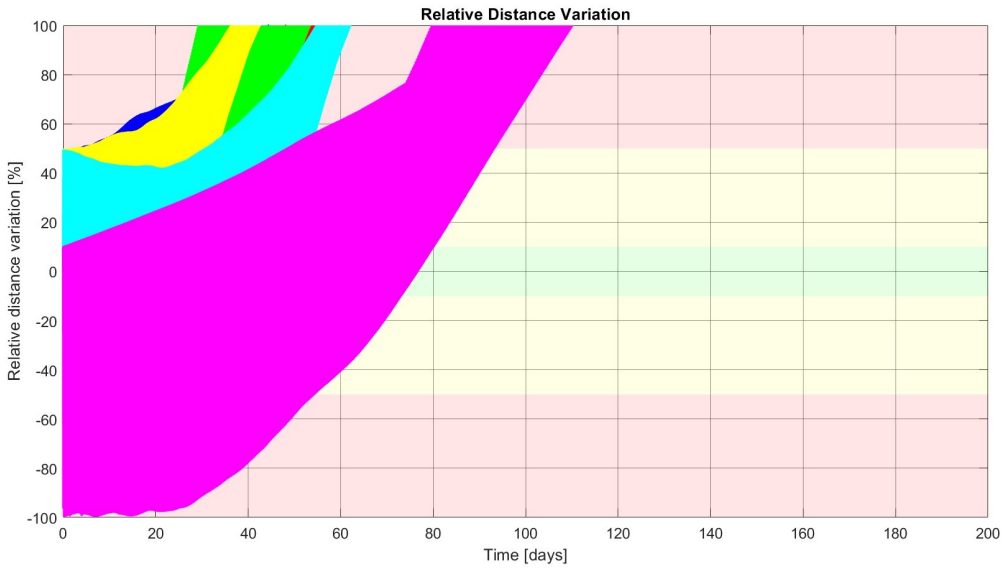

Figure 3.55: Relative distance variation evolution for the spacecraft formation in $500\,km$ heliotropic orbit, formation's radius $r = 100\,m$. Each color represents a CubeSat.

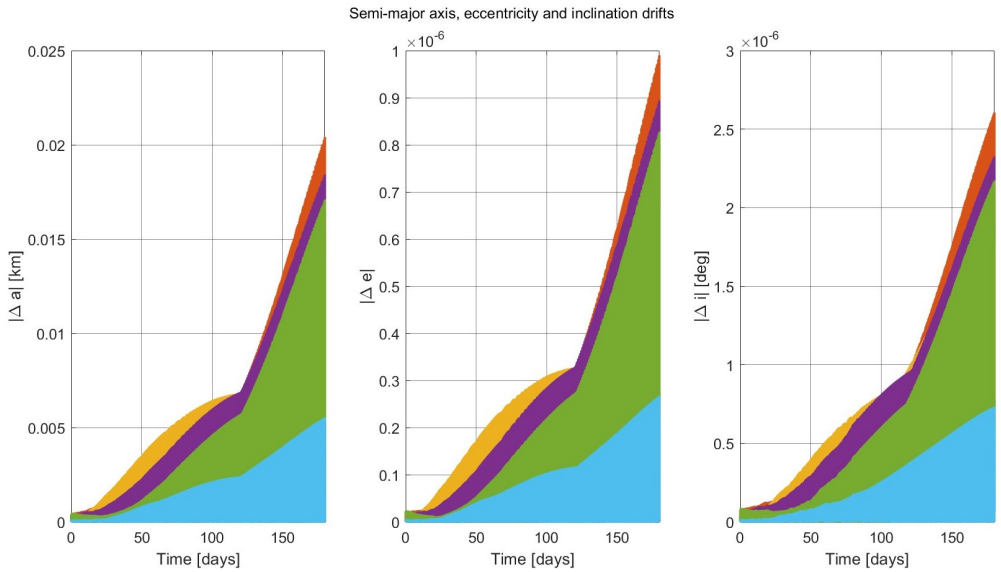

Figure 3.56: Semi-major axis, Eccentricity and Inclination drifts, formation's radius $r = 100\,m$.

Analysis with $r = 1000\,m$

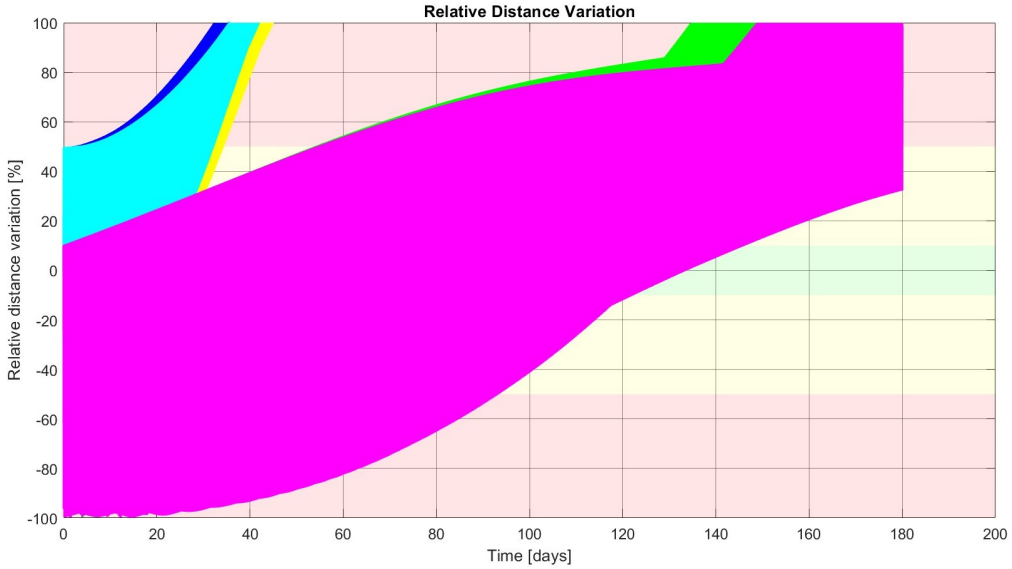

Figure 3.57: Relative distance variation evolution for the spacecraft formation in $500\,km$ heliotropic orbit, formation's radius $r = 1000\,m$. Each color represents a CubeSat.

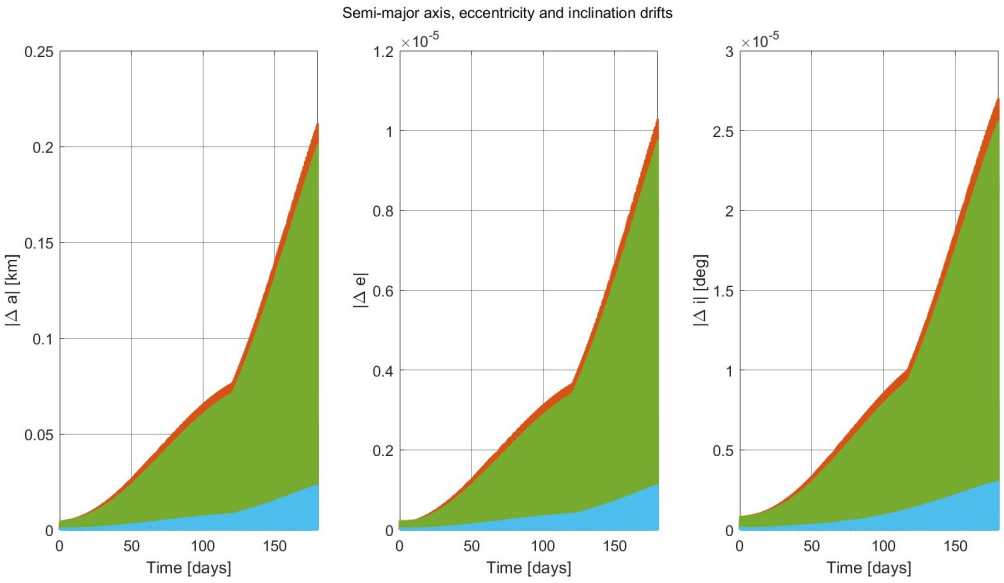

Figure 3.58: Semi-major axis, Eccentricity and Inclination drifts, formation's radius $r = 1000\,m$.

3.3.4 Effect of Single Perturbations

This chapter analyzes the effect of single perturbations on the stability of the formation flying. The studies conducted are considering the chief satellite's orbit described in Tab. 3.8, from which all the six deputy satellites' positions are evaluated.

Perigee Radius	r_p	6 878 km
Apogee radius	r_a	16 903,20 km
Semimajor axis	a	11 890,6 km
Inclination	i	97,4014°
RAAN	Ω	300°
omega	ω	270°
True anomaly	θ	90°
Formation's radius	r	100 m

Table 3.8: Classical orbital elements of the chief spacecraft in the formation geometry.

Keplerian Problem

Starting from the dynamical model described in chapter 2, the analysis is conducted considering one perturbation at a time. Firstly, only the Keplerian problem is considered, without the perturbations. The results are displayed in graphs 3.59 and 3.60. The instability is visible, the satellites will collide because they all are in the region of $RDV_{max} < -75\%$.

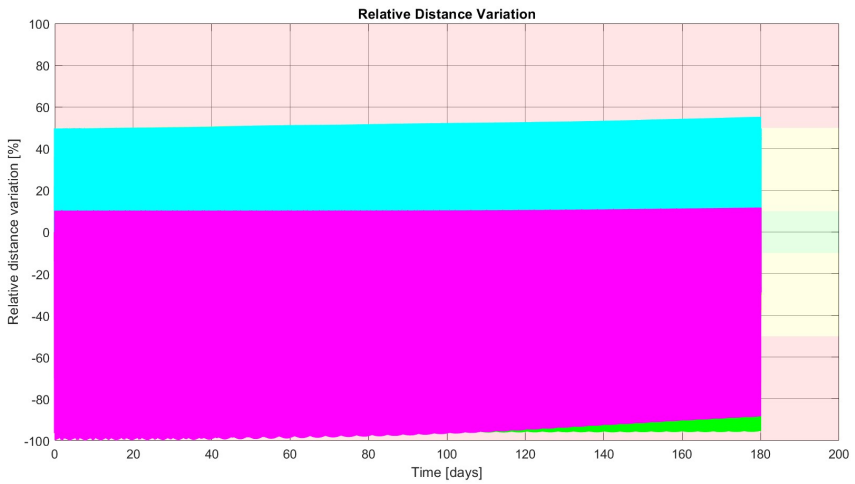

Figure 3.59: Relative distance variation evolution for the spacecraft formation in 500 km Heliotropic orbit, considering only the Keplerian problem. Each color represents a CubeSat.

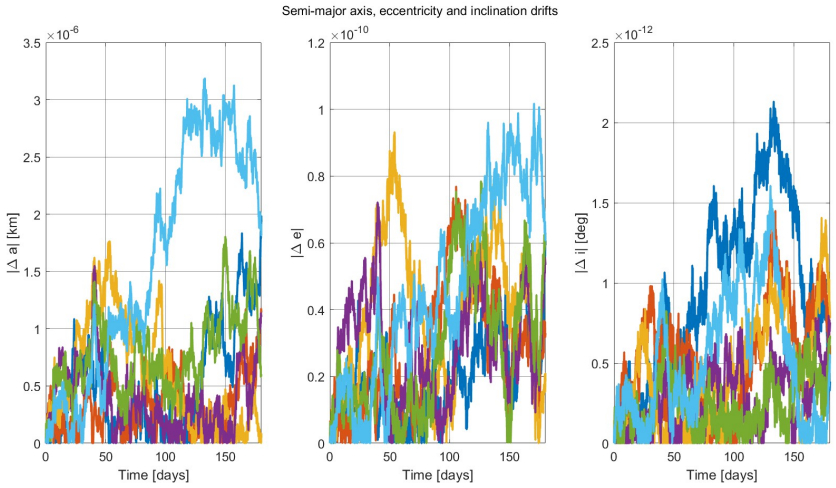

Figure 3.60: Semi-major axis, Eccentricity and Inclination drifts for the spacecraft formation in 500 km Heliotropic orbit, considering only the Keplerian problem.

Drag Perturbation

In this case, the drag perturbation effect is considered in addition to the Keplerian problem. The results are displayed in graphs 3.61 and 3.62.

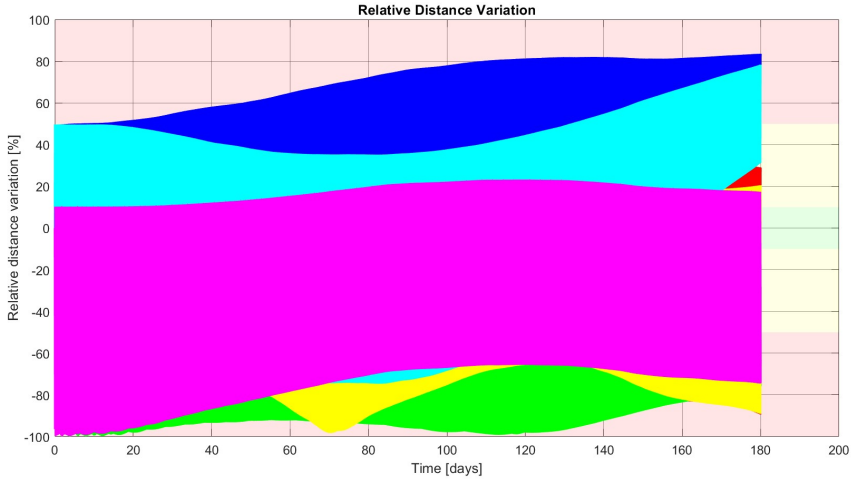

Figure 3.61: Relative distance variation evolution for the spacecraft formation in 500 km Heliotropic orbit, considering only the drag perturbation (in addition to the Keplerian problem). Each color represents a CubeSat.

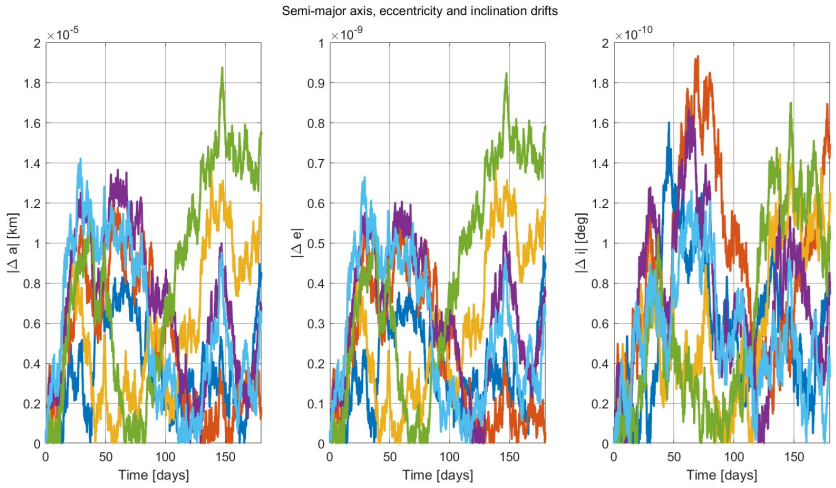

Figure 3.62: Semi-major axis, Eccentricity and Inclination drifts for the spacecraft formation in 500 km Heliotropic orbit, considering only the drag perturbation (in addition to the Keplerian problem).

Solar Radiation Pressure Perturbation

In this case, the solar radiation pressure perturbation effect is considered in addition to the Keplerian problem. The results are displayed in graphs 3.63 and 3.64.

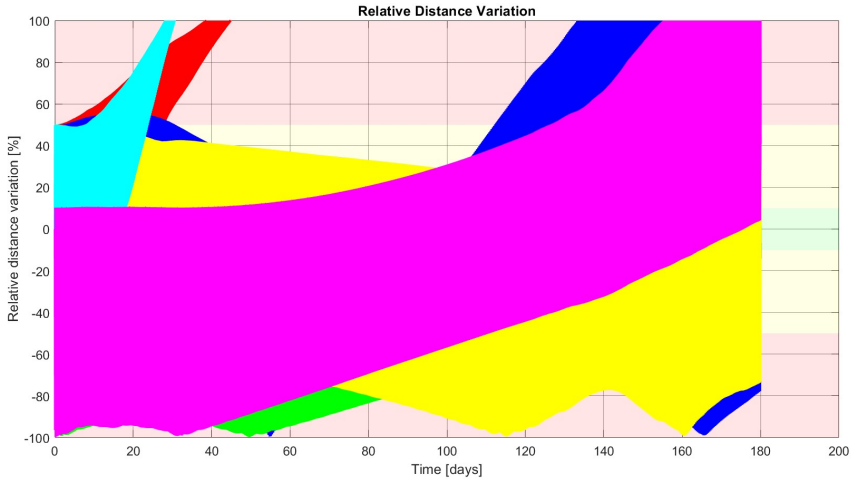

Figure 3.63: Relative distance variation evolution for the spacecraft formation in 500 km Heliotropic orbit, considering only the solar radiation pressure perturbation (in addition to the Keplerian problem). Each color represents a CubeSat.

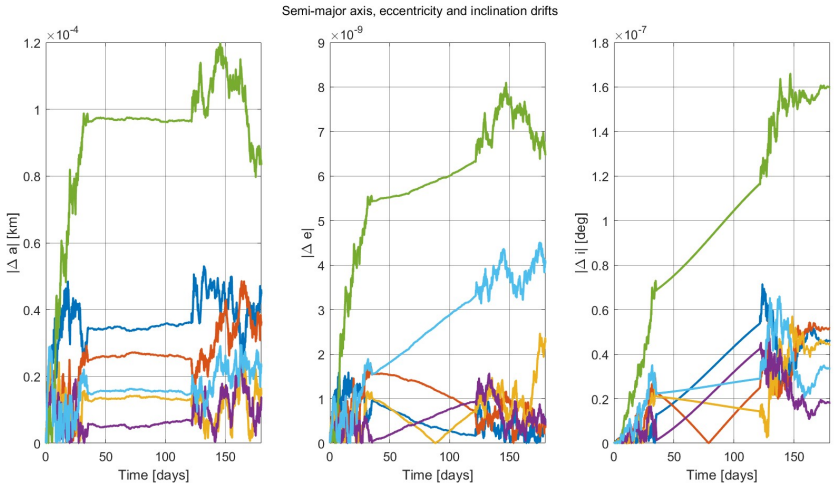

Figure 3.64: Semi-major axis, Eccentricity and Inclination drifts for the spacecraft formation in 500 km Heliotropic orbit, considering only the solar radiation pressure perturbation (in addition to the Keplerian problem).

Gravitational J2 Perturbation

In this case, the gravitational perturbation J2 effect is considered in addition to the Keplerian problem. The results are displayed in graphs 3.65 and 3.66.

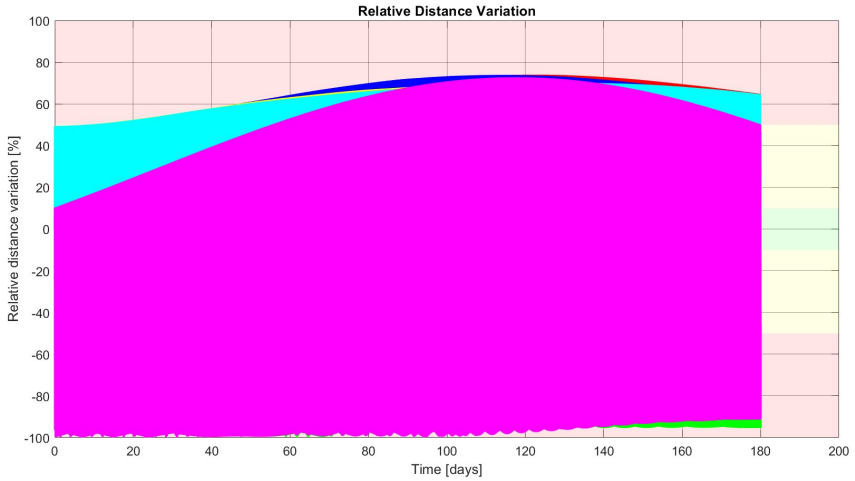

Figure 3.65: Relative distance variation evolution for the spacecraft formation in 500 km Heliotropic orbit, considering only the gravitational J2 perturbation (in addition to the Keplerian problem). Each color represents a CubeSat.

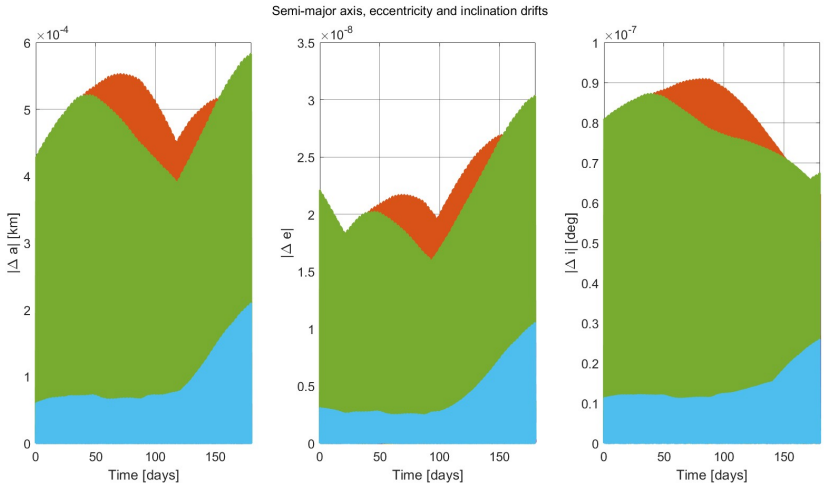

Figure 3.66: Semi-major axis, Eccentricity and Inclination drifts for the spacecraft formation in 500 km Heliotropic orbit, considering only the gravitational J2 perturbation (in addition to the Keplerian problem).

Gravitational J3 Perturbation

In this case, the gravitational perturbation J3 effect is considered in addition to the Keplerian problem. The results are displayed in graphs 3.67 and 3.68.

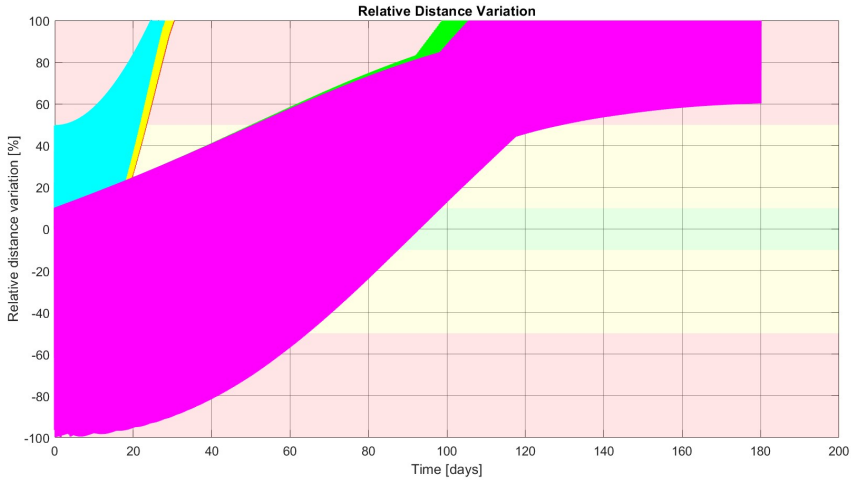

Figure 3.67: Relative distance variation evolution for the spacecraft formation in 500 km Heliotropic orbit, considering only the gravitational J3 perturbation (in addition to the Keplerian problem). Each color represents a CubeSat.

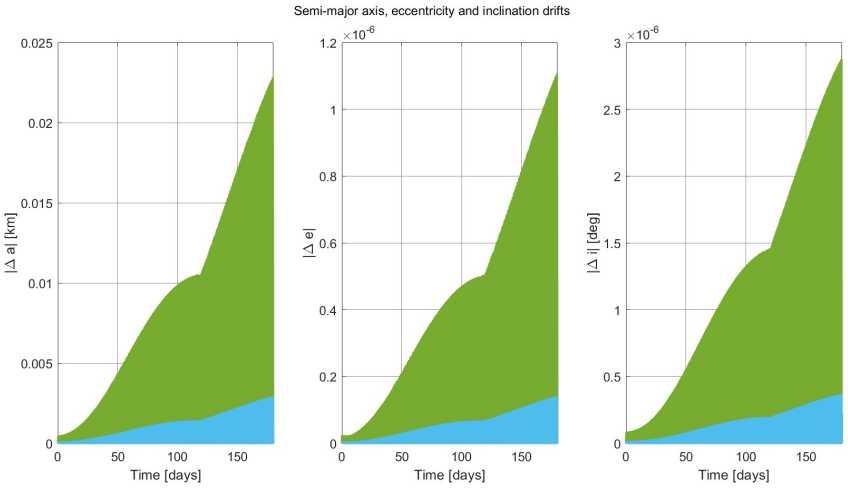

Figure 3.68: Semi-major axis, Eccentricity and Inclination drifts for the spacecraft formation in 500 km Heliotropic orbit, considering only the gravitational J3 perturbation (in addition to the Keplerian problem).

Gravitational J4 Perturbation

In this case, the gravitational perturbation J4 effect is considered in addition to the Keplerian problem. The results are displayed in graphs 3.69 and 3.70.

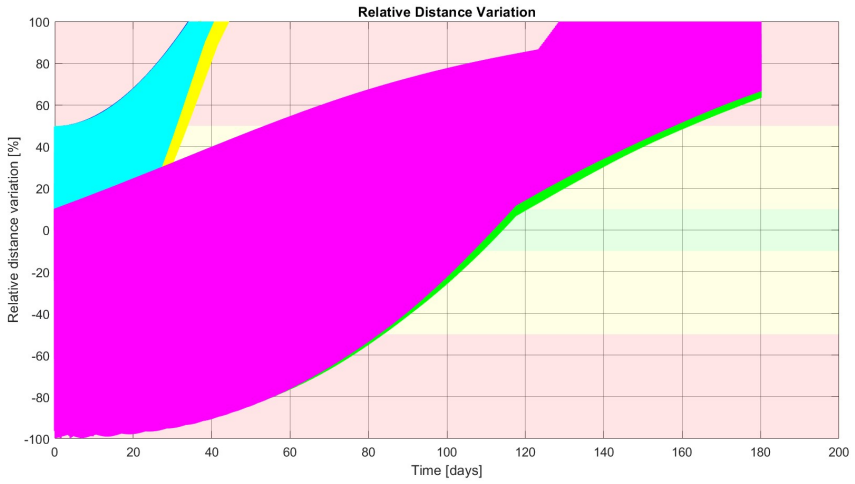

Figure 3.69: Relative distance variation evolution for the spacecraft formation in 500 km Heliotropic orbit, considering only the gravitational J4 perturbation (in addition to the Keplerian problem). Each color represents a CubeSat.

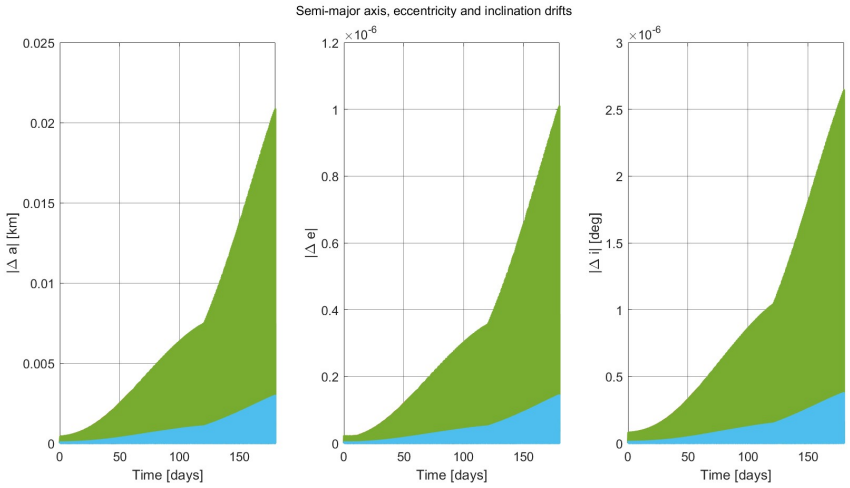

Figure 3.70: Semi-major axis, Eccentricity and Inclination drifts for the spacecraft formation in 500 km Heliotropic orbit, considering only the gravitational J4 perturbation (in addition to the Keplerian problem).

From the results in chapter 3.3.4, it is possible to deduce that the formation flying is unstable even in the case without the perturbation effects. The most effective perturbations on the instability are the solar radiation pressure and the gravitational perturbations. Indeed, in the graphs 3.67 and 3.69, which study the gravitational effects considering up to the J3 and J4 gravitational harmonics, it is noticeable that some satellites tend to collide at the beginning of the analysis, while others remain stable for some time before eventually diverging.

3.4 Satellite-to-Site Visibility Analysis

The satellite-to-site visibility problem involves determining the opportunities for a satellite to observe or communicate with an object on Earth's surface. This is crucial for analyzing the coverage of satellite orbits and constellations. [27] The satellite-to-site visibility periods are usually determined by the conventional brute force method, where the satellite's trajectory is tracked, and its access to the site is checked at each moment. The downside of this approach is that orbital positions must be calculated hundreds of times per orbit, leading to significant execution time, especially when considering perturbation effects. Even though the computation load is tolerable for ground facilities, it is undesirable for onboard real-time mission planning. Therefore, developing fast algorithms for visibility computation is essential for both ground-based constellation design and onboard spacecraft autonomy.

For this analysis, it has been used a mathematical model of the satellite-to-site visibility problem and generalize it as a multiple hump function rooting problem. [11]

A satellite cannot see a ground target until it rises above a minimum elevation angle. Let θ denote the elevation angle of the satellite at the current position, and θ_0 denote the predefined minimum elevation. As displayed in Fig. 3.71 , $\pi/2 - \theta$ equals the angle between the position vector of the ground target and the relative position vector from the ground target to the satellite. The visibility criterion is thus given as follows.[11]

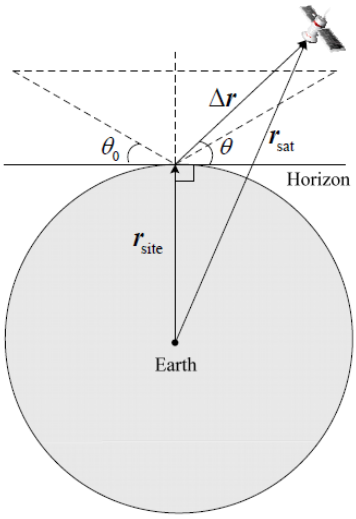

Figure 3.71: Geometric illustration of the satellite-to-site visibility.[11]

The visibility criterion is thus given as follows:

$$\frac{\Delta\vec{r} \cdot \vec{r}^{0}_{site}}{|| \Delta\vec{r} ||} \geq sin\ \theta_0 \tag{3.39}$$

where $\Delta\vec{r} = \vec{r}_{sat} - \vec{r}_{site}$, $\vec{r}^{0}_{site} = \vec{r}_{site}/|| \vec{r}_{site} ||$, $\vec{r}_{sat}$ and $\vec{r}_{sat}$ are the position vectors of the satellite and the ground target, respectively, and $|| \cdot ||$ denotes the magnitude of a vector.

The term of on the left side of Eq. 3.39 is defined as the visibility function denoted by $V(t)$, and varies with time. While the term on the right side is a constant and is defined as the visibility threshold, denoted by λ. The rise and set times are the solutions of the following nonlinear equation

$$V(t) - \lambda = 0 \tag{3.40}$$

The satellite sees the ground target only when the visibility function value is above the threshold line. The visibility analysis has been conducted for the orbit that had been analyzed in chapter 3.3, considering the classical orbital elements in Tab. 3.3. In Fig. 3.72 the orbit is represented in a geocentric equatorial frame. For the ground facilities, two cases have been selected: the first one is assumed to be located right under the orbit's perigee, the second one is assumed to be located under the orbit's apogee. These are represented in Fig. 3.73 in a geocentric equatorial frame.

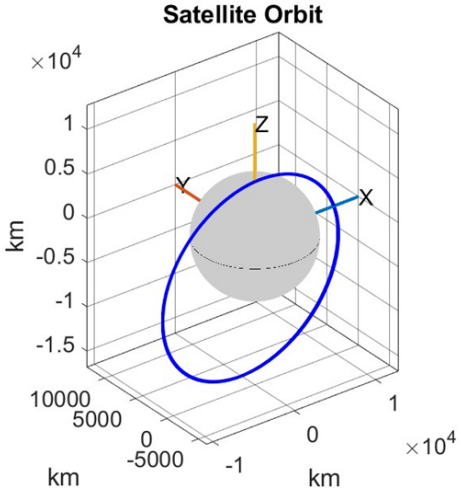

Figure 3.72: Heliotropic orbit with altitude of 500 km and inclination 97,4014°

The visibility function is calculated for the case of Ground Station under the perigee, using a minimum elevation angle of $\theta = 0°$. As depicted in Fig. 3.74, the visibility function is a multiple hump function. In order to have a better understanding of the timing of visibility, the graph has been transformed. In Fig.3.75, the visibility function is displayed as being equal to 0 when the function is below the threshold, and equal to 1 when the function intersects or exceeds the threshold.

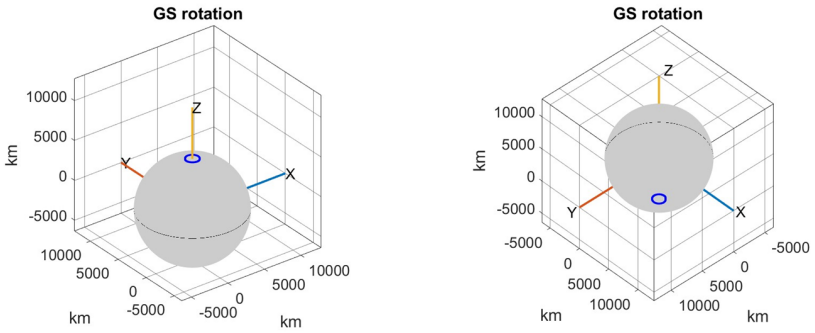

Figure 3.73: Ground stations' position over time. They are assumed to be located under the orbit's perigee and apogee.

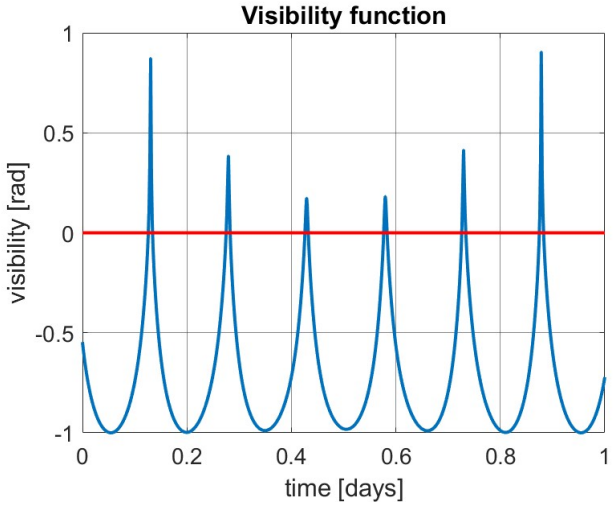

Figure 3.74: The visibility function in blue, the threshold in red.

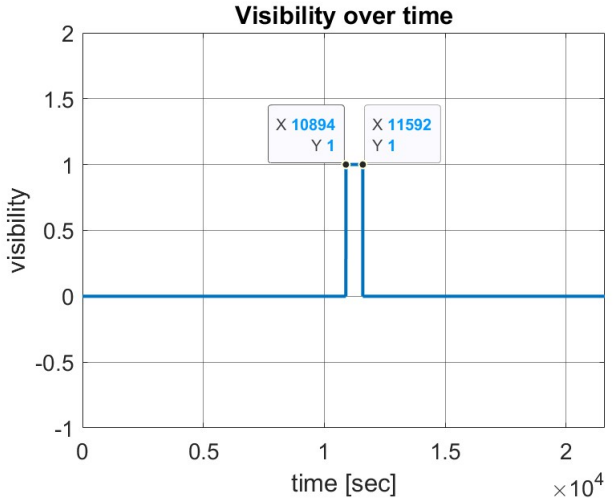

Figure 3.75: The visibility function is represented as being 0 or 1.

This representation simplifies the evaluation of the timing. For this case, the timing of visibility is $T_{perigee} = 11592 - 10894 = 698\ sec$.

The same analysis is conducted for the case of the Ground Station being under the orbit's apogee, the result displayed in Fig. 3.76 and 3.77 indicates that the visibility time is $T_{apogee} = 8594 - 1037 = 7557\ sec$.

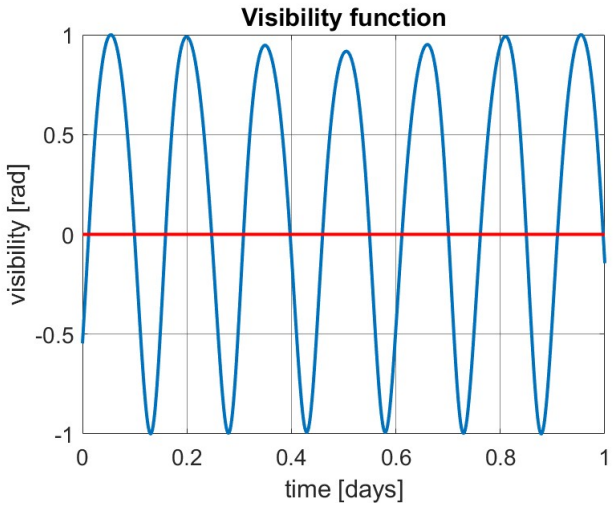

Figure 3.76: The visibility function in blue, the threshold in red.

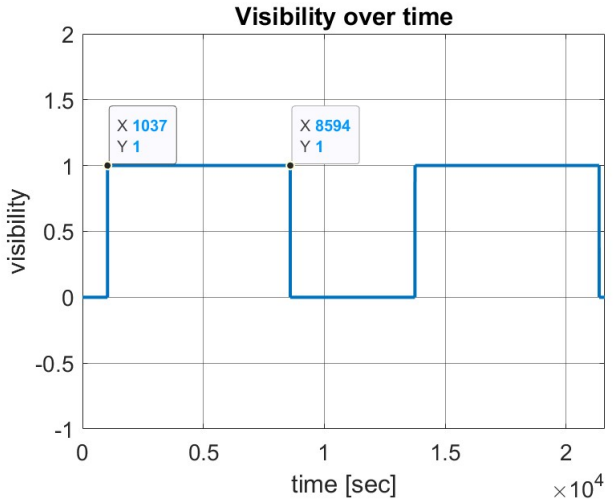

Figure 3.77: The visibility function is represented as being 0 or 1.

Chapter 4

Sun Position Analysis

In the following chapter, a detailed analysis of the relative position of the Sun concerning a spacecraft will be conducted using the Systems Tool Kit (STK) software. This analysis is crucial for determining the optimal placement of star trackers on a CubeSat. Understanding the dynamics of solar exposure is essential for ensuring that the star trackers, which rely on clear visibility of stars for accurate navigation, are positioned to avoid interference from sunlight. By modeling and simulating the spacecraft's orbit and its orientation with respect to the Sun, we aim to provide valuable insights for the effective design and operational planning of the CubeSat's attitude determination system.

Star trackers are critical components in a spacecraft's attitude determination system, providing precise orientation data by capturing images of star fields and comparing them to an onboard star catalog. To function effectively, star trackers must have an unobstructed view of the stars and avoid interference from bright light sources such as the Sun, Moon, and Earth. Proper placement of star trackers is essential to ensure accurate and reliable data. Typically, they are mounted on surfaces of the spacecraft that minimize the likelihood of direct sunlight or reflected light entering the optical path. Additionally, their positioning should consider the spacecraft's operational modes and potential obstructions from other structures or instruments. [20]

First, the CAD model of the CubeSat structure with the solar panel must be imported into the STK software. Next, the analysis is conducted using the local coordinate system, specifically the VVLH CBI (Vehicle Velocity Local Horizontal, Central Body Inertial) reference frame. In this coordinate system, the X-axis is aligned with the velocity vector, the Y-axis is perpendicular to both the X and Z axes, and the Z-axis points towards the geocentric nadir. The local coordinate system is illustrated in Fig. 4.1.

In the VVLH (CBI) reference frame, the angles analyzed are the azimuth and the elevation angles. The azimuth is the angle measured from the X-axis, with positive values oriented towards the Y-axis. The elevation is the angle measured

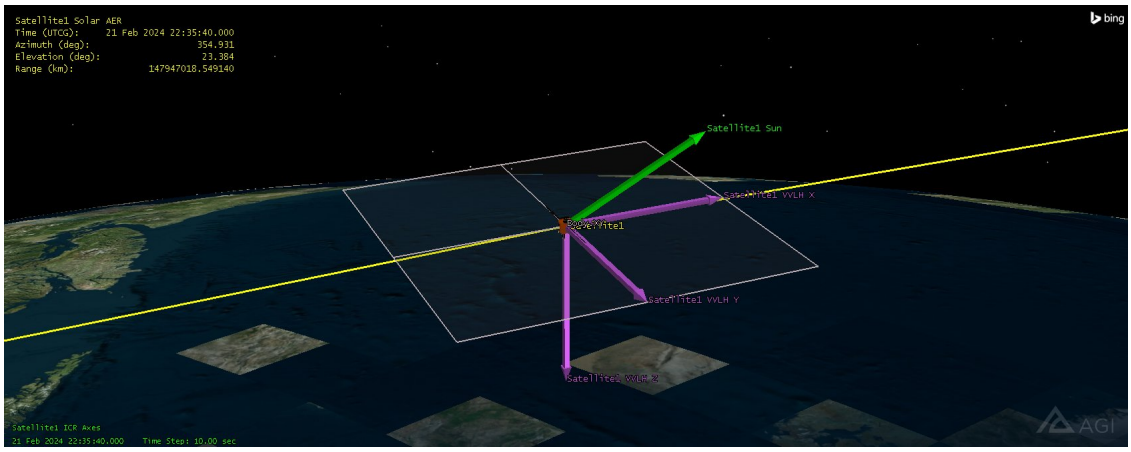

Figure 4.1: Representation on STK of the VVLH (CBI) reference frame.

from the X-Y plane, with positive values directed along the negative Z-axis. A resulting value of the analysis is also the evolution of the Range, which is the distance between the Sun and the CubeSat.

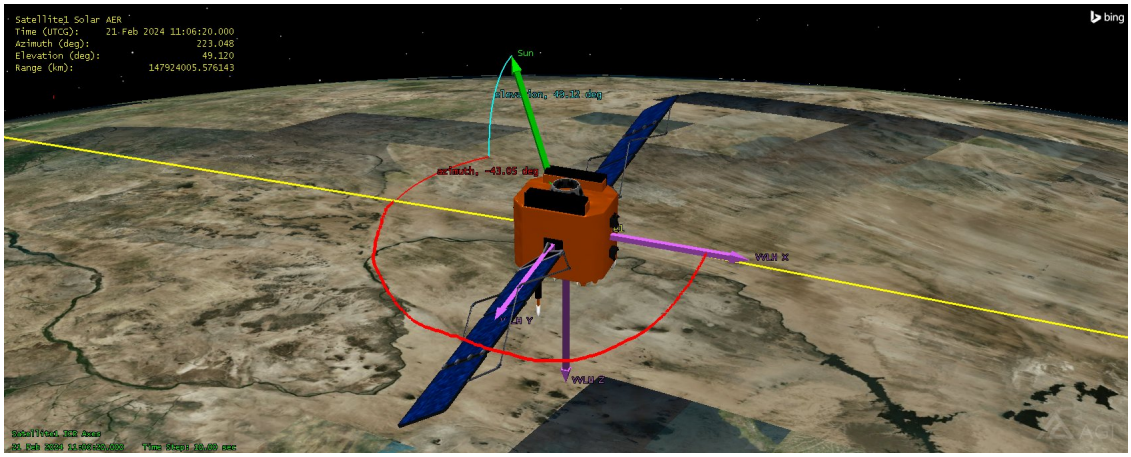

Figure 4.2: Representation on STK of the azimuth and elevation angles (in red the azimuth angle and in light-blue the elevation angle).

Figure 4.3 displays the graphs generated from the STK analysis, covering a duration of one and a half days. The azimuth angle is depicted in blue, the range in red, and the elevation angle in green.

Since the CubeSat will experience both periods of eclipse and sunlight, Figure 4.4 displays the resulting graph specifically for the sunlight condition. This graph illustrates the CubeSat's behavior and parameters during periods when it is exposed to sunlight.

From these results, it is clear that the Sun radiation is always on one side of the CubeSat, specifically on the side with negative Y.

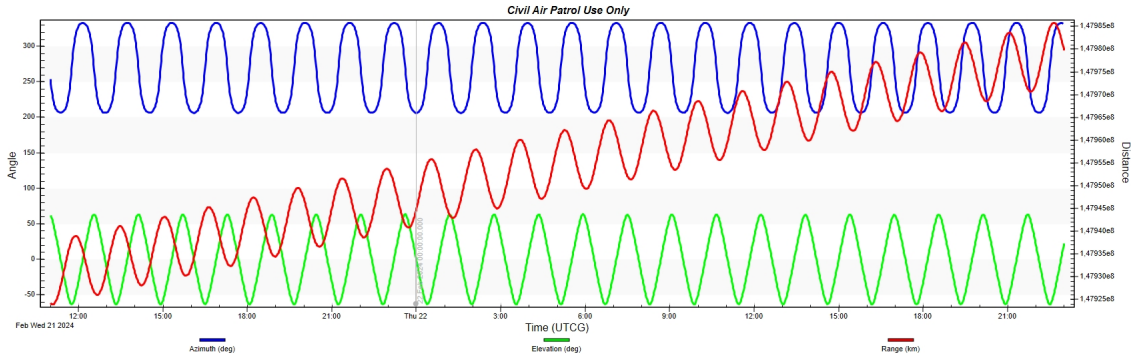

Figure 4.3: Evolution over time of the Elevation, Azimuth angle, and Range during the operational orbit.

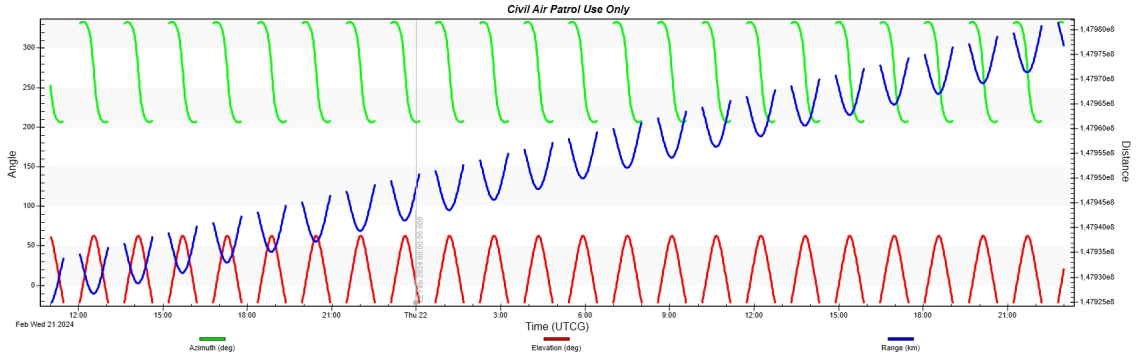

Figure 4.4: Evolution over time of the Elevation, Azimuth angle, and Range during the operational orbit in sunlight conditions.

Chapter 5

Thermal Analysis

A preliminary thermal analysis for the 16U4SBSP spacecraft has been performed and is presented in this chapter. The analysis has focused on one important aspect: a simplified single-node steady-state balance for the whole spacecraft, to predict the range of temperatures expected during operation and define a coating strategy on the external surface of the spacecraft for passive thermal control.

In order to develop a baseline understanding of the thermal loads and expected temperatures on the 16U4SBSP spacecraft, a single-node steady-state lumped mass analysis has been performed. The external dimensions of the 16U CubeSat structure (226 x 226 x 454 mm) are illustrated in Fig. 5.1. For the purpose of the analysis, this structure is represented using a simplified model as detailed in the subsequent chapter.

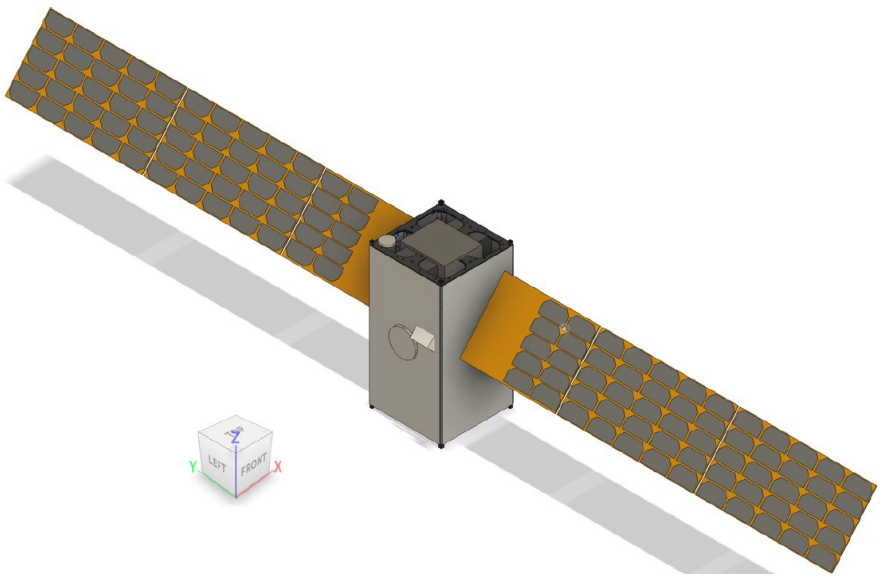

Figure 5.1: 16U4SBSP spacecraft with cover panels, solar array wings deployed. [24]

The thermal analysis is conducted considering the selected orbit in the Mission Design study, which is the Sun-Synchronous one with an altitude of 500 km and inclination $i = 97{,}4014°$. One of the main factors of this study is the so-called "beta angle", represented in Fig. 5.10, which is the angle between a satellite's orbital plane around Earth and the geocentric position of the Sun. The beta angle is crucial for understanding the percentage of time the satellite spends in direct sunlight, absorbing solar radiation. Two different options are considered: one corresponding to a beta angle of 0°, the other one corresponding to a beta angle of 70°, each leading to their own duration of the portion of a single orbit in eclipse. These two options have been chosen to identify two ideal conditions of worst thermal loads: the case with a beta angle of 0° represents the case of maximum time in eclipse; the case with a beta angle of 70° represents the case of maximum time in sunlight.

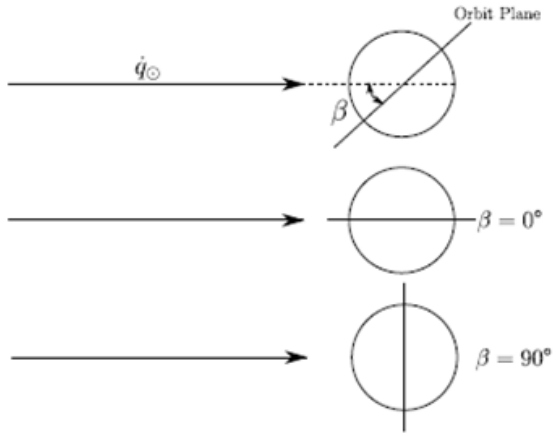

Figure 5.2: Geometric definition of Beta angle. [5]

Starting from the values of beta angle, it is possible to evaluate the percentage of eclipse duration as follows: [9]

$$f_e = \begin{cases} \frac{1}{180°} cos^{-1}\left(\frac{\sqrt{h^2+2Re\,h}}{(Re+h)cos\beta}\right), & |\beta| < \beta^* \\ 0, & |\beta| \geq \beta^* \end{cases} \tag{5.1}$$

where h is the value of orbit altitude, Re is the Radius of the Earth, and β^* is the critical beta angle, defined as: [9]

$$\beta^* = sin^{-1}\left(\frac{Re}{Re+h}\right) \tag{5.2}$$

By substituting the orbit altitude, the critical beta angle can be evaluated as 68°. So, the eclipse factors are:

$$f_e = \begin{cases} 0{,}3778 = 38\%, & \beta = 0° \\ 0\%, & \beta = 70° \end{cases} \tag{5.3}$$

Another critical factor for the thermal analysis is the season during which the satellite is considered to be operating. Indeed, in the Winter season the intensity of solar radiation is lower than in the Summer season. [15] For this reason, two cases are considered: Winter season with incident solar energy flux $S = 1317\ W/m^2$ and Summer season with $S = 1419\ W/m^2$. From now on, the two cases of ideal extreme conditions (described in Tab. 5.1) are called Case 1 and Case 2.

	h	**i**	β	**Season**	**Illumination**
Case 1.A	500 km	97,4014°	0°	Winter	Sunlight
Case 1.B	500 km	97,4014°	0°	Winter	Eclipse
Case 2	500 km	97,4014°	70°	Summer	Sunlight

Table 5.1: Conditions of Case 1.A, Case 1.B and Case 2.

These two cases were selected to represent the most extreme conditions. Case 1 combines the winter season, when the Earth is farthest from the Sun, with a β angle of 0°, resulting in the longest eclipse period. Case 2 combines the summer season, when the Earth is nearest to the Sun, with a β angle of 70°, resulting in the longest period of sunlight.

5.1 Heat Transfer Model

In this chapter, the Heat transfer model used for the analysis is described. Due to the high vacuum environment of space, an orbiting spacecraft can interact with their environment primarily through radiation. Internal heat dissipation can occur partially via conduction. Therefore, as shown in Fig. 5.3, for an Earth-orbiting spacecraft this interaction can be characterized by four means: [15]

- direct solar radiation;
- solar radiation reflected from the Earth (albedo radiation);
- planetary infrared radiation from the Earth;
- thermal radiation of energy from the external surfaces of the spacecraft to deep space.

As a result of this interaction, the spacecraft achieves thermal equilibrium when the heat gained from the first three sources, along with internal thermal dissipation, equals the energy radiated into deep space. By leveraging this phenomenon, it is possible to select surface properties to balance energy transfer across the desired spacecraft temperature range. This is achievable because the radiant energy absorbed from the environment is independent of the surface temperature, whereas

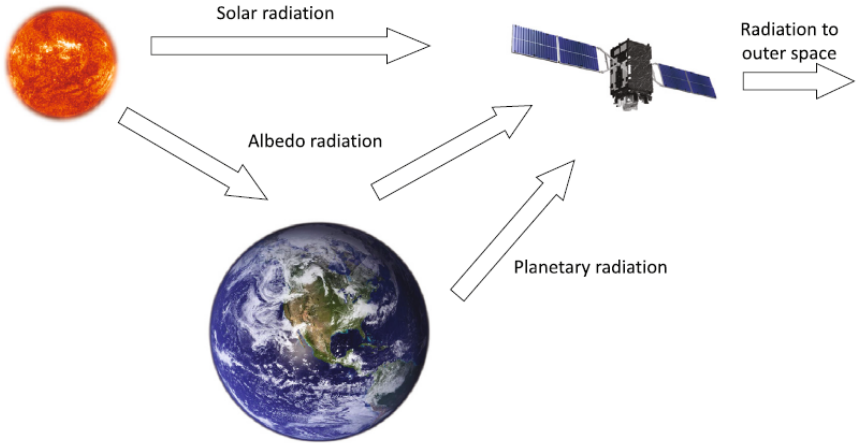

Figure 5.3: Spacecraft thermal environment. [28]

the energy radiated from the surface is highly dependent on its temperature. [15] The balance equation is:

$$Q_{in} = Q_{out} \tag{5.4}$$

$$Q_{solar} + Q_{albedo} + Q_{IR} + P_{internally\ dissipated} = Q_{out} \tag{5.5}$$

$$Q_{out} = A_r \cdot \varepsilon \cdot \sigma \cdot T^4 \tag{5.6}$$

where A_r is the radiating surface area of the CubeSat, ε is the emissivity of the surface, σ is the Stefan-Boltzmann constant ($\sigma = 5{,}67051 \cdot 10^{-8} W/m^2K^4$) and T is the absolute temperature in Kelvin. [15] It is now necessary to examine the sources of radiant energy in space one by one.

5.1.1 Direct Solar Energy

The direct solar energy flux varies with the distance from the Sun and is typically the primary heat source in spacecraft thermal management. The Sun emits energy uniformly in all directions, but from Earth's perspective, it appears as a small disc with an angular diameter of just 1/2 degree. This configuration causes the Sun's rays to strike a surface perpendicular to the Sun as parallel rays. [15]

There are two important characteristics of the Sun's radiant energy for spacecraft thermal control. These are the total energy density, or flux, incident on a surface, and the spectral content of that flux. The flux at 1 AU is called the Solar Constant and is calculated at the Earth's average distance from the Sun. The spectral composition of the solar flux mimics the black body radiation spectrum of an emitter at a temperature of $5\,780K$. [15]

As previously explained, to account for variability in solar heat load through the seasons, the model is run separately in two different cases: $S = 1419 W/m^2$ corresponding to the Summer season; $S = 1317 W/m^2$ corresponding to the Winter season. [28]

The direct solar energy flux can be calculated as follows:

$$Q_{solar} = S \cdot A_p \cdot [\%Solar\ time] \cdot \alpha_{AVG} \tag{5.7}$$

where A_p is the projected area toward the Sun, α_{AVG} is the average absorptivity of the external surface of the CubeSat. [15] The percentage of Solar time can be evaluated starting from the value of the beta angle, as previously explained in Eq. 5.1.

5.1.2 Albedo Energy (Reflected Solar Radiation)

Albedo radiation is the measure of the diffuse reflection of solar radiation received from Earth. In other words, it is the fraction of solar radiation that is reflected by the surface of a planet. It is measured on a scale ranging from 0, which corresponds to a theoretical black body, to 1, for a body that reflects all incident radiation. The measurement of albedo depends on several factors, including the weather and the spacecraft's orbit. [28]

The solar energy reflected by a planet becomes a significant source of radiant energy when a spacecraft is in close proximity to the planet. However, from higher altitudes, such as geosynchronous orbits, the albedo effect is negligible. Earth reflects between 25% and 55% of the incoming solar energy, depending on the properties of its surface. Different surfaces such as land, sea, clouds, and ice exhibit varying levels of reflectance. Therefore, on the sunlit side of the Earth, surfaces oriented towards the planet can receive incident energy amounting to 25% to 55% of the direct solar flux. The spectral composition of this reflected solar energy is nearly identical to that of direct sunlight. However, it reaches these surfaces as diffuse energy rather than parallel rays directly from the Sun. [15]

Calculating the albedo incident on different surfaces necessitates an understanding of the spacecraft's orientation and position in relation to the sunlit side of the Earth. Surfaces that are oriented away from the Earth will not receive any solar energy reflected from the planet.

The equation evaluating the energy heat flux is :

$$Q_{albedo} = Q_{incident\ albedo} \cdot A_{IR} \cdot \alpha_{AVG} \tag{5.8}$$

where A_{IR} is the area exposed to the infrared albedo energy, reflected by the planet. Table 5.4 summarizes the incident energy values for several orbit conditions of altitude and β angle considering the accepted range of variation for solar and Earth physical properties, to produce the "hot and cold" range of incident fluxes.

"Cold Case" W/m^2												
500 km	β = 0			β = 45			β = 70			β = 90		
Surface Orientation	Solar	Albedo	Earth IR	Solar	Albedo	Earth IR	Solar	Albedo	Earth IR	Solar	Albedo	Earth IR
Zenith	418.2			295.8			143.1			1.3		
Nadir	30.4	79.1	186.8	44.7	66.3	186.8	143.1	42.7	186.7	1.3	15.2	186.5
Sun	0.8	24.5	58.3	630.7	23.7	58.1	123.76	19.0	58.1	1317.0	16.5	58.0
Anti Sun	0.8	24.5	58.2		17.5	58.2		8.3	58.2			58.0
± Ram	287.3	24.6	58.0	226.0	20.6	57.9	143.1	13.3	57.9	1.3	5.3	57.9

"Hot Case" W/m^2												
500 km	β = 0			β = 45			β = 70			β = 90		
Surface Orientation	Solar	Albedo	Earth IR	Solar	Albedo	Earth IR	Solar	Albedo	Earth IR	Solar	Albedo	Earth IR
Zenith	450.6			318.7			154.2			1.4		
Nadir	32.7	123.9	224.6	48.2	98.9	224.7	154.2	59.6	224.6	1.4	19.7	224.4
Sun	0.9	38.4	70.1	679.5	35.4	69.9	1333.4	26.5	69.9	1419.0	21.4	69.8
Anti Sun	0.9	38.5	70.0		26.1	70.0		11.5	70.0			69.8
± Ram	309.5	38.6	69.7	243.5	30.8	69.7	154.2	18.6	69.7	1.4	6.8	69.7

	Cold case	Hot case	Units
Solar Constant	1 317,0	1 419,0	W/m^2
Albedo at β = 0°	0,22	0,32	
Albedo at β = 45°	0,26	0,36	
Albedo at β = 70°	0,34	0,44	
Albedo at β = 90°	0,49	0,59	
Earth IR	217,0	261,0	W/m^2

Figure 5.4: Orbit Average Incident Radiant Fluxes on Surfaces of an Earth-Oriented Cube for 500 km Circular Orbits. β is the angle of the Sun out of the orbit plane. The two cases analyzed are the Cold Case and the Hot Case.[15]

5.1.3 Planetary Radiation

Planetary infrared energy refers to the energy emitted by nearby planets. It depends on the planet's temperature and the spacecraft's orientation relative to the planet. The amount of heat incident on a surface is determined by the temperature of the source and the geometric relationship between the surface and the source. A surface that remains perpendicular to the source throughout its orbit will receive a constant infrared flux. A surface facing away from the source will receive none. [15] Although all planets in the solar system have non-zero temperatures and consequently radiate heat, Earth's planetary radiation will be considered the primary radiation from a planet affecting our analyzed spacecraft. [15] The equation evaluating the energy heat flux is :

$$Q_{IR} = Q_{incident\ IR} \cdot A_{IR} \cdot \varepsilon_{AVG} \tag{5.9}$$

where the emissivity is used instead of absorptance, and the reason for this is

explained at the beginning of the following section 5.1.4.

5.1.4 Absorbed Energy

The energy incident on a surface can either be absorbed or reflected. The surface characteristics that determine the absorbed energy are absorptance (α for solar energy) and emissivity (ε for infrared energy). Absorptance (α) defines the percentage of incident solar energy absorbed by the surface. Solar energy, which is primarily in the visible part of the electromagnetic spectrum, is absorbed differently compared to infrared energy. Emissivity (ε) represents the percentage of energy absorbed or emitted at infrared wavelengths. It is used to assess both the incident infrared energy absorbed by the surface and the infrared energy emitted from the surface at its temperature. [15] Tabs. 5.2 and 5.3 list some properties of typical surface finishes and coatings.

Material	**Absorptance,** α	**Emittance,** ε	**Absortion coefficient,** α/ε
Optical Solar Reflectors			
Silvered fused silica	0,07	0,8	0,0875
Indium - Tin - Oxide (ITO)	0,07	0,76	0,0921
Aluminized Teflon (0,5 mm)	0,14	0,4	0,35
Aluminized Teflon (10 mm)	0,15	0,85	0,1765
Silvered Teflon (2 mm)	0,08	0,68	0,1176
Silvered Teflon (10 mm)	0,09	0,88	0,1023
Black Coatings			
Catalac black paint	0,96	0,88	1,091
Delrin black plastic	0,96	0,87	1,1034
Martin black velvet paint	0,91	0,94	0,9681
Parsons black paint	0,98	0,91	1,0769
Vel-black	0,99	0,95	1,0421
White Coatings			
Barium sulphate with polyvinyl alcohol	0,06	0,91	0,0659
Catalac white plastic	0,24	0,9	0,267
NASA/GSFC NS-74 white paint	0,17	0,92	0,267
Magnesium oxide aluminum oxide paint	0,09	0,92	0,0978
White polyurethane paint	0,27	0,84	0,3214

Table 5.2: Spacecrafts' coating materials. [16]

Material	**Absorptance,** α	**Emittance,** ε	**Absortion coefficient,** α/ε
Anodized aluminium samples			
Anodized aluminium black	0,76	0,88	0,8636
Anodized aluminium blue	0,60	0,88	0,6816
Anodized aluminium chromic	0,44	0,56	0,7857
Anodized aluminium gold	0,48	0,82	0,5854
Anodized aluminium red	0,57	0,88	0,6477
Anodized aluminium yellow	0,47	0,87	0,5402
Film and tapes			
Aluminium tape	0,21	0,04	5,25
Aluminized aclar film (1 mm)	0,12	0,54	0,22
Aluminized kapton (aluminium outside)	0,14	0,05	2,8
Goldized kapton (gold outside)	0,25	0,02	12,5
Metals			
Buffled aluminium	0,16	0,03	5,33
Buffles copper	0,30	0,03	10
Polished aluminium	0,24	0,08	3
Polished Beryllium	0,44	0,01	44
Polished Gold	0,30	0,05	6
Polished Silver	0,04	0,02	2
Polished Stainless steel	0,42	0,11	3,818
Polished Tungsten	0,44	0,03	14,67
Vapor-deposited coatings			
Aluminium	0,08	0,02	4
Gold	0,19	0,02	9,5
Silver	0,04	0,02	2
Titanium	0,51	0,12	4,33
Tungsten	0,60	0,27	2,22
Polished Silver	0,04	0,02	2

Table 5.3: Spacecrafts' coating materials. [16]

5.2 Analysis

In this chapter, the thermal analysis of the 16U4SBSP CubeSat is presented. The CubeSat is treated as an approximately lumped mass, with the analysis conducted as a single-node evaluation. Separate thermal assessments are performed for the CubeSat's body and its solar panels, assuming that there is no contact between them. The CubeSat's body is modeled as a sphere with the same volume as the CubeSat's body. This assumption is often made when studying a spacecraft that is either inertially fixed or oriented toward a planet. [15] A sphere has isotropic properties, meaning thermal properties like absorption and emission of radiation are equal in all directions. This simplifies calculations and simulations. Results obtained from a spherical simplification are useful in this case, because is a preliminary analysis and initial estimate, but may not be sufficiently precise for detailed design and final thermal optimization. Indeed, the spherical shape does not accurately represent the flat surfaces, edges, and details of the real satellite's structure, which can lead to differences in calculations of thermal radiation absorption and emission. Real surfaces can have directional thermal properties that a sphere cannot represent. Future development of this analysis will require refining simulations and calculations using the satellite's actual geometry to achieve more accurate and reliable results.

5.2.1 Dissipated Power

Several assumptions have been made to estimate the power dissipated internally by the satellite, based on the figures provided in the power budget. Firstly, since the total power budget of the spacecraft is required to include an ESA system-level power margin, the nominal power requirements of the spacecraft were increased by 20%. [26] In addition, it is assumed that approximately 50% of the energy consumed by all subsystems (both in sunlight and in eclipse) is converted into heat and dissipated internally. The average dissipated power is then calculated by dividing this dissipated energy by the duration of the sunlight and eclipse portions of the orbit, respectively. Note that the energy dissipated by the payload is not included in this analysis, as it is managed by a dedicated heat dissipation system. For the solar arrays, it is assumed that the internally dissipated power is the difference between the incident solar flux and the power actually generated by the solar cells. The power budget of the 16U4SBSP mission is shown below in Fig. 5.10.

During the Sunlight time, the average energy consumed by the systems is 86,18 Wh. Including the ESA margin policy, the total margined energy is $86{,}18 \cdot (1 + 20\%) = 103{,}42\ Wh$. Therefore, as previously explained, the average dissipated energy as heat is: $103{,}42\ Wh \cdot 50\% = 51{,}71\ Wh$. To obtain the power dissipated, it is necessary to divide this amount of energy by the duration of the sunlight time.

For the Case 1.A :

$$P_{dissipated\ sunlight} = \frac{51{,}71\ Wh}{62\% \cdot T} = 52{,}89\ W \tag{5.10}$$

On the other hand, during the Eclipse time, the average energy consumed by the systems is 25,26 Wh (note that, as previously explained, this amount does not account for the energy used by the transmission system, as this system dissipates heat independently). The total margined energy is $25{,}26 \cdot (1 + 20\%) = 30{,}31\ Wh$. Thus, the average dissipated energy as heat is $30{,}31\ Wh \cdot 50\% = 15{,}15\ Wh$. For the Case 1.B :

$$P_{dissipated\ eclipse} = \frac{15{,}15\ Wh}{38\% \cdot T} = 25{,}28\ W \tag{5.11}$$

Regarding the Solar Panels, as mentioned before, the power dissipated internally as heat is the difference between the incident flux of solar radiant and the power generated by the solar cells. Both of these values depend on the inclination of the solar flux relative to the Solar Panel surface, that is beta angle. The case of $\beta = 0°$ is the situation of optimal conditions for the solar cells, because the solar flux is perpendicular to the surface. Therefore, the incident solar flux is maximum, as well as the generated power. Using the STK - Systems Tool Kit, it has been evaluated that the total amount of power generated by the 8 solar panels is 242,2 W. Therefore:

$$P_{incident\ flux} = S \cdot A_{solar\ cells} \cdot N_{solar\ cells} = 1317\frac{W}{m^2} \cdot (0{,}003018 \cdot 25)m^2 = 99{,}37\ W \tag{5.12}$$

$$P_{generated} = \frac{242{,}2\ W}{8} = 30{,}3\ W \tag{5.13}$$

$$P_{dissipated} = P_{incident\ flux} - P_{generated} = 69{,}07\ W \tag{5.14}$$

The case of $\beta = 70°$ has to be analyzed considering the inclination of the solar arrays. Using the software STK, it has been evaluated that the total amount of power generated by 8 Solar Panels is 84,8 W. Thus:

$$P_{incident\ flux} = S \cdot A_{solar\ cells} \cdot N_{solar\ cells} = 1419\frac{W}{m^2} \cdot (0{,}003018 \cdot 25)m^2 \cdot cos(70°) = 36{,}62\ W \tag{5.15}$$

$$P_{generated} = \frac{84{,}8\ W}{8} = 10{,}6\ W \tag{5.16}$$

$$P_{dissipated} = P_{incident\ flux} - P_{generated} = 26{,}02\ W \tag{5.17}$$

Component	# units	Sunlight			Eclipse			
		Power per unit [W]	Duty time [min]	Energy [Wh]	Power per unit [W]	Duty time [min]	Energy [Wh]	
Transmission system	1	331	0	0	331	10,00	55,17	*Assumed that power is delivered in night time only (eclipse), once per orbit. Total efficiency of the transmission system is 0.8x0.9x0.6=0.432 (331 W on board means 142.9 W delivered to ground per spacecraft; 142.9 W x 7 spacecraft = 1 kW).*
Thermal control (heaters)	5	5	0	0	5	17,85	7,44	*Assuming heaters are required for half of the eclipse period*
On-Board Computer	1	5,8	58,78	5,68	5,8	35,69	3,45	*Assuming OBC is continuously operational*
GNSS receiver	1	2	58,78	1,96	2	35,69	1,19	*Assumed as continuously operational*
S-band radio	1	2	19,20	0,64	2	10,00	0,33	*Assuming 10 minutes of inter-satellite communication in sunlight and 10 minutes in eclipse, plus communications to ground once per orbit*
ADCS box	2	10	26,67	8,89	10	10,00	3,33	*Assumed to be used in fine-pointing mode during power transmission or propulsion usage*
Propulsion, standby	1	16	58,78	15,67	16	35,69	9,52	*Assumed a total of 16 W continuously required standby power (main propulsion = 15 W per data sheet, RCS = 1 W assumed)*
Propulsion, RCS	1	40	0	0	40	0	0	*Assuming that in orbits when RCS is used (for desaturation or fast maneuvers), main propulsion is not used. Therefore, enough energy will be available from the power budget allocated to main propulsion.*
Propulsion, main (heat up)	1	40	10,00	7	40	0	0	*Assuming 10 minutes heating is sufficient (no info provided in the data sheet on this).*
Propulsion, main (operation)	1	105	26,67	46,67	105	0	0	*Assuming the worst case situation when maneuvers will be performed during an orbit (in Sunlight). For orbits where maneuvers are not performed, duty time will be zero. Max DeltaV per maneuver = 0.05 m/s -> 1.6 Ns -> 26.67 min burn.*
		TOT energy		**86,18**		**TOT energy**	**80,43**	
		ECSS margin		20 %		ECSS margin	20 %	
		TOT margined energy		**103,42**		**TOT margined energy**	**96,51**	
		Required charging energy to batteries		106,16		Charging losses	10 %	
		TOT required energy per orbit		209,58		**Required charging energy per orbit**	**106,16 Wh**	
						Available energy	258,4 Wh	
		Avg power per orbit		**213,94 W**		Required DoD	37 %	
		Distribution efficiency		10 %				
		Avg required power per orbit, from solar arrays		**235,33 W**				
		Available power		236 W				

Figure 5.5: Power budget for 16U4SBSP mission. [24]

5.2.2 Materials

The materials for the passive external coatings have been selected by a trade-off between four different combinations of materials, provided in Tab. 5.6. The materials were chosen from the Tabs. 5.2 and 5.3. The combinations of materials are selected to achieve a very low value of α_{AVG} and a low value of ε_{AVG}. This is because the absorbed energy needs to be minimal to prevent high temperatures during sunlight periods, while the emitted energy also needs to be low to avoid extremely low temperatures during eclipse periods. For each combination, the thermal analysis is conducted following the heat transfer model's equations explained in detail in chapter 5.1. The resulting temperatures are displayed in Tab. 5.7. The final step is a trade-off, for which the criteria used to select the optimal combination are based on ensuring temperature ranges within which the subsystems and solar panels can operate without complications. This involves maintaining temperatures ranging from approximately 0°C at the coldest to around the ambient temperature, which typically ranges between 5°C and 40°C.

Examining the temperatures shown in Tab. 5.7, it is evident that some combinations reach high temperatures, approaching $50°C$. This is unsuitable for the CubeSat design as it negatively impacts the operation of the sub-systems. Conversely, the temperatures in Cases 1.B are consistently acceptable. Consequently, combination number 4 has been selected, because it is the only one that has the temperature of Case 1.A near $40°C$.

Combination Number	Materials	α	ε	Percentage
1	Silver (vapor-deposited coating)	0,04	0,02	63 %
	Silvered Teflon (2 mm) (Optical solar reflector)	0,08	0,68	37 %
2	Aluminium (vapor-deposited coating)	0,08	0,02	68,5 %
	Indium - Tin - Oxide (ITO) (Optical solar reflector)	0,07	0,76	31,5 %
3	Silver (vapor-deposited coating)	0,04	0,02	70 %
	Indium - Tin - Oxide (ITO) (Optical solar reflector)	0,07	0,76	30 %
4	Silver (vapor-deposited coating)	0,04	0,02	65 %
	Aluminized Aclar film (1 mm)	0,12	0,54	5 %
	Silvered fused silica (Optical solar reflector)	0,07	0,8	30 %

Figure 5.6: Different combinations of materials used for a trade-off about thermal passive coating.

Indeed, for the CubeSat's body, combination 4 has been selected, utilizing the following materials in varying percentages:

- 65% of vapor-deposited coating made of Silver : $\alpha = 0{,}04$, $\varepsilon = 0{,}02$

1	CubeSat's Body Temperature
CASE 1. A	48,00° C
CASE 1. B	-5,72° C
CASE 2	25,06° C
2	**CubeSat's Body Temperature**
CASE 1. A	53,71° C
CASE 1. B	-3,30° C
CASE 2	32,95° C
3	**CubeSat's Body Temperature**
CASE 1. A	53,92° C
CASE 1. B	-0,72° C
CASE 2	29,47° C
4	CubeSat's Body Temperature
CASE 1. A	43,54° C
CASE 1. B	-8,95° C
CASE 2	20,90° C

Figure 5.7: Average temperature obtained from the thermal analysis conducted on different options of passive coating materials.

- 30% of Silvered fused silica (Optical solar reflector) : $\alpha = 0{,}07$, $\varepsilon = 0{,}8$
- 5% of Aluminized aclar film (1 mm) : $\alpha = 0{,}12$, $\varepsilon = 0{,}54$.

Therefore, the average values of absorptivity and emissivity for the body of the CubeSat are:

$$\alpha_{AVG} = (65\% \cdot 0{,}04) + (30\% \cdot 0{,}07) + (5\% \cdot 0{,}12) = 0{,}053 \tag{5.18}$$

$$\varepsilon_{AVG} = (65\% \cdot 0{,}02) + (30\% \cdot 0{,}8) + (5\% \cdot 0{,}54) = 0{,}280 \tag{5.19}$$

For the solar panels, the range of acceptable temperatures is different than the one for the CubeSat's body. Indeed, it is more wide and it generally goes from $-100°$ to $200°$. The solar cells cover 49,4% of the external surface of the solar panel; 50% is the surface facing the Earth; 0,6% is the surface facing the zenith without the solar cells. [24] The values of α and ε for the solar cells are specified in the datasheet of the chosen solar cells from AzurSpace Gmbh "30% Triple Junction GaAs Solar Cell Assembly". [10] The materials for the other surfaces of the solar panels are selected by looking at the general trend of the passive coating used in solar panels. The materials chosen for the Solar Panels are:

- Surface in nadir direction, without cells : black paint "Martin black velvet paint" $\alpha = 0{,}91$, $\varepsilon = 0{,}94$
- Surface in zenith direction:
  - Galium arsenide-based solar cells : $\alpha = 0{,}91$, $\varepsilon = 0{,}80$

– Aluminium vapor deposited coating: $\alpha = 0{,}08$, $\varepsilon = 0{,}02$.

Therefore, the average values of absorptivity and emissivity for the solar panels are:

$$\alpha_{AVG} = (50\% \cdot 0{,}91) + (49{,}4\% \cdot 0{,}91) + (0{,}6\% \cdot 0{,}08) = 0{,}905 \tag{5.20}$$

$$\varepsilon_{AVG} = (50\% \cdot 0{,}94) + (49{,}4\% \cdot 0{,}80) + (0{,}6\% \cdot 0{,}02) = 0{,}865 \tag{5.21}$$

5.2.3 Models and Areas

Modeling the body of the CubeSat as a sphere simplifies the calculations of the areas. Since the real measurements of the spacecraft are 22,6 cm × 22,6 cm × 45,4 cm, the sphere representative of the structure has the radius of $r = 17{,}69$ cm, since it is assumed to have the same volume as the spacecraft. Concerning the solar panels, each CubeSat has 2 wings, which are equipped with 4 solar panels each. Each solar panel is composed of 25 solar cells with an area of 30,18 cm^2 each. The model used to represent the solar panels in this thermal analysis is a parallelepiped of real dimensions 21 cm × 44 cm × 0,16 cm. Both the projected area toward the Sun and the area facing the Earth will be the same for any Case analyzed (Tab. 5.1). The solar panel always points to the Earth's center, so the area facing the Earth is the same. Instead, the area projected toward the Sun changes between the Cases due to the different β angle values.

Here are summarized the values of the areas needed for the equations' analysis:

- CubeSat's body - Case 1.A and Case 1.B: $A_p = 0{,}0983\ m^2$; $A_{IR} = 0{,}0983\ m^2$; $A_r = 0{,}3932\ m^2$
- CubeSat's body - Case 2: $A_p = 0{,}0983\ m^2$; $A_{IR} = 0{,}0983\ m^2$; $A_r = 0{,}3932\ m^2$
- CubeSat's solar panels - Case 1.A and Case 1.B: $A_p = 0{,}0924\ m^2$; $A_{IR} = 0{,}0924\ m^2$; $A_r = 0{,}1869\ m^2$
- CubeSat's solar panels - Case 2: $A_p = 0{,}0316\ m^2$; $A_{IR} = 0{,}0924\ m^2$; $A_r = 0{,}1869\ m^2$

Now, all the factors needed for the analysis have been explained.

5.2.4 CubeSat's body

In Tab. 5.8 are displayed the results of the thermal analysis equations, considering the material selected in chapter 5.2.2. Additionally, the solved equations for each case are provided below.

	Q_{SOLAR} [W]	Q_{ALBEDO} [W]	Q_{IR} [W]	$P_{DISSIPATED}$ [W]	Q_{OUT} [W]	T [°C]
Case 1.A	4,269	0,412	5,142	52,89	62,804	43,54
Case 1.B	0	0	5,1421	25,28	30,422	-8,95
Case 2	7,394	0,3105	6,183	32,79	46,680	20,90

Figure 5.8: Heat energy flux and temperature of the thermal analysis conducted of the CubeSat's 16U4SBSP mission.

CASE 1.A

$$Q_{solar} = S \cdot A_p \cdot [\%\ Solar\ Time] \cdot \alpha_{AVG} = 1317 \cdot 0{,}0983 \cdot 0{,}622 \cdot 0{,}053 = 4{,}2691\ W \tag{5.22}$$

$$Q_{albedo} = \dot{q}_{incident\ albedo} \cdot A_{IR} \cdot \alpha_{AVG} = 79{,}1 \cdot 0{,}0983 \cdot 0{,}053 = 0{,}4122\ W \tag{5.23}$$

$$Q_{IR} = \dot{q}_{incident\ IR} \cdot A_{IR} \cdot \varepsilon_{AVG} = 186{,}8 \cdot 0{,}0983 \cdot 0{,}280 = 5{,}1421\ W \tag{5.24}$$

$$P_{dissipated\ sunlight} = \frac{51{,}71\,Wh}{62\% \cdot T} = 52{,}89\ W \tag{5.25}$$

$$Q_{in} + P_{dissipated\ internally} = Q_{out} \tag{5.26}$$

$$Q_{out} = A_r \cdot \varepsilon \cdot \sigma \cdot T^4 = 0{,}3932 \cdot 0{,}280 \cdot 5{,}67051 \cdot 10^{-8} \cdot T^4 = (6{,}2438 \cdot 10^{-9}) \cdot T^4\ W \tag{5.27}$$

$$\boxed{T = 43{,}54°C} \tag{5.28}$$

CASE 1.B

$$Q_{solar} = 0\ W \tag{5.29}$$

$$Q_{albedo} = 0\ W \tag{5.30}$$

$$Q_{IR} = \dot{q}_{incident\ IR} \cdot A_{IR} \cdot \varepsilon_{AVG} = 186{,}8 \cdot 0{,}0983 \cdot 0{,}280 = 5{,}1421\ W \tag{5.31}$$

$$P_{dissipated\ eclipse} = \frac{15{,}15\,Wh}{38\% \cdot T} = 25{,}28\ W \tag{5.32}$$

$$Q_{in} + P_{dissipated\ internally} = Q_{out} \tag{5.33}$$

$$Q_{out} = A_r \cdot \varepsilon \cdot \sigma \cdot T^4 = 0{,}3932 \cdot 0{,}280 \cdot 5{,}67051 \cdot 10^{-8} \cdot T^4 = (6{,}2438 \cdot 10^{-9}) \cdot T^4\ W \tag{5.34}$$

$$\boxed{T = -8{,}95°C} \tag{5.35}$$

CASE 2

$$Q_{solar} = S \cdot A_p \cdot [\%\ Solar\ Time] \cdot \alpha_{AVG} = 1419 \cdot 0{,}0983 \cdot 1 \cdot 0{,}053 = 7{,}394\ W \tag{5.36}$$

$$Q_{albedo} = \dot{q}_{incident\ albedo} \cdot A_{IR} \cdot \alpha_{AVG} = 59{,}6 \cdot 0{,}0983 \cdot 0{,}053 = 0{,}3105\ W \tag{5.37}$$

$$Q_{IR} = \dot{q}_{incident\ IR} \cdot A_{IR} \cdot \varepsilon_{AVG} = 224{,}6 \cdot 0{,}0983 \cdot 0{,}280 = 6{,}183\ W \tag{5.38}$$

$$P_{dissipated\ eclipse} = \frac{51{,}71\,Wh}{100\% \cdot T} = 32{,}79\ W \tag{5.39}$$

$$Q_{in} + P_{dissipated\ internally} = Q_{out} \tag{5.40}$$

$$Q_{out} = A_r \cdot \varepsilon \cdot \sigma \cdot T^4 = 0{,}3932 \cdot 0{,}280 \cdot 5{,}67051 \cdot 10^{-8} \cdot T^4 = (6{,}2438 \cdot 10^{-9}) \cdot T^4\ W \tag{5.41}$$

$$\boxed{T = 20{,}90°C} \tag{5.42}$$

5.2.5 CubeSat's Solar Panels

In Tab. 5.9 are displayed the results of the thermal analysis equations, considering the material selected in chapter 5.2.2. Additionally, the solved equations for each case are provided below.

	Q_{SOLAR} [W]	Q_{ALBEDO} [W]	Q_{IR} [W]	$P_{DISSIPATED}$ [W]	Q_{OUT} [W]	T [°C]
Case 1.A	68,520	6,615	14,936	69,070	159,13	89,8
Case 1.B	0	0	14,936	0	14,936	-72,26
Case 2	40,58	4,984	17,96	26,02	89,539	41,2

Figure 5.9: Heat energy flux and temperature of the thermal analysis conducted for the Solar Panel of the CubeSat's 16U4SBSP mission.

CASE 1.A

$$Q_{solar} = S{\cdot}A_p{\cdot}[\%\ Solar\ Time]{\cdot}\alpha_{AVG} = 1317{\cdot}0{,}0924{\cdot}0{,}622{\cdot}0{,}905 = 68{,}52\ W \quad (5.43)$$

$$Q_{albedo} = \dot{q}_{incident\ albedo} \cdot A_{IR} \cdot \alpha_{AVG} = 79{,}1 \cdot 0{,}0924 \cdot 0{,}905 = 6{,}615\ W \quad (5.44)$$

$$Q_{IR} = \dot{q}_{incident\ IR} \cdot A_{IR} \cdot \varepsilon_{AVG} = 186{,}8 \cdot 0{,}0924 \cdot 0{,}8653 = 14{,}936\ W \quad (5.45)$$

$$P_{dissipated\ sunlight} = 99{,}37 - 30{,}3 = 69{,}07\ W \quad (5.46)$$

$$Q_{in} + P_{dissipated\ internally} = Q_{out} \quad (5.47)$$

$$Q_{out} = A_r{\cdot}\varepsilon{\cdot}\sigma{\cdot}T^4 = 0{,}1869{\cdot}0{,}8653{\cdot}5{,}67051{\cdot}10^{-8}{\cdot}T^4 = (9{,}1698{\cdot}10^{-9}){\cdot}T^4\ W \quad (5.48)$$

$$\boxed{T = 89{,}8°C} \quad (5.49)$$

CASE 1.B

$$Q_{solar} = 0\ W \quad (5.50)$$

$$Q_{albedo} = 0\ W \quad (5.51)$$

$$Q_{IR} = \dot{q}_{incident\ IR} \cdot A_{IR} \cdot \varepsilon_{AVG} = 186{,}8 \cdot 0{,}0924 \cdot 0{,}8653 = 14{,}936\ W \quad (5.52)$$

$$P_{dissipated\ sunlight} = 0\ W \quad (5.53)$$

$$Q_{in} + P_{dissipated\ internally} = Q_{out} \tag{5.54}$$

$$Q_{out} = A_r \cdot \varepsilon \cdot \sigma \cdot T^4 = 0{,}1869 \cdot 0{,}8653 \cdot 5{,}67051 \cdot 10^{-8} \cdot T^4 = (9{,}1698 \cdot 10^{-9}) \cdot T^4\ W \tag{5.55}$$

$$\boxed{T = -72{,}26°C} \tag{5.56}$$

CASE 2

$$Q_{solar} = S \cdot A_p \cdot [\%\ Solar\ Time] \cdot \alpha_{AVG} = 1419 \cdot 0{,}0316 \cdot 1 \cdot 0{,}905 = 40{,}58\ W \tag{5.57}$$

$$Q_{albedo} = \dot{q}_{incident\ albedo} \cdot A_{IR} \cdot \alpha_{AVG} = 59{,}6 \cdot 0{,}0924 \cdot 0{,}905 = 4{,}984\ W \tag{5.58}$$

$$Q_{IR} = \dot{q}_{incident\ IR} \cdot A_{IR} \cdot \varepsilon_{AVG} = 224{,}6 \cdot 0{,}0924 \cdot 0{,}8653 = 17{,}96\ W \tag{5.59}$$

$$P_{dissipated\ sunlight} = 36{,}62 - 10{,}6 = 26{,}02\ W \tag{5.60}$$

$$Q_{in} + P_{dissipated\ internally} = Q_{out} \tag{5.61}$$

$$Q_{out} = A_r \cdot \varepsilon \cdot \sigma \cdot T^4 = 0{,}1869 \cdot 0{,}8653 \cdot 5{,}67051 \cdot 10^{-8} \cdot T^4 = (9{,}1698 \cdot 10^{-9}) \cdot T^4\ W \tag{5.62}$$

$$\boxed{T = 41{,}2°C} \tag{5.63}$$

Element	Beta angle = 0°		Beta angle = 70°
	Sunlight	Eclipse	
Spacecraft body	43.5 °C	-8.9 °C	20.9 °C
Solar array wings	89.8 °C	-72.3 °C	41.2 °C

Figure 5.10: Average temperature for the CubeSat's 16U4SBSP mission, using passive external coating (Body: Vapor-deposited coating made of Silver, Silvered fused silica, Aluminized aclar film – Solar Panel: black paint "Martin black velvet paint", Galium arsenide-based solar cells, Aluminium vapor deposited coating)

5.2.6 Discussion of the Results

The results are obtained assuming a spherical shape for the spacecraft. This assumption leads to a discrepancy between the temperatures obtained from the analysis and the actual temperatures. A preliminary simplified analysis performed considering the actual parallelepiped shape for the spacecraft showed that the results are expected to diverge by no more than ± 5 ° compared to the results obtained for a spherical spacecraft shape; it has therefore been decided to use the results from the spherical spacecraft assumption as a sufficiently accurate first-order assumption for the cold and hot temperatures expected in the spacecraft.

From the temperatures obtained in the previous chapter, it is evident that they are suitable for the spacecraft of the 16U4SBSP mission. This conclusion can be drawn by comparing these temperatures with the accepted temperature ranges for the sub-systems and components, as reported in Table 5.4. The table shows the operational and non-operational temperature ranges, using the usual color code to indicate their compliance with the predicted spacecraft temperatures in orbit.

While the predicted thermal conditions are generally acceptable for most subsystems and components, there are potential criticalities for some components, namely the batteries, propulsion system/RCS, and star trackers, especially under cold/eclipse conditions. Consequently, the current spacecraft design includes a total of 5 active heaters, each with a heating power of 5 W. These heaters are strategically placed near the most critical sub-systems and components to provide active thermal control in emergency or non-ideal conditions.

Sub-system/Component	Operating Min	Operating Max	Non-Operating Min	Non-Operating Max
Solar Cells	-150	250	N/A	N/A
Batteries	-5	45	-20	20
Power Control Unit	-40	85	N/A	N/A
SADA	-20	50	N/A	N/A
Main Propulsion	0	50	-10	60
RCS Propulsion	0	50	-10	60
Reaction Wheels	-20	70	-40	80
IMU	-40	85	N/A	N/A
Sun Sensors	-30	85	N/A	N/A
Star Trackers	-20	40	-20	60
S-band radio	-20	60	N/A	N/A
GNSS receiver	-20	60	N/A	N/A
On-Board Computer	-30	60	N/A	N/A
16U structure	-40	80	N/A	N/A
Payload	-20	60	N/A	N/A

Table 5.4: Accepted temperature ranges for 16U4SBSP sub-systems and components, and compliance to the predicted spacecraft temperatures in orbit (green = compliant; yellow = correctable deficiencies; red = not compliant).

Chapter 6

Conclusion

This chapter presents the conclusions drawn from the research conducted on a preliminary mission analysis and sub-system design for the 16U4SBSP CubeSat mission. The primary aims of this study were to investigate the stability of the formation of CubeSats in a Heliotropic orbit and to conduct a thermal analysis to have a basic understanding of the range of operational temperatures. Throughout the investigation, several key findings have emerged, which are summarized and discussed in this chapter. Additionally, the limitations of the study are acknowledged, and recommendations for future research are proposed.

6.1 Summary of Key Findings

The research findings regarding the stability of CubeSats' formation flying indicate that the Heliotropic orbit is not a suitable choice for the Mission Analysis of the 16U4SBSP mission. Specifically, it was observed that the formation begins to diverge from the very first days of the mission in the absence of propulsion control. This divergence underscores the inherent instability of the initial orbit selected. In contrast, the Sun-Synchronous orbit emerges as a more suitable alternative for achieving the mission's objectives. In this orbit type, the formation maintains stability for the first 20 days without requiring any propulsion adjustments. These findings offer valuable insights into the trade-offs associated with selecting the operational orbit. The instability of the initially chosen orbit necessitates frequent propulsion adjustments, which consequently significantly increase maintenance costs. In contrast, the stability of the Sun-Synchronous orbit during the critical initial period suggests that it could be a more cost-effective option, reducing the need for constant propulsion interventions and thereby lowering overall mission expenses.

The study conducted reveals that there isn't a straightforward correlation between the instability of the formation and the orbital geometry. This suggests that

factors other than the orbit's geometry may play significant roles in influencing formation stability.

The thermal analysis indicates that the selected materials for passive thermal control are suitable for the 16U4SBSP mission. Indeed, the temperatures reached by the CubeSat under the two extreme conditions studied fall within the operational temperature ranges permitted for all spacecraft subsystems and components. While the predicted thermal conditions are generally acceptable for most subsystems and components, some critical issues may arise for specific components, particularly the batteries, propulsion system/RCS, and star trackers, especially during cold or eclipse conditions. Therefore, the current spacecraft architecture includes a total of 5 active heaters, each with a 5 W heating capacity, strategically positioned near the most critical subsystems and components for emergency or non-ideal thermal control.

6.2 Recommendations for Future Research

Based on the findings and limitations identified in this study, several recommendations for future research can be proposed. These suggestions aim to address the gaps and challenges encountered, as well as to explore new avenues that could further enhance the understanding of the formation stability and the thermal analysis.

For the preliminary Mission Analysis study, future research should investigate more deeply the reasons behind the instability of the formation in the Heliotropic orbit. Additionally, one potential enhancement in the dynamic model is to replace the cannonball model with the actual shape of the satellite and to consider the solar cycle, as it primarily affects atmospheric density. Exploring the impact of propulsion systems on the stability and cost-efficiency of formations in the Heliotropic Orbit is another area that warrants further investigation.

For the thermal analysis study, future research should aim to enhance the accuracy of the analysis by employing a multi-node approach or utilizing advanced thermal simulation software. These methods can provide more precise temperature readings and a deeper understanding of thermal behavior. Furthermore, it is advisable to include a broader range of extreme scenarios, particularly by considering different conditions of the β angle. This comprehensive approach will ensure that the thermal analysis is robust and accounts for a variety of potential situations.

Ringraziamenti

Ringrazio il mio relatore Angelo Cervone per avermi offerto la possibilità di scrivere questa tesi a TUDelft. Ringrazio Wail Boumchita per avermi seguita e sostenuta nella stesura di questa tesi. Ringrazio la mia relatrice Manuela Battipede.

Bibliography

[1] *U.S. Standard Atmosphere, 1976.* National Oceanic and Atmospheric Administration, National Aeronautics and Space Administration, United States Air Force, 1976.

[2] R. H. Battin, editor. *An Introduction to the mathematics and Methods of Astrodynamics.* AIAA Education Series, 1987.

[3] D.L. Boulet, editor. *Methods of Orbit Determination for the Microcomputer.* Willmann-Bell Richmond, 1991.

[4] J. D. Biggs C. Maclean, D. Pagnozzi. *Planning Natural Repointing Manoeuvres for Nano-Spacecraft.* IEEE Transactions on Aerospace and Electronic Systems, 2014.

[5] D. L. Cotten C. Versteeg. *Preliminary Thermal Analysis of Small Satellites.* Small Satellite Research Laboratory, The University of Georgia, 2018.

[6] H. D. Curtis, editor. *Orbital Mechanics for Engineering Students.* Butterworth-Heinemann, 2020.

[7] C. Bruccoleri D. Mortari, M. P. Wilkins. *On Sun-Synchronous Orbits and Associated Constellations.* Texas AM University, 2004.

[8] S.Broschart D.Lantukh, R.P. Russel. *Heliotropic Orbits at Oblate Asteroids: Balancing Solar Radiation Pressure and J2 Perturbations.* 2014.

[9] D. G. Gilmore. *Spacecraft Thermal Control Handbook.* The Aerospace Press, El Segundo, 2002.

[10] AZURSPACE Solar Power Gmbh. *30 % Triple Junction GaAs Solar Cell Assembly - Type: TJ Solar Cell Assembly 3G30A.* 2016.

[11] S. Xiucong H. Chao, G. Xiaojie. *Rapid Satellite-to-Site Visibility Determination Based on Self- Adaptive Interpolation Technique.* School of Astronautics, Beihang University, 2017.

[12] J. L. Junkins H. Schaub, editor. *Analytical Mechanics of Space Systems.* AIAA Education Series, 2003.

[13] G. Hill, editor. *Researches in the Lunar Theory.* American Journal of Mathematics, 1878.

[14] N. Al-Dhahir J. E. Hershey I. Ali, P. G. Bonanni. *Doppler Applications in LEO Satellite Communication Systems.* Springer New York, NY, 2002.

[15] J. J. Puschell J. R. Wertz, D. F. Everett. *Space Mission Engineering: The*

New SMAD. Space Technology Library, 2015.

[16] L. Kauder. *Spacecraft thermal control coatings references*. NTRS - NASA Technical Reports Server, 2005.

[17] W. M. Kaula. *Theory of Satellite Geodesy - Applications of Satellites to Geodesy*. Blaisdell Publishing Company, 1966.

[18] C. A. Kluever. *Space Flight Dynamics*. Wiley, 2018.

[19] A. Puig L. Zardaìn, A. Farrès. *High-Fidelity modeling and visualizing of solar radiation pressure: a framework for high-fidelity analysis.* 2020.

[20] Dr. Carl Christian Liebe. *Star Trackers for Attitude Determination*. 1994.

[21] P. Gurfil M. Lara. *J2-perturbation solution to the relative motion problem*. 2012.

[22] R. G. Melton. *Time Explicit Representation of Relative Motion Between Elliptiocal Orbits*. Journal of Guidance, Control, and Dynamics, 2000.

[23] J. J. Michalsky. *The Astronomical Almanac's algorithm for approximate solar position (1950-2050)*. Pergamon Journals, 1988.

[24] M.Vasile M.Madi, A.Cervone. *Final Report - Swarms of CubeSats for kW-scale Space-Based Solar Power (16U4SBSP)*. 2024.

[25] National Almanac Office, editor. *The Astronomical Almanac for the Year 2019*. GPO, 2018.

[26] SRE-PA D-TEC staff. *Margin philosophy for science assessment studies*. European Space Research and Technology Centre, 2012.

[27] Y. Ulybyshev, editor. *Geometric analysis of low-earth-orbit satellite communication systems: coverage functions.* Journal of Spacecraft and Rockets, 2000.

[28] F. J. Fuenmayor V. Alcayde, A. Vercher-Martınez. *Thermal control of a spacecraft: Backward-implicit scheme programming and coating materials analysis*. Elsevier B.V., 2021.

[29] D. Vallado. Fundamentals of astrodynamics and applications. Springer, 2001.

[30] M. Vasile. *Fractioned solar power satellite for regional coverage*. 63rd International Astronautical Congress Naples, Italy, 2012.

[31] R. S. Wiltshire W. H. Clohessy, editor. *Terminal Guidance System for Satellite Rendezvous*. Journal of the Aerospace Sciences Vol.27, 1960.